POLITECNICO DI TORINO

DENERG – Energy Department

Master of Science in Energy and Nuclear Engineering

Master Thesis

Innovative technique to assess the performance of photovoltaic generators: experimental analysis for energy estimation of commercial high efficiency PV modules.

Supervisors:

Prof. Filippo Spertino

Prof. Gustavo Nofuentes Garrido

Prof. Slawomir Gulkowski

Ing. Gabriele Malgaroli

Candidate:

Martina Dattesi

22nd October 2020

Academic Year 2019/2020

I would like to thank Professor Filippo Spertino, Professor Vicente Munoz and Ing. Gabriele Malgaroli who have been of great help and support in the developing of this thesis. I would like to thank our group at University of Jaén, with whom the Monday meetings on skype have made this experience more enjoiable despite all the adversities that 2020 and the global pandemic have brought to us.

Ringrazio i miei 'amici di Torino', che sono tutto fuorchè torinesi, senza i quali l'esperienza universitaria sarebbe stata sicuramente più triste e noiosa. Un ringraziamento speciale va ad i miei coinquilini, Alessandro e Giacomo, nei quali ho trovato una seconda famiglia in questi anni lontana da casa e che mi hanno sopportato, e supportato, nei momenti di sconforto. Ringrazio il mio ragazzo, Lorenzo, che mi è stato sempre vicino in tutti i miei momenti di ansia, dandomi la forza di andare avanti e di trovare sempre il sorriso nei momenti più stressanti.

Torino non sarebbe stata la stessa senza di voi.

Vorrei poi ringraziare i miei amici di sempre, con cui sono cresciuta insiame sin dal liceo nonostante la distanza che ci divide. In particolare vorrei ringraziare Alessia, il cui modo di fare mi ha sempre spinta a mettermi in dubbio per conoscermi meglio, Gaia, che è sempre stata disponibile per parlare e per offrirmi uno spunto diverso ogni qualvolta ne avessi bisogno, e Giulia, che ogni volta che tornavo a casa era sempre pronta a darmi il benvenuto come se non fossi mai andata via. Grazie per tutto quello che avete fatto per me in questi anni.

Infine, desidero soprattutto ringraziare dal profondo del cuore la mia famiglia, in particolare i miei genitori e mia sorella, che mi hanno spinta a dare sempre il massimo, appoggiandomi con affetto in tutte le mie scelte senza farmi mai mancare nulla.

Ringrazio anche la mia cara nonna, che nonostante la sua assenza ho sentito più che mai vicina in questi ultimi due anni.

Abstract

The pressing issues related to climate change have made photovoltaic technology one of the leading renewable technologies. Besides the many advantages however, the PV technology is still characterized by lower efficiency and high investment cost compared to the standard technologies based on fossil fuels. For this reason, it is paramount to guarantee the optimal operation of the solar module in any given condition, in order to exploit, as best as possible, the solar source. This can be achieved only by developing suitable models that can accurately simulate the behaviour of a PV cell. This thesis focuses on the experimental analysis and comparison of three models to assess the performance of a PV module. The first two models are based on the equivalent circuit with the single diode model with five parameters, for which appropriate correlations have been found using two numerical methods, Levenberg-Marquardt (LM) and a combination of Simulated-Annealing and Nelder-Mead (SA-NM) respectively. The third method uses the most common theoretical model known in literature, the Osterwald model. The procedure is applied to three sets of experimental data associated with different solar photovoltaic technologies: a high efficiency Heterojunction with Intrinsic Thin layer (HIT) as well as two thin film (CIGS and CdTe) technologies. The results show that the LM model guarantees the higher level of accuracy as it exhibits the lowest deviation with respect to the measurements. The SA-NM is able to achieve similar results, and the lower level of accuracy is compensated by lower computational cost. Lastly, the Osterwald model has proven to be the less accurate of the three for all three applications.

Table of Contents

List of Figures

List of Tables

Introduction

Due to the shortage of fossil fuels and the generation of pollutant agents that comes with their usage, the search for renewable energy sources has become an important topic of research. In fact, unlike fossil fuels, renewable energy offers clean and inexhaustible solutions to the ever-increasing demand of energy. In particular, the sun provides the most powerful and abundant natural energy source, which can be exploited in solar photovoltaic technology to directly produce electrical energy in a sustainable way. The performance of solar photovoltaic modules is strongly affected by weather conditions such as irradiance and air temperature. In literature, many models analyse PV modules using an equivalent circuit with a variable number of parameters. However, these parameters vary with irradiance and temperature and their dependence on weather conditions is not uniquely determined in literature. Thus, this work aims to correctly identify equations describing the dependence on irradiance and cell temperature for the parameters of the PV modules under analysis. Moreover, the identification of these equations may be fundamental for diagnosis purposes. In fact, the knowledge of the parameters of the equivalent circuit, in any weather condition, may be used to trace the current-voltage (*I-V*) curve of PV generators and to search for deviations from the reference parameters, corresponding to healthy modules.

The work presented in this thesis is part of a joint activity performed at Politecnico di Torino and at the University of Jaén. In particular, this thesis focuses on the experimental validation of an innovative technique developed at Politecnico di Torino to predict the parameters of the equivalent circuit in any condition of irradiance and temperature.

The procedure consists of the following steps. First, the experimental data are properly filtered to remove measured curves affected by mismatch or shadowing. Then, the parameters of a selected equivalent circuit model are extracted. In this case, the single diode model has been selected to describe the behaviour of a PV module, because it guarantees a good compromise bewteen high accuracy and simplicity. Moreover, two numerical methods have been used to extract the parameters of this model: the Levenberg-Marquardt and a combination of

Simulated-Annealing and Nelder-Mead algorithms. The extracted parameters with the two methods are then used to identify appropriate equations that can describe each parameter as a function of irradiance and temperature. In particular, the coefficients of available equations in literature are obtained by applying a non-linear regression.

Finally, the equations are validated by comparing the predicted PV energy generated during the experimental campaign with experimental data. Moreover, the most common method in literature to estimate the maximum power is used to compare the different methods. This method uses the Osterwald model, which is the most used and accurate theoretical model known in literature. It provides the maximum power as a function of the atmospheric conditions and the temperature coefficient γ.

In this work, the above-described analysis has been performed on three PV modules from different technologies: a high efficiency Heterojunction with Intrinsic Thin layer (HIT) module and two thin films, a Copper Indium Gallium Selenide(CIGS) and a Cadmium Telluride (CdTe) modules. The corresponding experimental campaigns were carried out in 2011 (HIT) and 2012 (CIGS, CdTe).

Chapter 1

Structure and operating principle of solar cells

All energy on Earth has been created by the ‘solar power’ as it is the fundamental energy that sustains every process on earth: from the photosynthesis of plant to the process of production of fossil fuels, as well as wind and hydroelectric energy. Therefore, it can be said that solar energy is the most abundant source of energy available, exceeding by several orders of magnitude the total human consumption of energy, as it is shown in figure (1.1). In other words, if it could be converted completely in usable energy, the sunlight that reaches the Earth in a day could be enough to address the needs of the world for a whole year.

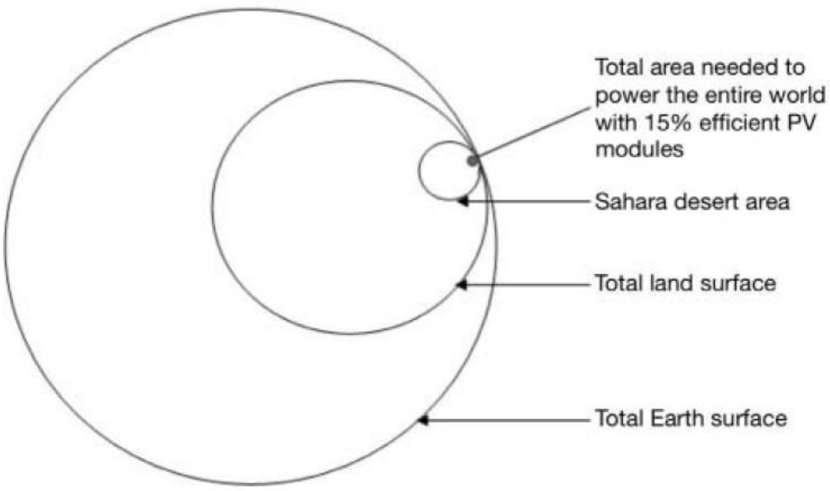

Figure 1-1: Theoretical needs to provide energy to the world (Not to scale) [1]

Due to the shortages of fossil fuels and the generation of pollutant agents that comes with their usage, the search for renewable energy sources has become an important topic of research. [2] [1] [3] [4] In this sense, the great availability of energy source from the Sun has made renewable sources exploiting the Sun’s energy extremely interesting as its applications are multiple since it can be used both directly and indirectly.

One way to exploit directly the energy coming from the sun is through the photovoltaic effect, which is the operating principle of the PV technology. Fundamentally, a solar cell is a p-n junction made of semiconductor material that can absorb light causing the photovoltaic effect. This generates electron-hole pair inside the solar cell, which gives rise to an electric field and a controlled motion of charges, generating electricity. In this chapter, the fundamental aspects of the PV technology will be presented as well as a brief overview on the primary source, solar energy.

1.1 Solar Energy

Sunlight is a form electromagnetic radiation that essentially consists of a range of energy bands also called solar spectrum. In this sense, the solar spectrum can be divided in different wavelengths that are characterized by different energies. The most important components of the spectrum consist in the ultraviolet radiation (UV), the visible radiation and the infrared radiation (IR). Most of the UV radiation is filtered out by the atmosphere and never reaches the surface as the energy that reaches the Earth's surface is mostly made of visible radiation (400 to 700 nm).

The electromagnetic spectrum describes light as a wave with a particular wavelength. However, for some specific applications such as photovoltaic technologies, the light behaviour can be described according to the Plank definition: as if was made of 'particles' of energy with no mass, that travel at the speed of light. These particles are called *photons*. Each photon is characterized by either a wavelength or an energy, which are inversely proportional with each other. In fact, the *photon energy* is given by the following equation:

$$E_{ph} = \frac{h \cdot c}{\lambda} \tag{1-1}$$

Where:

- $h = 6.626 \cdot 10^{-34} \left(\frac{m^2 Kg}{s}\right)$, is the Plank constant.
- $c = 3 \cdot 10^{-8} \left(\frac{m}{s}\right)$, is the speed of ligth.
- $\lambda\ (\mu m)$, is the wavelength

Moreover, since when dealing with particles, the common unit of energy used is the electron-volt (eV), the formulation can be written as follows:

$$E_{ph} = \frac{1.24[eV]}{\lambda} \tag{1-2}$$

This formulation is very important to understand the interaction of sunlight with p-n junctions inside solar cells. A second parameter can also be estimated to determine the number of electrons which are generated, and therefore the current produced, in a solar cell. This parameter is called the *photon flux*, and it is defined as follows:

$$\phi_{ph} = \frac{n.of\ photons}{sec \cdot m^2} \tag{1-3}$$

The combination of the photon flux and the photon energy can be used to estimate the power density for photons at a wavelength.

Moreover, it is possible to identify other important parameters to describe the behaviour and the characteristics of the solar radiation that are paramount to study the behaviour of PV modules:

Firstly, it is important to mention the *solar irradiance*, or *incident solar radiation*, which is the power per unit area received from the sun in the form of electromagnetic radiation. Depending on the type of measure, there are several types of irradiances:

1. *Total Solar Irradiance*: is the value of the solar energy integrated over the whole spectrum that reaches the top of the atmosphere.
2. *Direct Normal Irradiance*: is the amount of solar radiation per unit area received by a surface that is always normal to the sun-rays coming from the sun. It is equal to extraterrestrial irradiance above the atmosphere minus the absorption and scattering losses.
3. *Diffuse Horizontal Irradiance*: is the amount of solar radiation per unit area received by a surface that has been scattered by the molecules present in the atmosphere. It is the light that comes from clouds and all the points in the sky excluding the direct radiation coming from the sun.

4. *Global Horizontal Irradiance*: is the amount of solar radiation per unit area received by a horizontal surface. It is given by the sum of the two previously mentioned contributions.

Moreover, considering this parameter, it is possible to identify a standardized condition known as 'clear sky condition'. This condition is usually identified by the absence of clouds in the sky and it is characterized by daily irradiance curves such as the following.

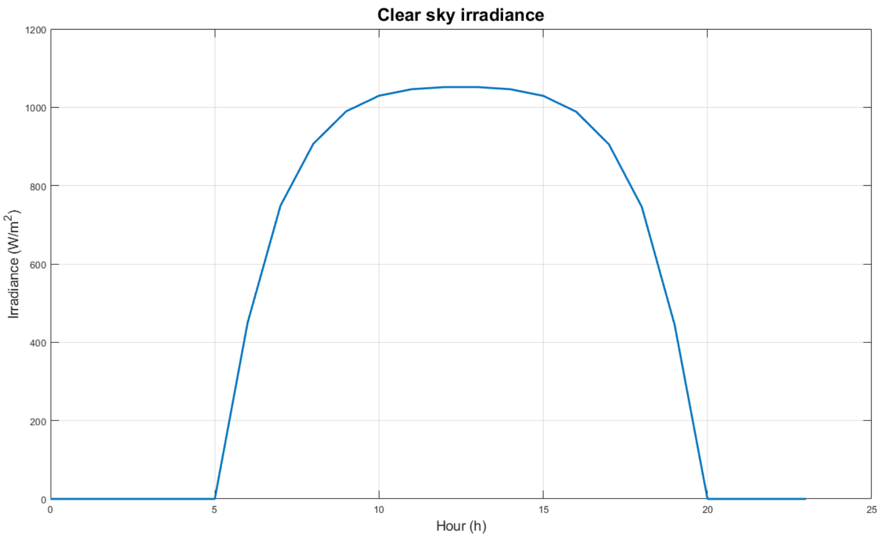

Figure 1-2: Daily curve of clear sky irradiance

A second important parameter is the *air mass*. The air mass represents the portion of the atmosphere that the sun rays must travel through to reach the Earth's surface, normalized with respect to the overhead path which is the shortest possible path. It is a measure of the power reduction that light undergoes due to the interaction with the various molecules composing the atmosphere. The Air Mass is equal to 1 when the real path corresponds to the overhead path and it increases with the real path-length that the sun-light has to travel. Considering θ as the zenith angle between the real path and the overhead path, the air mass is given by the formula:

$$AM = \frac{1}{\cos(\theta)} \tag{1-4}$$

1.2 Electronic Band Structure

In order to properly understand the electronic behaviour of a solar cell, it is important to understand how materials are categorized. In this sense, band theory is the basis of many technologies based on solid state electronics, such as solar cells.

Contrary to the behaviour of an electron in free space, the behaviour of an electron in a solid lattice, and therefore its energy, is strictly related to the behaviour of the other particles that are around it. This establishes a distinction between the ranges of energy that the electron can assume, called allowed bands, and the ranges that the electron cannot possess, called forbidden bands.

When moving to a macroscopic scale, the allowed bands in a solid are strictly related to the discrete allowed energies of the single atoms, called energy levels. Considering a homogeneous solid, the energy of each atom becomes perturbed through quantum mechanical effects by the energy levels of all the other atoms, since the various orbitals overlap each other. Since the number of atoms in a solid is very large (10^{-22}), the number of orbitals is very large and thus they are very closely spaced in energy (10^{-22}eV). For this reason, they can be considered as a continuum, forming many electronic bands with different values of energy.

All the electrons from the many atoms occupy a band in the solid called valence band, more stable and at lower values of energy, while all the empty states of the various atoms are broadened into an electronic band that is normally empty, called conduction band, which is usually at higher levels of energy. Often, between the two band there is a gap of forbidden energies, called energy gap. The electrons in the solid lattice can transfer from one energy level in a given band into another in the same band or into another band, depending on the particular structure of the material and therefore of the band structure and the energetic input provided.

The Fermi level is a hypothetical level that electrons have a 50% probability to occupy at thermodynamic equilibrium (absolute temperature of 0 K). This value is crucial to determine the electrical properties of different materials, since its position with respect to the band energy levels will change accordingly.

According to this structure, three distinct groups of materials can be found:

1. *Conductors (Metals)*: forbidden bands do not occur in the range of the most energetic electrons, which means that the valence band and the conduction

band are partially or totally overlapped. For this reason, metals are good electrical conductors, since electrons can easily transit from valence to conduction band, where they are free to move. The Fermi level lies in a delocalized band, which is close to states that are thermally active and ready to carry current.

2. *Insulators*: have wide forbidden bands that can be crossed only if the electron has a very high energy, which is very unlikely to happen. For this reason, insulators are poor conductors. In this case, the Fermi level lies in the energy gap.
3. *Semiconductors*: have a more narrow forbidden band, which can be crossed by valence electron with sufficient energy, higher than that of the forbidden bands.

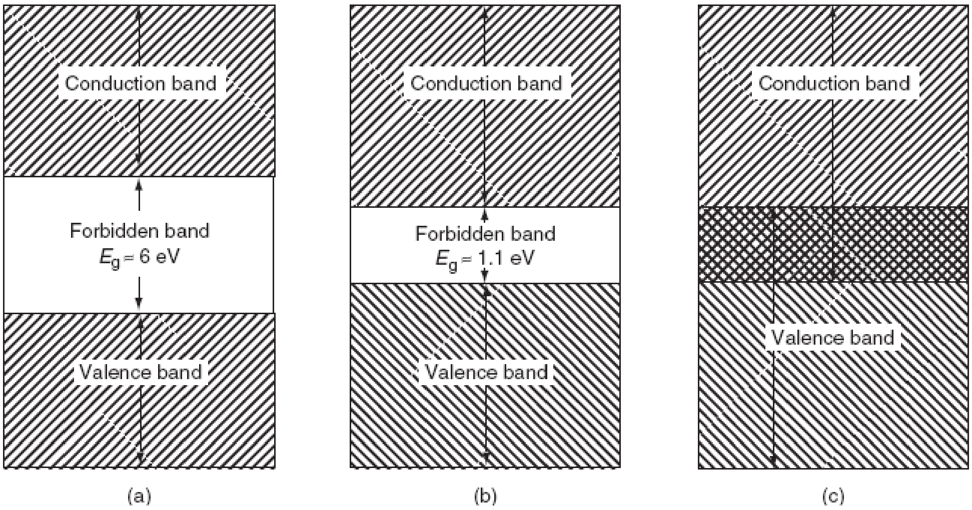

Figure 1-3: Band structure model of different materials: (a) insulators - (b) semiconductors - (c) conductors

In particular, semiconductors materials are of great interest for photovoltaic applications since it's were the energy conversion occurs. In fact, semiconductors materials are employed in many electronic devices, such as diodes and transistors. They have a wide range of current and voltage handling capabilities, and often are able to pass current more easily in one direction than the other.

The conductivities of semiconductors are generally between those of conductors and insulators. They are very sensitive to:

- Temperature, since the resistance falls as the temperature increases.
- Illumination.
- Magnetic fields.

- Doping, which is related to the percentage of impurity atoms found in the solid lattice. In general, in their natural state, semiconductors are poor conductors because they have their valence bands filled, preventing the flow of new electrons. For this reason, they are usually doped in order to improve their conductivity by causing an imbalance in the number of electrons.

The main semiconductor materials are:

- Those composed of single species of atoms, such as *silicon*, which is the most used semiconductor*, germanium* and *tin*;
- Those in the VI column of the periodic table;
- Compound semiconductors, made of two or more elements, such as *gallium arsenide* (GaAs), the second most used semicondutor, *mercury indium telluride* ($HgIn_2Te_4$) or *aluminum gallium arsenide* ($Al_xGa_{1-x}As$).

The properties of semiconductors materials are related to their atomic characteristics, and therefore change from group to group.

1.3 Silicon

Silicon is a nonmetallic chemical element, one of the most abundant elements on the planet, second only to oxygen. Due to the high reactivity of pure Silicon, the primary element is usually found in nature in rocks, sand, clays, and soils in the form of quartz, which is made of non-crystallized silicon oxide (SiO_2 or silica).

To obtain crystalline silicon, quartz is heated up in a graphite crucible where metallurgical grade silicon is obtained, with a purity of 98%. A further step of extreme purification is necessary to obtain solar grade silicon with the required purity of 99.99999%. This is done through a reaction with hydrochloric acid (HCl) that creates trichlorosilane $SiHCl_3$ and hydrogen. The two products are then separated through a fractional distillation process, since H_2 is in gaseous form at temperatures lower that 30 °C whilst $SiHCl_3$ is liquid. Lastly, pure silicon is separated from trichlorosilane with a chemical vapor deposition process.

Due to its atomic structure, Silicon is one of the most commonly used semiconductors, with a band gap of 1.12 eV. Silicon is a member of group IV, with atomic number 14. It is tetravalent, with 4 valence electrons, that are those involved in the chemical bonds with the neighboring atoms. Each atom is made of a nucleus which contains protons and neutrons surrounded by electrons, such that the number of electrons and protons is equal, in order to guarantee electrical neutrality.

Figure 1-4: Atomic structure of silicon

In the solid structure, the silicon atoms are bonded together with a covalent bond in a regular shape, which means that between each atom and its 4 surrounding atoms, 8 electrons are being shared.

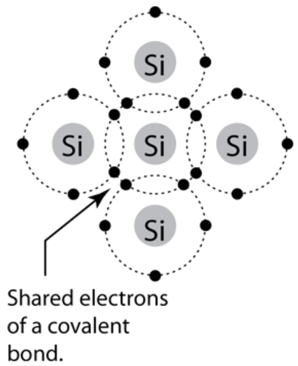

Figure 1-5: Chemical bonds in the silicon structure

At absolute temperature (0K) the electrons are completely employed in the formation of the covalent bond, so the silicon behaves as an insulator since there are no electrons free to move. As the temperature increase, the atoms are able to break the bonds causing the electrons with sufficient energy to jump from the valence band to the conduction band. This energy is equal to the energy gap, which is the energy necessary to break the covalent bond and generate the electron-hole pair.

Introducing small quantities of impurities inside the silicon lattice can enhance the semiconducting properties since they can shift the balance of electrons and holes in the lattice.

- *N-type*: this kind of semiconductors are obtained by introducing atoms with an additional valence electron, such as those of V group, like *phosphorus*. When small quantities of these atoms are added in the silicon lattice an electric current is able to flow inside the lattice. This is caused by the fact that the fifth electron introduced with the dopant has nothing to bond with and it is free to move, thus can jump relatively easily in the conduction band. For this reason the donor energy level is close to the conduction band, reducing the overall band gap and therefore the energy required for the other electrons to jump from the valence to the conduction band.
  Due to the higher number of free electrons present inside the lattice they are called the majority charge carriers, while free mobile holes are called minority charge carriers.

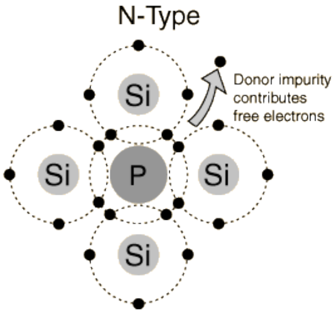

Figure 1-6: N-doped silicon with phosphorus

- *P*-type: this kind of semiconductors are obtained by introducing atoms with less electrons, thus introducing an additional vacancy (hole), called acceptor. They are therefore member of the group III, such as *boron*. The absence of electrons creates a positive charge that makes the electrons in the valence band become mobile. Due to their nature, the holes are able to conduct current by accepting the electrons of the neighbouring atoms. This causes the holes to move in the opposite direction of the movement of the electrons, generating a current. Since the hole introduced by the dopand may be already occupied at low-energy by an electron from the valence band, the acceptor energy level is close to the valence band, reducing once again the overall band gap.
  In this kinds of semiconductors, the holes are the majority charge carriers whilst free electrons are the minority charge carriers.

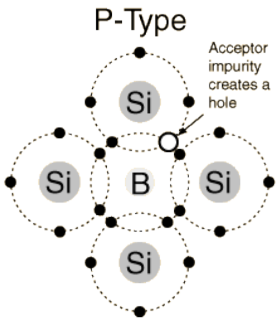

Figure 1-7: P-doped silicon with boron

After the doping process the semiconductors are still electrically neutral so the terms n-type and p-type simply refers to the majority charge carriers present in the crystalline lattice.

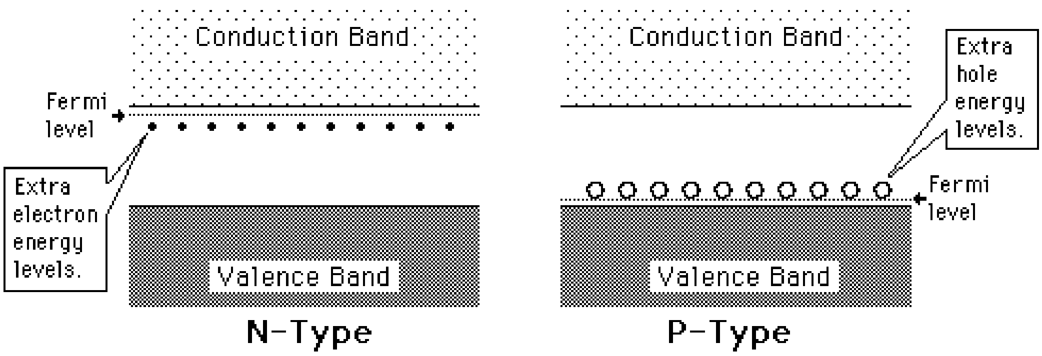

Figure 1-8: Band model of doped semiconductors

1.4 P-N Junction

The P-N junction is the basic requirement for photovoltaic energy conversion as it creates an electronic asymmetry in the semiconductor structure. It is the interface created between two regions with opposite doping inside the semiconductor material. Due to the different doping this area is characterized by the absence of free charge carriers (depletion zone), because the concentration gradient triggers the phenomenon of diffusion. Considering that there is only a small number of free electrons in the P-type layer and only a small number of holes in the N-type layer, the free electrons of the N-type layer recombine with the holes of the P-type near the interface region, causing a motion of the majority carriers from one type to the other.

- Electrons in N-type layer, that are negatively charged, are attracted by the positive charges in the P-type layer. Due to this motion the P-type layer is charged negatively since it has gained electrons whilst the N-type layer is charged positivley since it has lost them.
- Holes in P-type layer, that are positively charged, are attracted by the negative charges in the N-type layer. Due to this motion the P-type is charged negatively since it has lost holes whilst the P-type layer is charged positively since it has gained them.

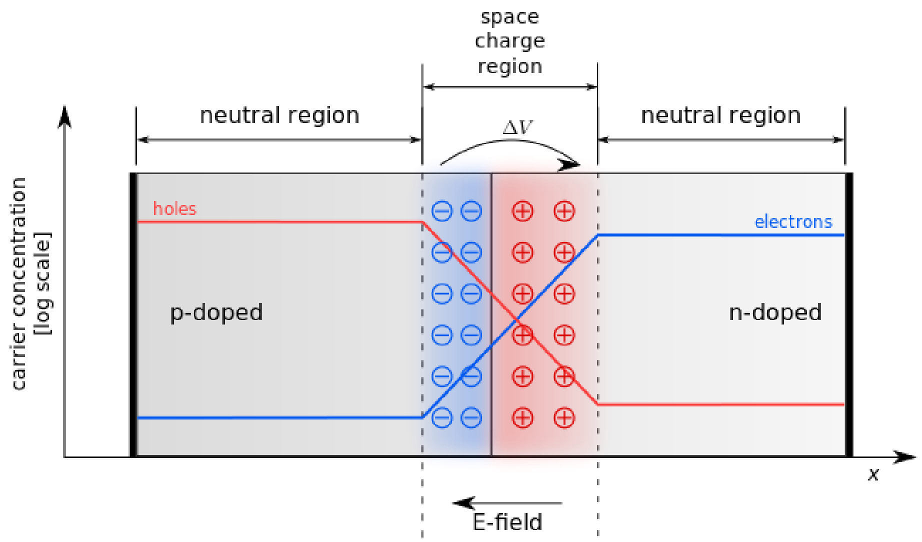

Figure 1-9: P-N junction

In this sense, the creation of the P-N junction generates two opposite motions of charges.

1. The *diffusion current* is the current generated as a result of the concentration gradient of the charge carriers inside the semiconductor of a P-N junction, which consists in the net transfer of charge carriers from the area with the higher density to that with the lowest density. It is the dominant current near the depletion region.
   The most probable direction coincides with the passage of the carriers from the zone with the higher concentration to that with the lower concentration. Since there is both a positive and a negative charge movement, we can say that the diffusion phenomenon generates a simultaneous motion of the two charges in two different directions. This motion is the diffusion current, and can be written as follows:

$$j_{diffusion} = j_p + j_n = q \cdot D_n \cdot \frac{dn}{dx} - q \cdot D_p \cdot \frac{dp}{dx} \tag{1-5}$$

Where:

- D_p, is the diffusion coefficient of the positive charges (holes) inside the semiconductor.
- D_n, is the diffusion coefficient of the negative charges (electrons) inside the semiconductor.
- q, is the elementary charge.
- dp/dx, is the concentration gradient of the positive charges (holes).
- dn/dx, is the concentration gradient of the negative charges (electrons).

2. The *drift current* is the current generated due to the presence of the electric field in the depletion region. The minority charges, subjected to the action of the electric field, tend to move in order to guarantee the electroneutrality. This current increases as the voltage difference between the two regions increases, counterbalancing the diffusion effect until steady state is achieved. This motion consists in the net transfer of the charge carriers (both positive and negative) to the area oppositely charged. In particular, electrons move in the direction opposite to the electric field whilst the holes move in the direction of the electric field. Moreover, an expression for the surface density of the drift current can be written as follows:

$$j_{drift} = q \cdot n \cdot \mu_n \cdot E + q \cdot p \cdot \mu_p \cdot E \tag{1-6}$$

Where:

- q, is the elementary charge.
- n, is the concentration of the negative dopant atoms.
- p, is the concentration of the positive dopant atoms.
- μ_n, is the mobility of the negative charges (electrons)
- μ_p, is the mobility of the positive charges (holes).
- E, is the intensity of the electric field

As shown in equation (1-6), the charge movement is characterized by the mobility. The mobility is a parameters which varies between different semiconductors materials and it indicates how easily the charge carries is able to move inside the lattice.

At the beginning, the diffusion current is predominant over the drift current. As the charges recombine, the depletion zone increases, thus increasing the voltage difference between the two layers. In the absence of an external electric field, after a certain threshold (0.7 V for Silicon) the recombination stops, and the diffusion phenomenon reaches an equilibrium since the charges are no longer able to overcome the electric field that is generated by this motion. A steady state is finally reached, which results in the creation of a junction that contains no mobile charges.

$$j = j_{diff} - j_{drift} = q\left(D_n \frac{dn}{dx} - n\,\mu_n\,E - D_p \frac{dp}{dx} - p\,\mu_p\,E\right) = 0 \qquad (1\text{-}7)$$

The function of the P-N junction is to allow an electric current only in one direction and block the current in the opposite direction. For this reason, we can say that the photovoltaic cell behaves like a diode. The typical symbol and nomenclature used for diodes is presented in figure (1-10).

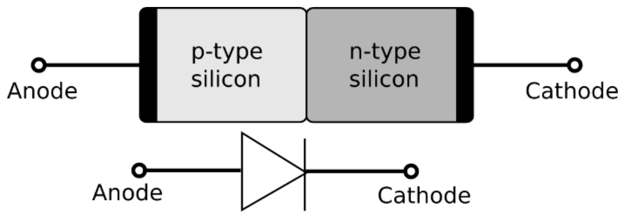

Figure 1-10: Diode symbol

As already stated, when no external source is applied, the diode reaches the equilibrium condition and the two currents described before perfectly balance each other out. On the contrary, when subjecting the P-N junction to an external voltage source under dark conditions, there are two configurations possible:

1. *Forward Bias*: this is achieved by applying the positive voltage to the p-type layer (anode) and the negative voltage to the n-type layer (cathode). The effect of this kind of connection is to activate the diffusion phenomenon while simultaneoulsy reducing the electric field, which results in the distruption of the equilibrium existing at the junction and the reduction of the depletion region. In fact, as they are repelled from the positive and negative terminals of the voltage source, electrons and holes are pushed

toward the junction. After a certain treshold value that depends on the semiconductor material, the application of a great enough voltage can cause both the holes and the electrons to overcome the depletion region were they can recombine closing the circuit and allowing the current flow.
Typical values of the minimum threshold voltage for Si-diodes are around 0.7 V. In this type of configuration, the diode is considered active or ‘ON’ as it enable the current to pass through.

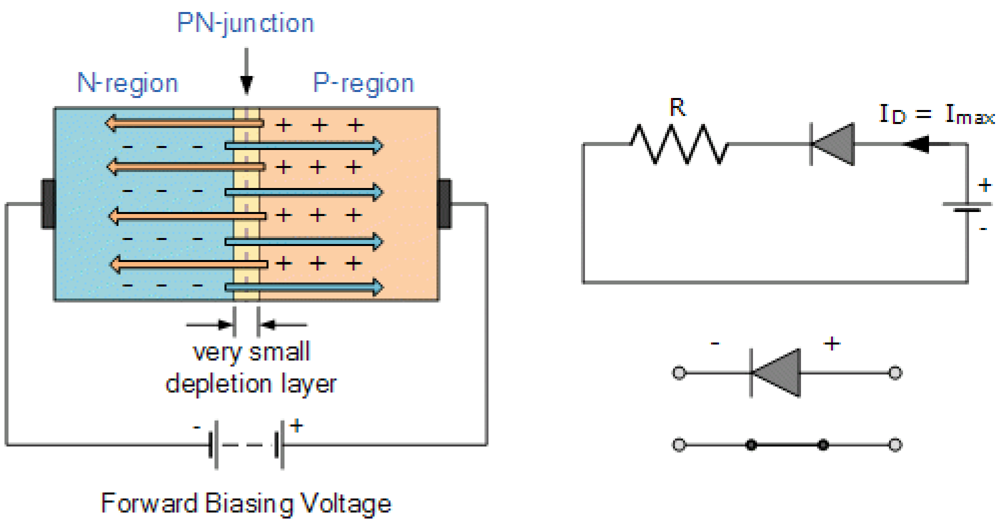

Figure 1-11: Diode in forward bias

2. *Reverse Bias*: this is achieved by applying the positive voltage to the n-type layer (cathode) and the negative voltage to the p-type layer (anode).
This connection increases the electric field at the junction and therefore the depletion region. As a consequence, the propability that the charges can diffuse from one side of the junction to the other is very low, hence the diffusion current is reduced and the steady state condition is ‘forced’.
A small increase in the drift current can be observed due to the increase of the depletion region, but essentially the drif current remains constant since it is limited by the number of minority carriers present on either sides of the p-n junction. Moreover, since the state state condition is ‘forced’ , a reverse current of equal magnitude occurs in order to guarantee internal equilibrium. This current is called the saturation current and it is a measure of the ‘leakage’ of carriers across the p-n junction.
For this reason, in this configuration the diode is considered inactive or ‘OFF’, as no current is allowed to pass.

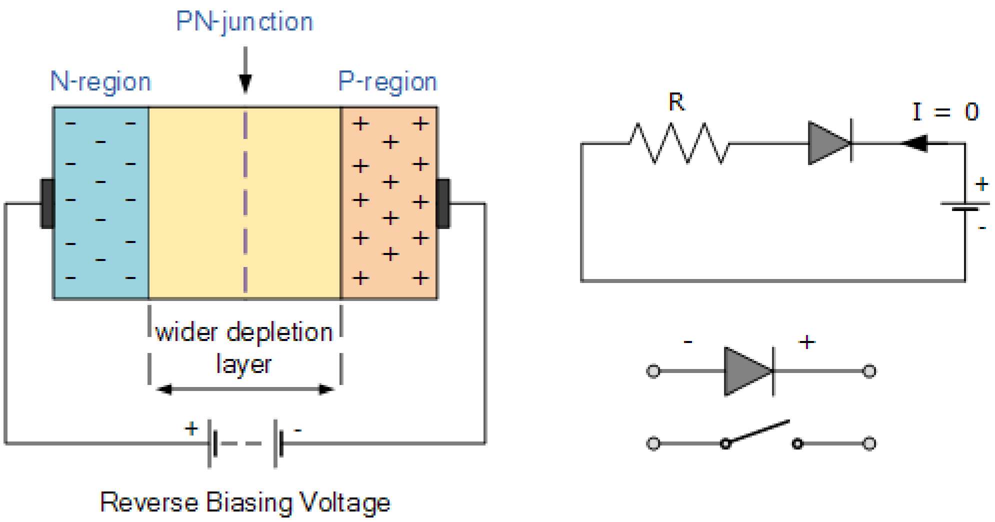

Figure 1-12: Diode in reverse bias.

Considering this, it is possible to draw the p-n junction characteristic shown in figure (1-13). The physical behaviour of a p-n junction with no illumination is described by the Shockley Equation:

$$I = I_{diffusion} - I_{drift} = I_0 e^{\left(\frac{q\,V}{n\,k\,T}-1\right)} = I_0 e^{\left(\frac{V}{n\,V_{th}}-1\right)} \tag{1-8}$$

Where:

- I_0 (A), is the saturation current under reverse bias.
- $q = 1.6\ 10^{-19} (C)$, is the elementary charge.
- $n\ (-)$, is the diode ideality factor.
- $k = 1.38\ 10^{-23} \left(\frac{J}{K}\right)$, is the Boltzmann's constant.
- $V\ (V)$, is the applied voltage.
- $T\ (K)$, is the diode temperature
- $V_{th}\ (V)$, is the thermal voltage which is given by the formula:

$$V_{th} = \frac{k\,T}{q} \tag{1-9}$$

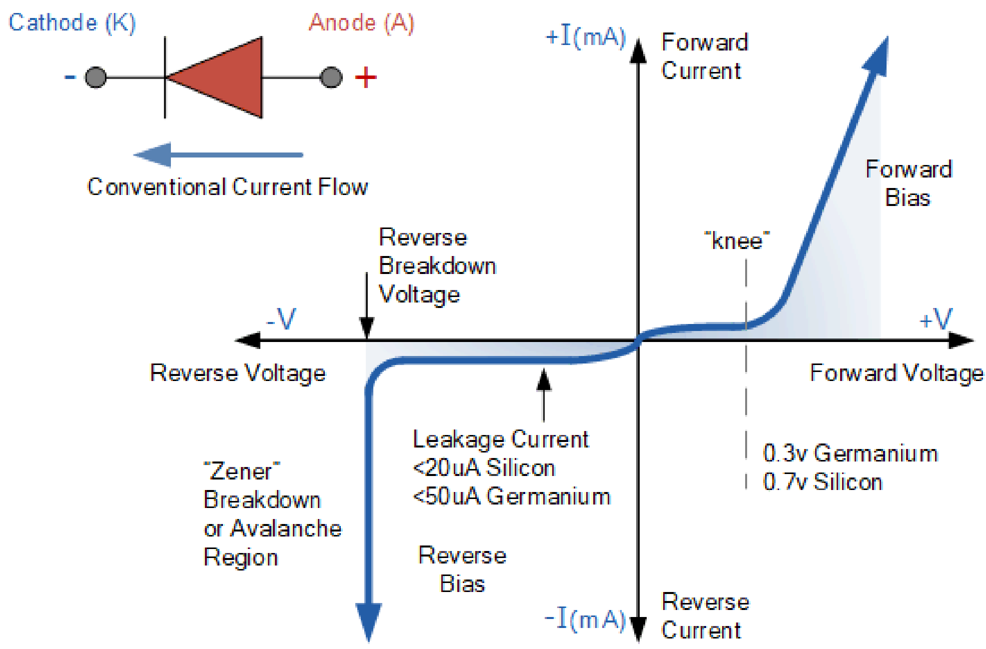

Figure 1-13: Diode *I-V* curve characteristic

1.5 Photovoltaic Effect

When the solar cell (p-n junction) is subjected to sun-light, electron-holes pairs are generated, resulting in the creation of a *photo-generated current*. In particular, in order for this process to occur, it is necessary that the incident photons have sufficient energy to overcome the band gap of the semiconductor material that compose the p-n junction.

$$E_{ph} = \frac{h \cdot c}{\lambda} \geq E_{gap} \tag{1-10}$$

Moreover, because of the electric field that already exists inside the p-n junction, the generated holes and electrons move in the opposite direction as what is expected, which means that the electrons are attracted toward the N-type layer whilst the holes are attracted to the P-type layer. Even in the absence of an external voltage, if the external circuit is closed (short circuit configuration), the photo-generated current continues to flow. On the other hand, in open circuit, there is an increment in the diffusion current since the flowing of the photogenerated current tends to decrease the electric field due to the recombination phenomena. These two currents tend to balance each other reaching an equilibrium configuration.

Considering this additional term, equation (1.8) can be rewritten by subtracting the photo-generated current I_{ph} from the diode current under dark conditions. The overall cell current that flow inside an illuminated p-n junction is given by the following formula:

$$I = I_0 e^{\left(\frac{V}{n\, V_{th}} - 1\right)} - I_{ph} \tag{1-11}$$

Where:

- I_0 (A), is the saturation current.
- n, is the diode ideality factor.
- V (V), is the voltage.
- $V_{th}(V)$, is the thermal voltage
- $I_{ph}(A)$, is the photogenerated current.

Moreover, the photogenerated current can be modelled considering the characteristics of the incident radiation. Its expression is the following, where the integration limits are related to the portion of the solar spectrum which is exploitable by the solar cell:

$$I_{ph} = A \int g(\lambda) \cdot SR(\lambda) \cdot d\lambda = A \cdot G \cdot k_{mat} \tag{1-12}$$

Where:

- A (m^2), is the surface of the cell.
- $g(\lambda)$ is the solar spectrum, which is a function of the wavelength.
- G $(\mathrm{W/m^2})$, is the irradiance. It is given by the integration of the solar spectrum.
- $SR(\lambda)$, is the spectral response . It is the ration between the electron charge and the photon energy and is a linear function of the wavelength.
- k_{mat}, is the average spectral response, which is a specific parameter of the material composing the solar cell.

1.6 *I-V* Curve

The *I-V* curve of the solar cell is the best tool to describe the behaviour of a solar cell for any given couple of irradiance and temperature. Moreover, from the *I-V* curve it is possible to compute the corresponding P-V curve by simple computation of the power as:

$$P = V \cdot I \tag{1-13}$$

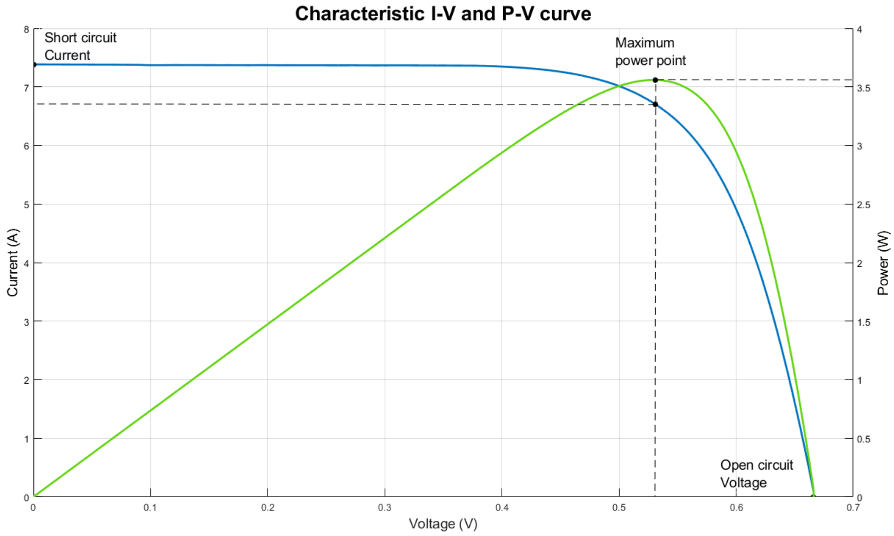

Figure 1-14: Characteristic *I-V* and P-V curve for a high efficiency solar cell

An example of the classical *I-V* curve for high efficiency solar cells is presented in figure (1-13). It is possible to identify three main points, which are highlighted in the graph:

- *Short circuit point* $(0,I_{sc})$: is associated with the highest current since the load connected to the solar cell is null.
- *Open circuit point* $(V_{oc},0)$: is the voltage across the internal diode when no external current flow is observed and all the photogenerated current flows inside the diode. It is the equilibrium condition between the photogenerated current and the diffusion current. Crystalline silicon solar cells have typical values around 0.6 V. It is not useful to provide power.

- *Maximum power point* (V_{mpp},I_{mpp}): is the point of the curve associated with the maximum power production. It is the most useful point of operation and it is usually the point in which the P-V module works under nominal conditions since it is where the maximum power can be extracted. The maximum power can be analytically estimated exploiting equation (1-13), by performing the derivative over the voltage:

$$\frac{dP}{dV} = \frac{d(V \cdot I)}{dV} = V \cdot dI + I \cdot dV = 0 \tag{1-14}$$

$$\frac{I}{V} = -\frac{dI}{dV} \tag{1-15}$$

From equation (1-13) it is possible to extract the optimum load resistance since in order to transfer the maximum power from the generator to the lead, the internal resistance of the PV generator must be equal to the load.

$$R_{load,optimal} = \frac{V_{mpp}}{I_{mpp}} \tag{1-16}$$

It is important to mention that the real *I-V* curve lays also in the second and third quadrant (figure (1-15)), as there are particular conditions in which the solar cell can behave like a load, absorbing power. This can happen when the solar cell is subjected to shading or mismatch phenomena.

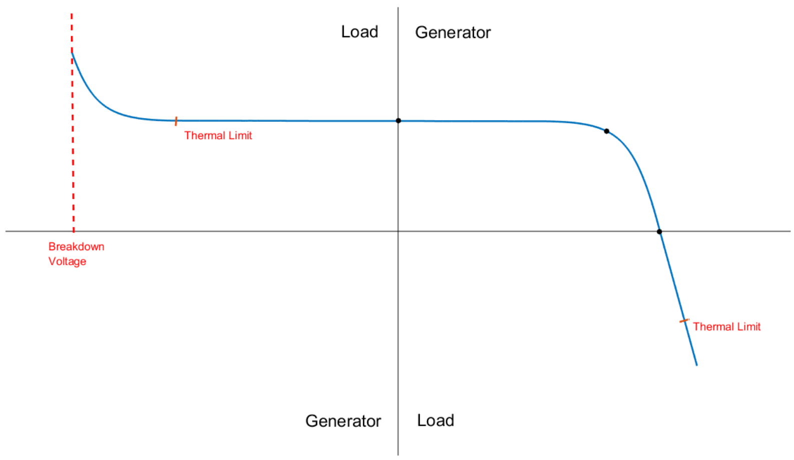

Figure 1-15: Complete characteristic *I-V* curve

- In the first quadrant the solar cell behaves like a generator. The curve correspond to the normal *I-V* curve shown in figure (1-13) and it is possible to identify the main points previously mentioned.
- In the second and third quadrant the solar cell behaves like a load. There is a reverse voltage and a reverse current respectively, and the power is absorbed. It is possible to identify the two thermal limits, after which the the cell is not able to work without getting damaged, and the breakdown voltage, that causes istant failure of the cell

In addition to the most important points already discussed, from the *I-V* curve it is possible to extract a series of important parameters, such as the fill factor and the efficiency.

The *fill factor* is a useful parameter that gives information about the amount of the available energy can be exploited. The higher is this parameter and the higher is the quality of the solar cell. Typical values of the fill factor are around 0.8,0.9. It is given by the following formula:

$$FF = \frac{V_{mpp} \cdot I_{mpp}}{V_{oc} \cdot I_{sc}} \tag{1-17}$$

Where:

- V_{mpp} (V), is the voltage at maximum power point.
- I_{mpp} (A), is the current at maximum power point.
- V_{oc} (V), is the open circuit voltage.
- $I_{sc}(A)$, is the short circuit current.

The *solar cell efficiency* is a measure of the goodness of the power conversion inside the cell. Typical values are around 20% depending on the technology. It is given by the ratio between the electrical power delivered to the load and the power of the solar radiation incident on the solar cell. It can be estimated with the following formula:

$$\eta_{solar\ cell} = \frac{P_{max}}{P_{in}} = \frac{I_{mpp}V_{mpp}}{G \cdot A} = \frac{FF\ I_{sc}V_{oc}}{G \cdot A} \tag{1-18}$$

Where:

- V_{mpp} (V), is the voltage at maximum power point.
- I_{mpp} (A), is the current at maximum power point.
- G $\left(\frac{W}{m^2}\right)$, is the incident solar radiation.
- A (m^2), is the area of the solar cell.
- V_{oc} (V), is the open circuit voltage.
- $I_{sc}(A)$, is the short circuit current.
- FF, is the fill factor.

The efficiency of solar cells is limited by many losses, some of which are not avoidable and intrinsic to the system:

1. Not all incident photons can penetrate into the cell as some of them are reflected or absorbed. The frontal electrodes cover partially the active surface of the solar cell, thus blocking part of the incident radiation. Moreover, without any special precaution semiconductors materials are very reflective. Normally about 40% of the incident radiation is lost but with thin-film surfaces the reflection can be reduced to 3%.
2. Photons with an energy lower than the band gap cannot generate photovoltaic effect and thus a big portion of the solar spectrum is lost. For typical Si-modules around 23% of the spectrum is not exploitable.
3. Photons with an energy higher than the band gap dissipate the surplus of energy through heat generation. Typical values of this losses are around 25%.
4. There is a small portion of photons that are not able to generate electron-hole pairs even if they are absorbed. This loss is very low (around 5%) and is usually measured by the quantum efficiency.
5. Not all the photo-generated electron-hole pairs are able to produce a useful current in the external circuit. Usually this loss is around 30% for solar cell with 10% overall efficiency.
6. Some electron-hole pairs recombine themselvesl inside the p-n junction before they can be separated by the electric field. The recombination phenomena are more likely in the presence of defects in the semiconductor material.
7. The electric insulation of the lateral surface is imperfect and can cause a leakage current which is what causes the *I-V* curve to have its shape and not a rectangular one. They constitute around 20% of the total losses.

1.7 Dependence on Temperature and Irradiance

The behaviour of a solar cell is strictly related to the external atmospheric conditions. In this sense, the first aspect to take into consideration is the relation between the behaviour of the solar cell and the photovoltaic effect. As the photon flux increases, the electron flux increases as well, which means that the shape of the characteristic *I-V* curve is strongly related to the specific conditions of the photons reaching its surface, such as irradiance. Moreover, since the solar cell is made of semiconductor material, its behaviour will depend strongly on the temperature of the solar cell. At higher values of temperature, the energy gap of the material is reduced and therefore the exploitable portion of the solar spectrum increases.

The effects of the variation of these two parameters on the shape of the *I-V* curve are presented in figure (1-16) and (1-17).

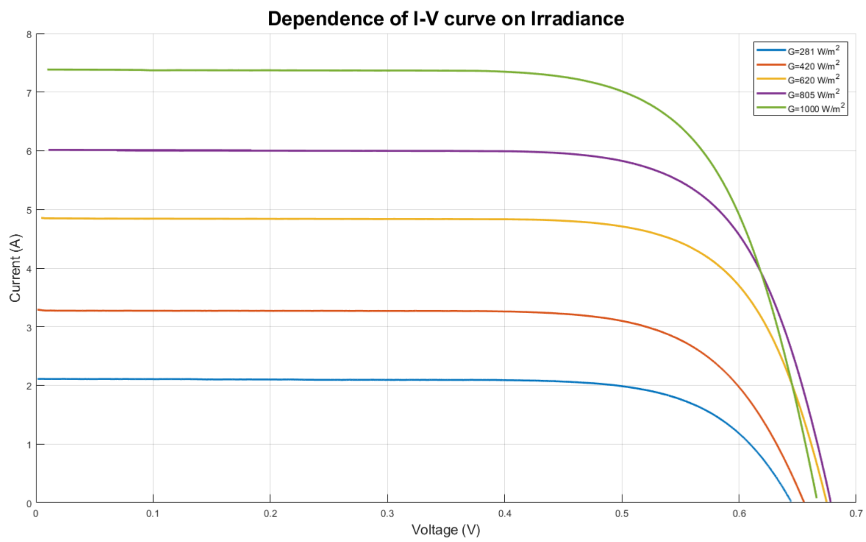

Figure 1-16: Influence of Irradiance on the *I-V* curve.

In particular, focusing on the effects of the irradiance, it can be observed that:

- The short circuit current and the maximum power point current increase proportionally with irradiance. This behaviour is related to the fact that the short circuit current is stricly related to the photogenerated current, which is proportional to the irradiance as shown in equation (1.12).

- The open circuit voltage increases proportionally with irradiance. Moreover, it can be proven that there is a logarithmic dependance between the values of irradiance and the open circuit voltage. Using equation (1.11) applied to the open circuit condition, it is possible to obtain:

$$0 = I_0 e^{\left(\frac{q\,V_{oc}}{n\,k\,T}-1\right)} - I_{ph} \tag{1-19}$$

  From this equation it is possible to obtain the following formulations which proves the logaritmic dependence as the photogenerated current is proportional to the irradiance.

$$V_{oc} = \frac{n\,k\,T}{q} \ln\left(\frac{I_{ph}}{I_0}\right) \propto \ln\left(G\right) \tag{1-20}$$

  Consequently, the variation of the open circuit voltage is almost negligible at higher values of irradiance and increases for lower irradiances, as can be observed in figure (1.16). Furthermore, the same dependance can also be observed for the maximum power point voltage.
- As a consequence, the maximum power increases with increasing irradiance.

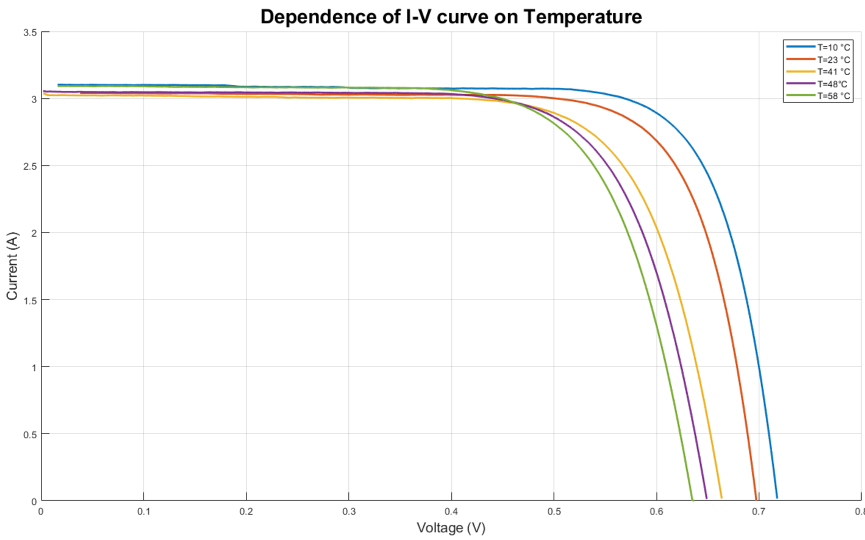

Figure 1-17: Influence of Temperature on the *I-V* curve

Moving on the effects of Temperature variation on the *I-V* curve, it is possible to observe that:

- The short circuit current and maximum power point current are almost constant. Since the effect of Temperature is strictly connected to the diode behaviour and little to the photogenerated current. Nonetheless, a small decrease can be observed as the temperature increases.
- The open circuit voltage and the maximum power point voltage on the other hand, are strictly related to the temperature variation. They decrease proportionally as temperature increases
- As a consequence, the maximum power decreases proportionally as temperature increases as well.

Finally, this dependence of the most important points with irradiance and temperature, can be expressed as follows with the following equations:

$$I_{sc} = I_{sc,STC} \cdot \frac{G}{1000} [\cdot 1 + \alpha \cdot (T - 25)] \tag{1-21}$$

$$V_{oc} = V_{oc,STC} \cdot [1 + \beta \cdot (T - 25)] \tag{1-22}$$

$$P_{max} = P_{max,STC} \cdot \frac{G}{1000} \cdot [1 + \gamma \cdot (T - 25)] \tag{1-23}$$

Where:

- $I_{sc,STC}$ (A), $V_{oc,STC}$ (V), and $P_{max,STC}$ (W) are respectively the short circuit current, the open circuit voltage and the maximum power in standard test conditions, provided by the manufacturer.
- G $\left(\frac{W}{m^2}\right)$, is the irradiance.
- T $(°C)$, is the temperature.
- α, β and γ are the thermal coefficients that correlate the corresponding parameter variation (I_{sc}, V_{oc} and P_{max}) to the temperature variation. They depend strictly on the technologies and are provided by the manufacturing datasheet.

1.8 Equivalent Circuit

The behaviour of a solar cell can be represented schematically using an electric circuit approach. Different models based on the *I-V* characteristic curve of a PN junction are presented in literature. As previously stated, in these models there are two currents that need to be represented: one associated with the generation of the electron-hole pairs called photogenerated current and one associated with the diffusion of electrons and holes across the junction, called saturation current. In addition, in these models are typically included series and parallel electrical resistances to take into account the internal and external losses caused by the interconnections of cells and by leakage through the lateral surfaces

The simpler and most used model known is the single diode model, but there are many other that are more complex and have a higher level of accuracy and physical meaning. However, for the purpose of this study, the single diode model has been employed due to its simplicity. For this reason, in this sub-chapter an overview of the SDM model will be given.

The equivalent circuit of the single diode model is presented in the figure below.

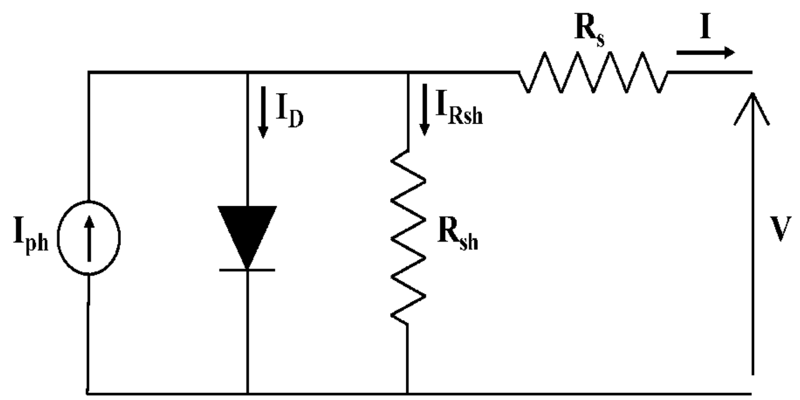

Figure 1-18: Equivalent circuit for Single diode model with 5 parameters [5]

The main components of the equivalent circuit are:

- *Ideal current generator* to represent the photogenerated current.
- *Antiparallel diode* through which the diode current flows. It represents the straightening effect of the electric field generated inside the p-n junction. To take into account the real behaviour of the p-n junction, the diode is associated with a diode ideality factor n. This parameter contains informations about the charge transport and the recombination process which occurs inside a real diode.

- *Shunt Resistance*, placed in parallel with the current generator and the diode. It is due to the non-ideality of the solar cell and it accounts for the leakage current (I_{SH}) over the lateral surfaces caused by not perfect isolation. Ideally the value of this resistance should be infinity to avoid any losses, but in reality it is not possible to achieve this. Nonetheless, its value can be increased by increasing the thickness of the lateral surfaces
- *Series Resistance*, placed in series to the other components in the circuit. It takes into account the losses that occur across the electrical contacts across the frontal electrodes. The main impact of the series resistance is to reduce the fill factor.

Moreover, according to the equivalent circuit shown in figure (1-18) it is possible to write the transcendental equation for any given value of irradiance and temperature by applying Kirchhoff's Law on the equivalent circuit. The implicit formulation of the transcendental equation is the following:

$$I = I_{ph} - I_0\left(e^{\frac{V - R_s \cdot I}{V_{th} \cdot n}} - 1\right) - \frac{V + R_s \cdot I}{R_{sh}} \qquad (1\text{-}24)$$

Where:

- I_{ph} (A), is the photogenerated current.
- I_0 (A), is the saturation current.
- V (V), is the voltage.
- I (A), is the current.
- $R_s(\Omega)$, is the series resistance.
- $R_{sh}(\Omega)$, is the shunt resistance.
- n $(-)$, is the diode ideality factor.

In particular, it can be observed that this model is characterized by five parameters which are: the photogenerated current, the saturation current, the diode ideality factor and the series and shunt resistance. The main issue of the implicit formulation is that it is not possible to express current in the explicit form as it is present both in linear and exponential form. However, an explicit formulation could be particularly useful when dealing with parameters extraction problems. For this reason, in order to obtain the explicit formulation, it is possible to exploit the Lambert function [6]. The Lambert W-function and the explicit form of the transcendental equation are defined as follows:

$$W(x)e^{W(x)} = x \tag{1-25}$$

$$I = -\frac{V}{R_S+R_{sh}} - \frac{W\left(\frac{R_S I_0 R_{sh} e^{\frac{R_{sh}\left(R_S I_{ph}+R_S I_0+V\right)}{nV_{th}(R_S+R_{sh})}}}{nV_{th}(R_S+R_{sh})}\right) nV_{th}}{R_S} + \frac{R_{sh}\left(I_0+I_{ph}\right)}{R_S+R_{sh}} \tag{1-26}$$

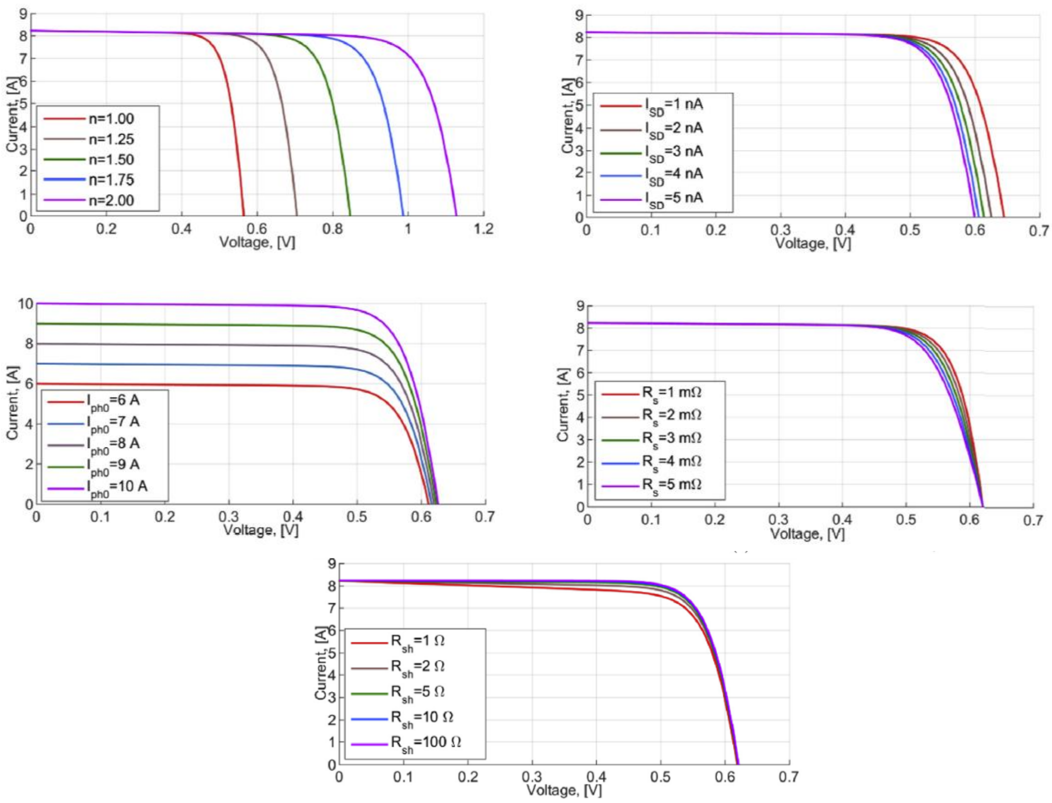

Figure 1-19: Influence of parameters variation on the *I-V* curve [7]

In figure (1-19) the effects of each parameters variation on the overall shape of the *I-V* curve can be observed separately [7] [8]. As expected, the photogenerated current has the highest effect on the short circuit current since the correlation between the two quantity and irradiance is directly proportional. The ideality factor, on the other hand, has the highest effect on the open circuit voltage since with increasing values of n the probability of recombination increases, thus increasing the open circuit voltage. The saturation current has a similar effect on the open circuit voltage too, but its contribution is far more negligible compared to the diode's ideality factor. Focusing instead on the effects of the two resistances, it seems that their variations have an effect mainly on the fill factor as they change the shape of the *I-V* curve near the maximum power point while keeping unaltered the short circuit current and the open circuit voltage. Moreover, it seems that the series resistance has an higher effect on the slope of the *I-V* curve on the vertical portion of the curve (from maximum power point to open circuit), whilst the effect of the shunt resistance is more evident on the horizontal portion of the curve (from short circuit to maximum power point).

1.9 Series and Parallel Connection

The typical power production of a single solar cell is very low since the open circuit voltage is around 0.6-0.7 V. For this reason, solar cells are usually connected in series or in parallel to form a photovoltaic module. This configuration enables to increase the power production of the module to make it comparable with commercial applications.

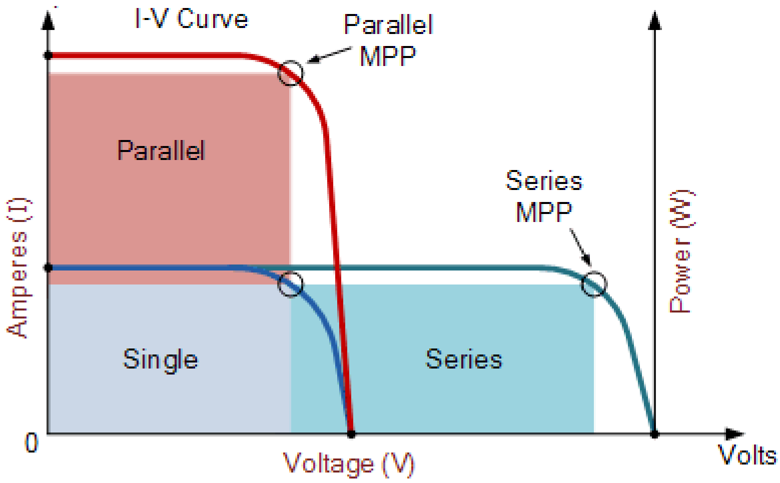

Figure 1-20: Effects of series and parallel connection to the *I-V* curve [9]

In particular, as shown in figure (1-20), in the series connection the overall voltage is given by the sum of the voltages of the connected cells whilst the current is imposed by the cell with the minimum current. Instead, in the parallel connection the behaviour is the opposite. The two behaviours can be summarized as follows:

$$\begin{cases} I_{module} = \min\left(I_i\right) \\ V_{module} = \sum_{i=1}^{N_S} V_i \end{cases} \qquad for\ series\ connection \tag{1-27}$$

$$\begin{cases} I_{module} = \sum_{i=1}^{N_P} I_i \\ V_{module} = \min\left(V_i\right) \end{cases} \qquad for\ parallel\ connection \tag{1-28}$$

Where:

- N_S, is the number of series connected cells.
- N_p, is the number of parallel connected cells.
- I_i, is the current of the i-th cell.
- V_i, is the voltage of the i-th cell.

However, an important issue arises when connecting cells with different electrical characteristics that lead to mismatch phenomenon that can cause significant power losses. [10] In fact, it is paramount to connect modules with similar *I-V* characteristic in order to reduce as much as possible these losses since the output of the entire PV module is determined by the cell with the lowest output. Moreover, cells need to have similar electrical properties as well as similar irradiance conditions. The mismatch phenomenon will be discussed in detail in the following sub-chapters, focusing on the main causes and the main consequences.

1.9.1 Causes of Mismatch

As previously stated, the mismatch phenomenon affects cells connected in series or parallel that present different *I-V* curves. The main reasons that could lead to these differences are the following:

1. *Production tollerance*: this is an intrinsic cause of loss as it is not possible to repeat perfectly the parameters in the manufacturing process, so the parameters do not have exactly the same electrical behaviour. This is

usually related to the presence of defects inside the structure of the material, which are not complitely avoidable. Moreover, usually manufacturers divide modules according to different categories associated with different tollerance values. This is useful to avoid connecting modules belonging to different tollerance classes and avoid mismatch effects.

2. *Presence of defects due to degradation or damage during production and transport*. The presence of micro-fractures or broken contacts affects greatly the performance of the solar cell subjected to this defects, but also those connected to it.
3. *Shading effect*: this is an external cause of loss but also one of the most severe since it can lead to the total obscuration of the cell. The shading can be partial or total and can be caused by nearby trees or building, as well as by the deposition of dust or snow over the surface of the module.

1.9.2 Mismatch of cells connected in series

Series connection is particularly useful to increase the overall voltage of the connected cells as shown in equation (1.27). However, when one cell in the connection is defected, the overall current will be limited by the defected cell, thus reducing the overall power output. Moreover, depending on the severity of the mismatch the losses can be more or less significant. In addition, whenever the defected cell has a current that is a lot lower compared to those to which is connected, local hot spot phenomena could arise since the defected cell operates as a load and no longer as a generator and in some situation the breakdown voltage could be reached. In fact, even if in the external circuit the current is imposed by the defected cell, the 'good' cells are still producing their typical current. Since it cannot flow in the external circuit, this current is 'forced' inside the shaded cell, that results in reverse voltage across the shaded cell (works in the 2^{nd} quadrant). This phenomenon becomes more critical as the mismatch increase and it is worst in case of totally shaded cell. In this case, the hot spot phenomenon could be so severe to cause the failure of the solar cell as the thermal limit would be exceeded.

To overcome the issue related to the mismatch phenomenon in series connections, *bypass diodes* are usually added every 20 cells. They are connected antiparallel to the cell in the direction of the photogenerated current such to avoid the presence of high voltage difference in the reversed-bias configuration. Moreover, whenever the bypass diode is active, the power is optimized as the defected cell no longer has an impact on the overall output of the connected cell.

The typical shape of the *I-V* curve with bypass diode is presented in figure (2-22): the effect of the bypass diode is noticeable by the presence of the two maximums. When the diode is off, the current is imposed by the defected cell. However, as the current increase, increasing the voltage drop in the defected cell, the diode is switched on and the current generated by the 'good' cells is now able to flow in the external circuit producing a useful output.

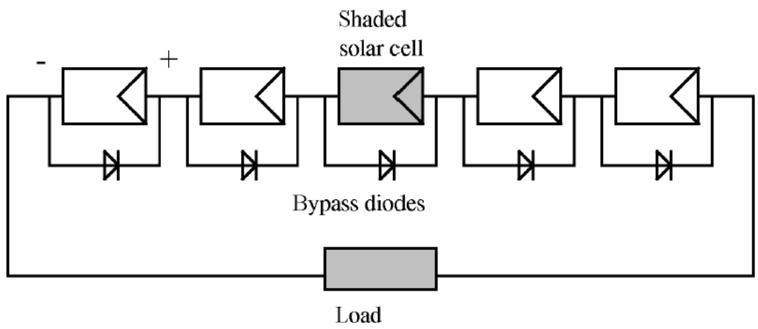

Figure 1-21: Series connection of solar cells with bypass diode. [4]

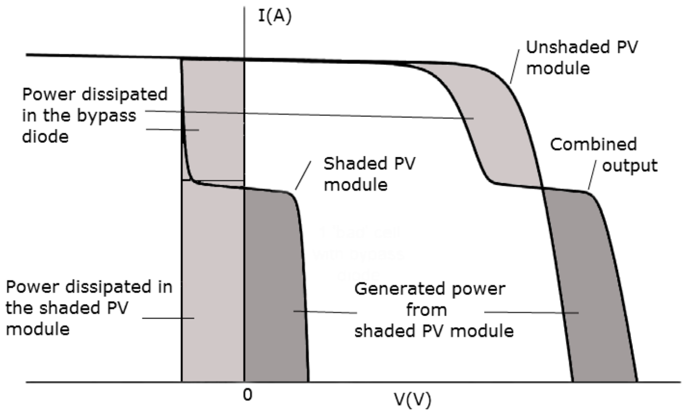

Figure 1-22: Effect of bypass diode on combined *I-V* curve with one shaded. [11]

1.9.3 Mismatch of cells connected in parallel

Similarly to what has been discussed for the series connection, in case of parallel connected the voltage value is limited by that of the defected cell. As the mismatch becomes severe, the defected cell will be subjected more and more to a reverse current (4th quadrant) generated the real voltage difference produced by the 'good' cells. In the worst case possible (totally shaded cell), the cell would be subjected to a very strong reverse current that could lead to failure if the thermal limit is exceeded.

It is important to notice that usually parallel connections are not very used to connect cell in a module. In fact, this connection is typically applied to large arrays of modules to connect different strings with each other. Nonetheless, the mismatch phenomenon is addressed by adding a *blocking diode* in series with each string. Contrary to the bypass diode, the blocking diode is always active and causes some losses. However, its presence is necessary to block eventual reverse current to flow inside the shaded string in order to guarantee good performance of the P-V arrays.

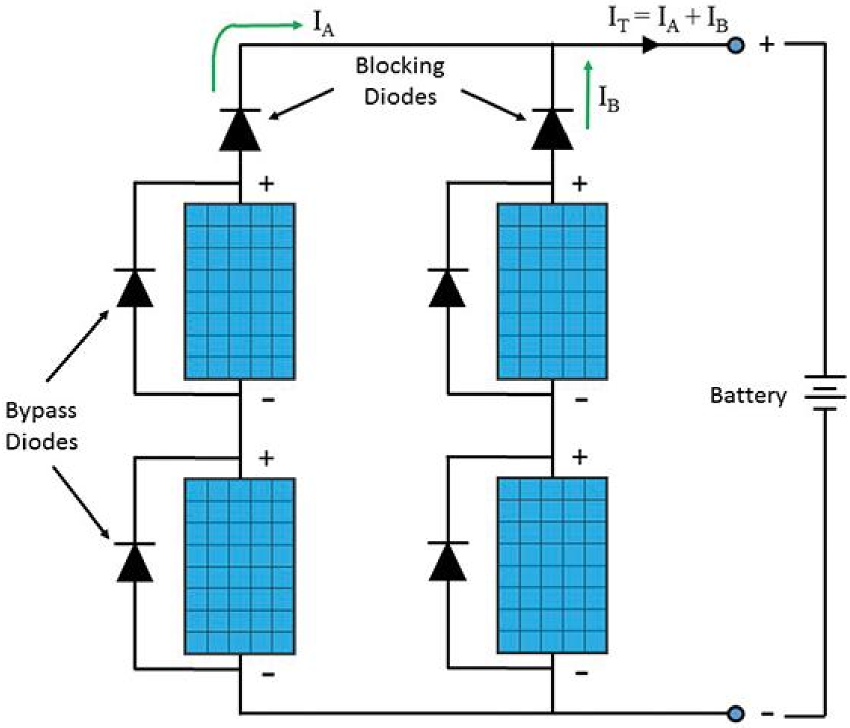

Figure 1-23: Typical configuration of PV arrays with bypass and blocking diodes. [12]

Chapter 2

Photovoltaic Modules

2.1 Structure of a PV Module

As the previously chapter stated, the solar cell is the most important component of a PV module. There are, however, other components that are usually included in the conventional design, shown in figure (2-1).

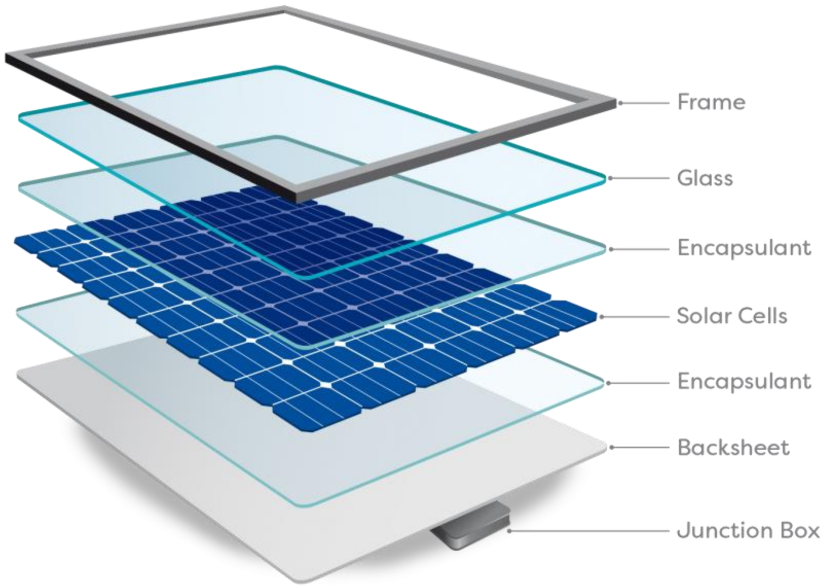

Figure 2-1: Typical design of conventional PV module [13]

In particular, it is possible to identify the following layers:

1. *Junction Box* containing the bypass diodes and the connectors. It is basically a small weather proof enclosure located on the back side of the module. It is where the connection between the module and the external circuit occurs, thus it needs to be protected from moisture and dirt to guarantee correct functioning.
2. *Polymeric rear backsheet*, usualy made of PP, PET or PVF (Tedlar). The main role of this layer is to act as a moisture barrier while simultaneously provide mechanical protection and electrical insulation. In some module,

the polymeric layer is substituted with a rear glass panel since it is more durable compared to typical backsheet materials.

3. *Solar photovoltaic cells*. The number of cells connected in series depends on the dimension of the solar panels, typical values for crystalline technologies range between 60-96 cells. Usually, in the manufacturing process the p-n junction is treated with an anti-reflective coating that adapts the silicon and glass refraction indices. In addition, each cell is equipped with rear and front contact, that consist of a flat electrode plate in the rear side and a combination of busbars and fingers in the front side. This contacts are necessary to connect the different cells with each other and to create the external circuit in which the generated current can flow.
4. *Encapsulant layer*, usually made of high quality EVA (Vinyl Ethylene Acetate). The encapsulation process is achieved through lamination under vacuum condition on either sides of the PV-cells. This is done to prevent penetration of humidity and dirt, which is crucial to guarantee the long term performance of P-V modules. Moreover, this layer provides shock absorption and helps protect the cells from vibration and sudden impact (e.g hail) which could lead to their distruption.
5. *Tempered Front Glass*. The role of this layer is to withstand the numerous external environmental agents, such as hail, snow, wind or dust and protect the solar cells. Usually this layer is made of high transmissive glass, in order to improve efficiency and performance by enhancing the light transmission and reducing the optical losses.
6. *Aluminium Frame*. This is the outer layer and also one of the most important one since its role is to guarantee the structural integrity of the module and to to provide a solid structure for mounting purposes. Usually a sealant gasket is necessary to increase the electrical insulation between the frame and the module.

Lastly, it is important to mention that the global efficiency of PV-module is usually lower than that of a single solar cell since there are many additional losses that are introduced with the construction of the module. In particular, the overall efficiency can be given by the following formula:

$$\eta_{module} = \eta_P \cdot \eta_{sc} \cdot \eta_T \cdot \eta_{MIS} \cdot \eta_{IM} \tag{2-1}$$

Where:

- η_P, is the filling efficiency which takes into account the inactive frontal surface that cannot be exploited for the conversion of the solar radiation into electricity. This loss is related to the fact that when connecting togheter the solar cells it is not possible to avoid some inactive spaces.
- η_{sc}, is the typical conversion efficiency of a solar cell without considering the EVA or the glass layer.
- η_T, takes into account the absorbtion losses caused by the glass cover materials.
- η_{MIS}, takes into account the intrinsic mismatch of module, since they are made of solar cells connected usually in series.
- η_{IM}, takes into account for the non-homogeneity of the incident radiation over the module surface.

2.2 Technical Specifications

Usually there are many different specifications that are associated with a PV-module datasheet. The goal of a technical datasheet is to provide concise and useful information about the performance of the PV-module. In this sense, there are a series of information that are usually provided, such as the main electrical parameters, the thermal coefficients and the technological and mechanical specifications (e.g. dimensions, materials, number of cells connected and so on). Examples of typical datasheet are provided in Annex A, for the modules used in this study.

In particular, it is important to specify the two main test conditions under which the module is tested to obtain these parameters: STC and NOCT.

Standard test conditions refer to the specific standardized conditions in which the modules are tested to obtain the main information about voltage and current ($I_{sc}, V_{oc}, P_{max}, I_{mpp}, V_{mpp}$). The STC conditions are defined in IEC/EN60904 to guarantee that all modules are characterized under the same conditions. Specifically, STC conditions consist of:

- $G = 1000 \frac{W}{m^2}$
- $T = 25\ °C$
- $AM = 1.5$

'NOCT' stands for *Nominal Operating Cell Temperature*. This temperature is the equilibrium temperature reached by open circuited solar cells inside a module, exposed to the sun, in standardized conditions ($G = 800 \frac{W}{m^2}, T_a = 20°C,\ v_{wind} = 1 \frac{m}{s}$). It is given by the following formula:

$$T_c = T_a + \frac{NOCT - 20}{800} G \qquad (2\text{-}2)$$

Where:

- $T_a\ (°C)$, is the ambient air temperature.
- $NOCT\ (°C)$, is the NOCT temperature. Its value is usually provided by the manufacturer.
- $G\ \left(\frac{W}{m^2}\right)$, is the irradiance.

This formulation is useful to determine the temperature of the solar cell at any given value of irradiance. One of the main issues, however, is that further from the standardized conditions for which this formulation is valid, equation (2-2) loses some of its physical meaning. Nevertheless, it is a great tool that can be used to compare the measured values of temperature with the expected one, as it will be shown in chapter 5.

2.3 Main Photovoltaic Technologies

Due to the rising interest in renewable resources, the market for P-V technologies presents a wide range of different technologies exploiting the photovoltaic principle. Starting from the classical crystalline silicon technologies, recent studies and innovations have found new well-developed PV-technologies exploiting different materials. In the following sections , an overview of the dominant technologies present in the market will be given, comparing them in terms of manufacturing and installation cost, energy payback time and efficiency.

A first classification can be made depending on the material used and the level of commercial maturity [14]:

1- First generation: consist of crystalline based silicon technologies, such as monocrystalline and polycristalline.

2- Second generation: consist of thin-film technologies, which include three main families (CdTE, CIGS and amorphous silicon).
3- Third generation: consist of technologies thare are still under demostration and are not yet commerciable, such as organic PV cells or concentrating PV.

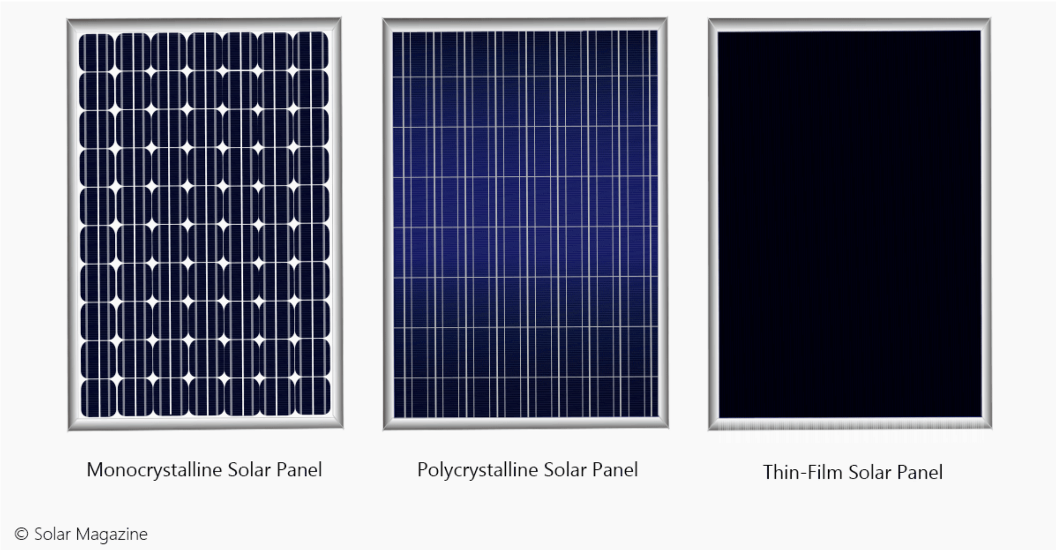

Figure 2-2: Main P-V module technologies [15]

2.3.1 Monocrystalline Silicon Solar cells

Monocrystalline solar cells are the oldest type of solar cell. As the name suggests, they are made of pure crystalline silicon, characterized by the absence of defect and a continuous lattice. Due to the high purity, these types of solar cells are characterized by high efficiency, which usually ranges between 20-24% depending on the specific technology.

As shown in figure (2-2), typical monocrystalline cells are characterized by a black or iridescent blue colour and the characteristic shape with rounded corner. This is related to the manufacturing process necessary to obtain monocrystalline silicon. Due to this aspect, these modules are characterized by a high percentage of inactive surface. Moreover, the monocrystalline solar cells are considered very durable and can last up to 25 year, guaranteeing 80% of the initial power.

Nonetheless, as previously mentioned, they are very expensive due to the difficult manufacturing process and are characterized by great mechanical vulnerability. In fact, they are characterized by the higher payback time, which is around 2-3 year depending on the location This is what prompted researche in new more feasible alternatives.

2.3.2 Polycrystalline Silicon Solar Cells

Polycrystalline solar cells are made of multi-crystalline silicon. Due to the manufacturing process and the higher percentage of impurities they are less efficient compared to the monocrystalline technology. In fact, typical values of efficiency are around 14-16%. However, for this same reason the manufacturing cost is reduced remarkably guaranteeing an energy payback time below 2 years.

As shown in figure (2-2), they are characterized by a blue colour due to the way they are manufactured. In addition, the single solar cells are square and do not present the large white spaces present in monocrystalline panels. The durability is similar to that of the previous technology, as they should last for more than 25 years.

2.3.3 Thin Film Solar Cells

Thin film solar cells are produced by depositing one or more thin layers of photovoltaic material on a substrate, which can be made of glass or of metal. They are completely different from the previously mentioned technology as they are often characterized by flexibility and lightweight, as well as high transparency to light. Moreover, as shown in figure (2-2), they are solid black and lack the typical cell's outlines present in crystalline technologies. The manufacturing procedure usually involves high temperature deposition techniques.

The thin films technology is usually employed for large scale operation since it is characterized by the lower efficiency ratings. For commercial module typical efficiencies are around 8%-13% depending on the technology. In addition, there is also a secondary issue related to the durability, since they have a shorter lifespan compared to other types of solar panels since they degrade quicker. Nonetheless, they are also characterized by the lowest cost and they are easier to install.

In particular, there are four main thin-films technologies employing different materials:

- *Cadmium Telluride* (CdTe). This is the predominant thin film technology and it is characterized also by the higher efficiency (around 13-15%). In addition, this technology is characterized by the lowest energy payback time of 8 months or even less. The main issues of this technology are the toxicity of cadmium and the rarity of tellurium. This could be a limiting factor for the market share of this technology.

- *Copper Indium Gallium Selenide* (CIGS). This is the second most used thin film technology and it is characterized by efficiencies around 11-13% and an energy payback time around 1 year.
- *Amorphous Silicon* (a-Si): This is the third most used thin film technology. It uses non-crystalline Silicon as deposited layer. Its main advantage compared to the other thin films technologies is related to the high abundance of silicon, even though typical efficiency is usually lower (around 6-10%). The energy payback time is comparable with that of polycristalline technologies.

2.3.4 Heterojunction with Intrinsic Thin Layer (HIT) Solar Cells

HIT solar cells are an evolution of the classic monocrystalline solar cells. In this sense, a thin mono-crystalline silicon wafer is inserted between two thin amorphous silicon layers, as shown in figure (2-3). With this configuration it is possible to reduce the defective area in the internal structure, improving the performance of the modules. Moreover, this technology is able to guarantee high performance even at high temperatures compared to conventional crystalline silicon solar cells.

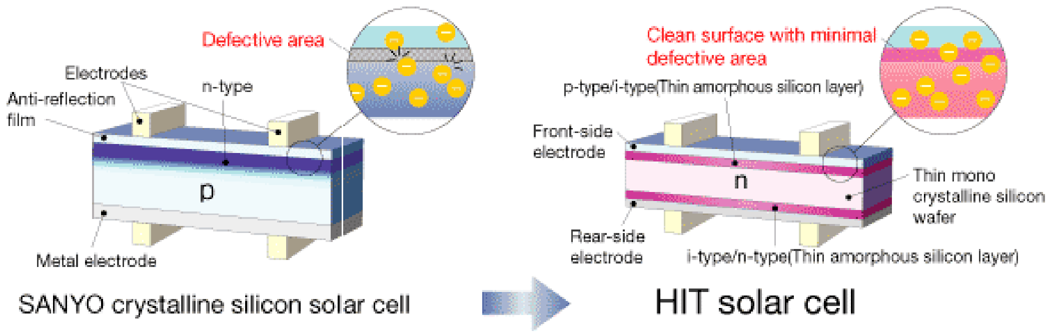

Figure 2-3: Comparison between HIT and crystalline solar cell. [16]

Chapter 3

Innovative procedure to estimate the performance of PV modules

The aim of this study is to develop an innovative technique that is able to accurately predict the behaviour of a PV module according to different environmental conditions. Moreover, this new proposed model will be compared with another known model to check for its validity and usefulness for future applications. In this sense, three approaches have been used to estimate the performance of PV modules:

- The first two approaches are related to the estimation of the electrical parameters to compute the *I-V* curve for any given couple of irradiance and temperature. Two new empirical models will be extracted from the experimental measurements with this innovative technique. What differs in the implementation of the two models is the application of two different optimization algorithms to extract the parameters, but the overall procedure is the same for both.
- The third approach utilizes the Osterwald method which is a theoretical model known in litterature.

In this chapter, a brief and general description of the innovative technique used to estimate the empirical models will be provided in the first section. Moreover, an overview of the procedure used for the validation of the proposed model and the estimation of the produced PV energy will be provided in the second section. A more detailed discussion will be then provided in the following chapters.

3.1 Estimation of the empirical models

In order to predict the behaviour of photovoltaic modules is paramount to analyse the electrical response of said module to different environmental and operating conditions. In particular, the innovative technique presented in this study is based on the existing correlation between the electrical parameters of the equivalent circuit and the shape of the *I-V* curve at different values of irradiance and temperature. In this sense, the parameters of the corresponding equivalent circuit have been extracted using different methods, which will be thoroughly discussed in chapter 5. These parameters can be used to define an equation (1.23) that is able to model the characteristic *I-V* curve of the module.

In the study presented in this thesis, the single diode model with five parameters has been used to represent the equivalent circuit due to its simplicity and accuracy compared to the other models. An overview of the model and the different parameters, as well as of the corresponding transcendental equations, has been provided in previous chapters (see 1.8). The goal of the first part of the analysis is to find for each available measure a set of experimental parameters that are able to approximate as best as possible the corresponding measured *I-V* curve. Furthermore, by accurately evaluating these parameters for a large amount of data, at different operating conditions, it will be possible to estimate how the performance will vary with irradiance and temperature.

Firstly, one of the main challenges that needs to be addressed is that the parameters extraction of solar cell models is a non-linear, multi-variable, and multi-modal problem with many local optima. Generally, in literature, there are mainly two types of approaches used for the purpose of parameters extraction of solar cells: analytical and numerical methods. With analytical methods the parameters of the equivalent circuit are calculated directly by solving a system of analytical equations. The main issue of this kinds of methods is that they require many assumption and simplifications to obtain an analytical equation that can be used to solve the problem, which may lead to a lower accuracy of the results. On the other hand, numerical methods allow the parameters to be extracted through a series of iterations on a certain equation that describes the problem in analysis (objective function). This is achieved using specific optimization algorithms. The main issue of this kinds of methods is that even though they potentially guarantee a higher accuracy of the results, they require a higher computational cost and may be very dependent on the set of initial parameters guessed. For this reason, using only analytical extraction techniques may prove difficult to extract accurately the parameters without applying too many simplifications and assumptions. But at the same time, using only numerical extraction techniques may not be feasible for the high computational cost that they require and the potential inaccuracy of the results, which are strongly dependent on the initial set of parameters guessed. To overcome this issue, analytical methods can be coupled with more complex numerical methods to achieve the best solution in terms of computational cost and accuracy.

For the sake of this thesis, the whole extraction procedure was implemented in MATLAB using an ad hoc GUI developed for this specific application.

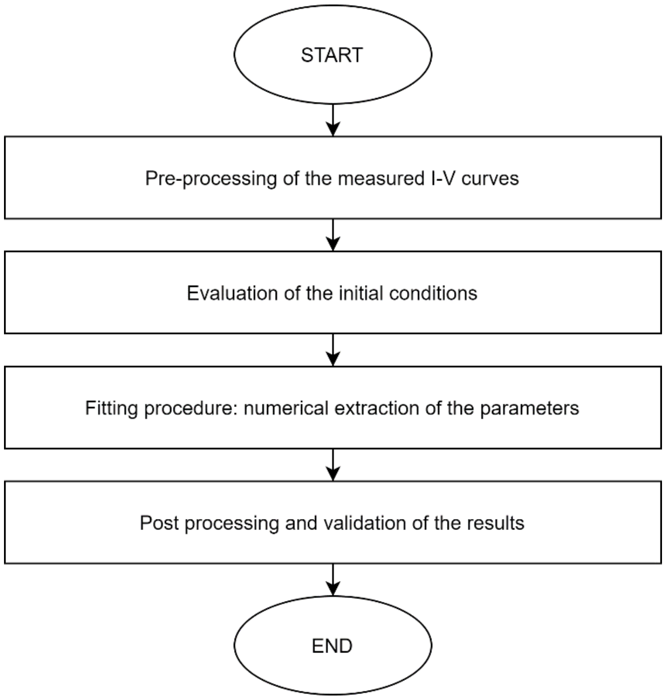

Figure 3-1: Flowchart of the parameter extraction procedure

As shown in figure (3-1), the implementation of the overall extraction procedure can be divided in four main steps:

1. Pre-processing of the curves, to obtain from the measured data the clean *I-V* curves and remove those curves that were not interesting for this analysis due to shading phenomenon.
2. Evaluation of the initial conditions.
3. Fitting procedure, to extract the parameters with the selected optimization algorithm.
4. Post-processing and validation of the results.

The last step is necessary to check the quality of the obtained parameters. This is done considering the resnorm and the percentage error on the maximum power. Furthermore, one of the main problems to take into consideration regarding the parameter extraction procedure is called *‘overfitting’* and is related to the fact that it is possible to obtain more than one set of parameters that are able to solve correctly the transcendental equation and simultaneously accurately minimize the objective function. Therefore, parameters without real meaning could be obtained, hence why the results need to be filtered and validated before proceeding forward in the analysis.

Moreover, the set of extracted parameters is used to obtain some empirical correlations that can predict the behaviour of the various electrical parameters with respect to the environmental conditions, such as module irradiance and temperature. In literature, there are many known correlations that aims to do this [17]. The issue with these correlations is that they do not have enough experimental evidence, but they can still be used as a starting point. In this sense, these empirical equations have been used to perform a non-linear regression and find the optimal fitting coefficients that improve the fitting of each electrical parameters. These correlations coupled with the transcendental equation (1-23) of the single diode model, can be used in the empirical model to estimate the performance of PV modules for any environmental condition.

3.2 Power and Energy estimation

The last step of this study consists in the energy estimation, which is achieved through the integration in time of the power at maximum power point. Since the goal of this study is to compare different methods to estimate the energy, the power is estimated according to two different approaches:

- Through the use of correlations, in order to compute the measured *I-V* curve with respect to the estimated parameters.
- Through the Osterwald method.

In this sense, the energy estimation has been done considering four values: the experimental measured value, the one estimated with the Osterwald method and those estimated with the parameter’s correlations. Lastly, a comparison between the experimental values and the estimated ones has been performed to analyse the accuracy of the different methods employed.

Furthermore, the energy estimation process can be divided in four simple steps which will be discussed in detail in chapter 7:

- Pre-processing of the data to guarantee the integrity of the procedure.
- Power computation with the applied models.
- Energy computation.
- Validation of the results.

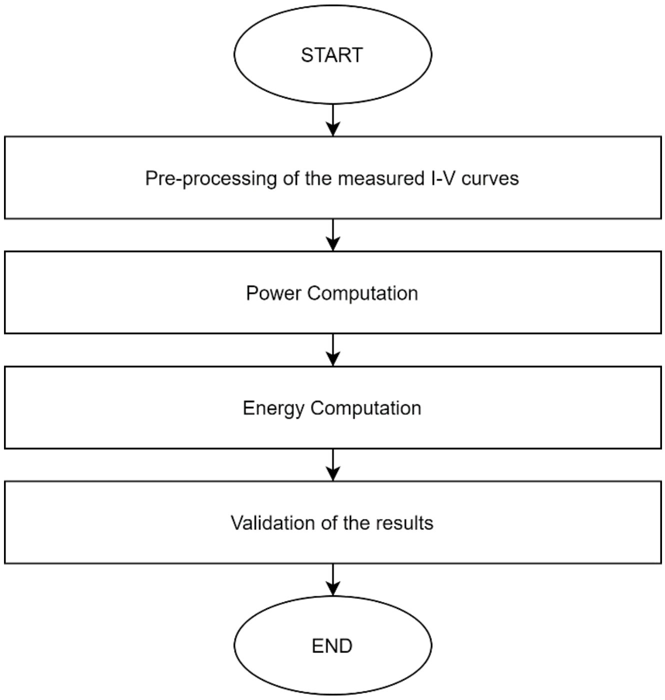

Figure 3-2: Flowchart of the energy estimation procedure

Chapter 4

Data acquisition and pre-processing

The electrical characterisation of the modules in this study was carried out by two different measurement systems: Tracker and Fixed system, respectively. Regardless of the obvious placement of the PV modules that each measurement system entails – PV modules were mounted in a two axes tracker in system 1 and in a structure with a fixed orientation and tilt in system 2 – the technical differences between both measurement system are not significant. The elements and electronic devices that both of them share are far more that the ones which make them unlike, as it will be shown.

In the first sub-chapter, a simple description of the technique used to achieve the *I-V* curve measurement will be presented. In the second section, it has been decided to carry out the description of both measurement systems together as if they were a single measurement system, while in the third section the main differences between the two systems will be pointed out. Moreover, the discussion of the uncertainty associated to each recorded measurement is presented in the fourth section.

Lastly, it is important to mention that the recorded data still needed to be wiped and filtered in order to be suitable for the study. For this reason, an overview of the pre-processing procedure adopted will be presented in the fifth section.

4.1 *I-V* curve measuring technique

Theoretically in order to achieve the measure of the *I-V* curve of a module, said module needs to be connected to a variable load. The resistance swept is necessary in order to measure all the different working points in which the module can operate. In particular, the measuring technique used in this study to record the *I-V* curve is based on the capacitor charging method, which exploits the charging transient to achieve the aforementioned swept [18]. This technique is probably the simplest method that can be used for *I-V* curve tracing purposes.

In figure (4-1) a simple schematic of the circuit used for the *I-V* curve tracing is provided.

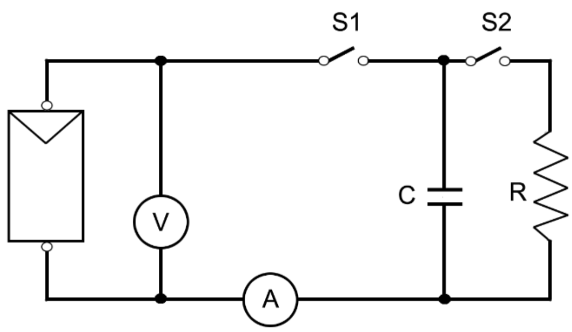

Figure 4-1: Scheme of the measuring circuit used for the *I-V* curve tracing

The circuit consist of a capacitive load (C) connected to the terminals of the PV module through a breaker (S1). A secondary discharge circuit is added in parallel, which consist of a discharge resistance (R) and a second breaker (S2). Lastly, a voltmeter and an ammeter are used to measure the voltage and the current, respectively, during the charging process.

Considering an initial condition in which the capacitor is completely discharged, when the breaker S1 is closed, there is at first a short circuit configuration - which means that the current passing in the circuit is the highest possible whilst the voltage drop is null. As the capacitor is charged, it is possible to observe an evolution from short circuit to open circuit. The current is slowly reduced while the voltage increases until the capacitor is completely charged, and open circuit configuration is achieved.

The voltage transient measured at the capacitor terminals can be defined with a simple differential equation. Its formulation is the following:

$$i(t) = C\frac{dv(t)}{dt} \tag{4-1}$$

Where:

- C (F), is the capacitance.
- $v(t)$ (V), is the instantaneous value of the voltage measured across the capacitor

The time evolution of the two quantities can be observed in figure (4-2).

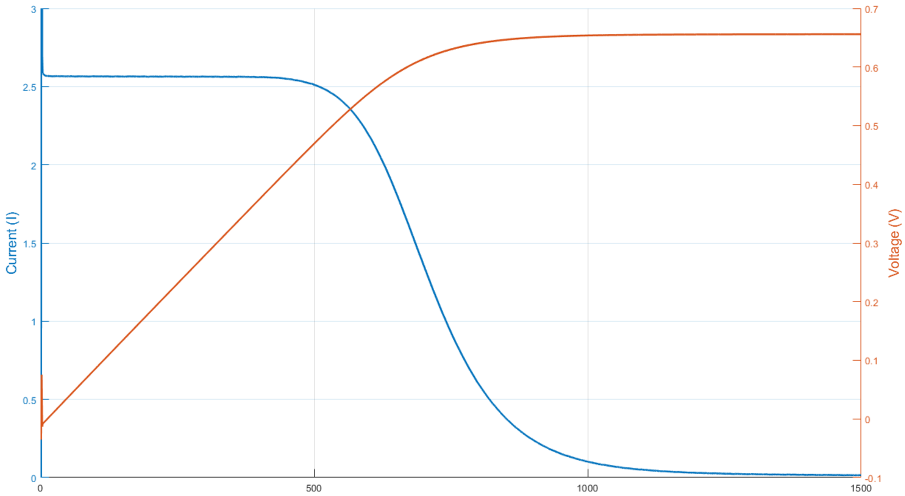

Figure 4-2: Charging transient of a capacitor connected to a PV module

As shown in figure (4-2), evolutions of voltage and current follow an asymptotic tendency. Thus, in theory the capacitor will never reach the open circuit voltage. For this reason, usually the transient is considered completed when voltage reaches 99.33% of the open circuit voltage.

Moreover, if a full charge transient from short circuit to open circuit is considered, it is possible to estimate the charging time with the following equation:

$$t_C = \frac{C}{A} \cdot \frac{V_{oc} \cdot N_S}{I_{sc} \cdot N_P} \tag{4-2}$$

Where:

- $A = 0.55\ (-)$, is the proportionality factor.
- $C\ (F)$, is the capacitance.
- V_{oc} (V), is the open circuit voltage.
- $I_{sc} (A)$, is the short circuit current.
- $N_S\ (-)$, is the number or series connected cells.
- $N_P\ (-)$, is the number of parallel connected cells.

An exact estimation of the charging time is paramount to correctly set the measuring system. For this reason, this parameter needs to be estimated before the acquisition of the *I-V* curve. The estimation can be achieved exploiting the relationship between the charging time and atmospheric conditions (irradiance and temperature) due to the fact that they have a great influence on the values of short circuit current and open circuit voltage.

4.2 Measurement system

The measurement system used for the data acquisition was designed by the IDEA Research Group focused on solar energy. It was placed in the flat roof of the Higher Technical College of the University of Jaén [19], as shown in figure (4-3)

Figure 4-3: Higher Technical College of the University of Jaén

The system was designed to measure the electrical parameters of 4 PV modules, along with the atmospheric conditions. These information are useful to analyse the electrical behaviour of the multiple modules under different outdoor conditions at the same time. The experimental setup can measure the *I-V* curves automatically and continuously, with the possibility of setting the lapse of time between each measurement (e.g. 5 min). From the measure of the *I-V* curve for each module it is possible to obtain the most important points, such as V_{oc} I_{sc} and P_{max}.

As mentioned at the beginning of the chapter, the characterization of the module can be carried out using two different measuring system, which are very similar with each other besides a few differences which will be discussed in the next section. In figure (4-4) is shown the overall system schematic valid for both measurement systems. The common characteristics between the two systems are represented in light blue whilst those peculiar to the tracker and fixed system are in blue and in orange respectively.

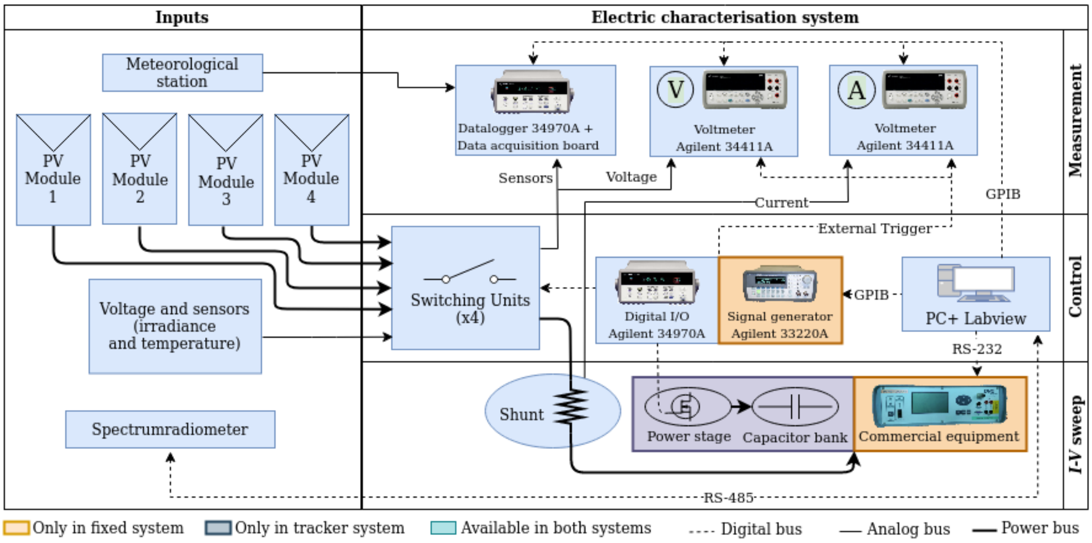

Figure 4-4: Measurement system schematic highlighting the common and different parts between tracker and fixed system.

In figure(4-4), it is possible to identify two main blocks. The first one (column inputs in figure 4-4) consists of the meteorological stations, the temperature and irradiance sensors, the spectroradiometer and the voltage measure. The second one is the electrical characterisation system. In particular, it is possible to identify the instrumentation used to record the measurements performed by the various sensors, as well as two multimeter used to record voltage and current. Moreover, since it is a single *I-V* tracer system, multiplexing is necessary in order to perform the measurement of multiple modules. This is achieved through the switching unit, which requires control and a trigger signal in order to synchronize the various measurement.

As previously mentioned, the data acquisition procedure is completely automatic and iterative. The first step of the procedure consists of the configuration of the initial conditions, which entails the manual configuration of the electrical features of the PV modules as well as the selection of the electrical parameters to measure and the time step between each measurement (e.g. 5 min). In addition, it is possible to define the daily time window in which the program must be able to work. On top of the that, the working window can be also set by defining some upper and lower limits for the irradiance value.

The second step of the iterative procedure consists of recording of the atmospheric conditions. For the acquisition of the atmospheric parameters a wide range of sensors have been installed on the system. The sensors are able to measure multiple meteorological data (such as wind speed, solar spectrum and ambient temperature). For the specific application presented in this paper, the most important data to measure were the module and ambient air temperature, the irradiance and the wind speed. In particular, the necessary sensors used to achieve those measures, among others, are the following:

1. Pt100 sensor connected in 4 wires configuration. The sensors was set on the back side of the modules to record the temperature. It is able to measure the temperature in the range between -50-150 °C.

Figure 4-5: Picture of the Pt100 Temperature probe

2. Pyranometers Kipp and Zonnen^{TM} CMP11. Two of this decives were used to measure both the horizontal global irradiance (*Gh(0)*) and the on-plane global irradiance (*Gh(a,b)*)

Figure 4-6: Picture of the pyranometer(left) placed on the tracker

3. A Young^{TM} 05305VM anemometer to record the wind speed. This measure was necessary to estimate the accuracy of the temperature measure.

Figure 4-7: Picture of the Young 05305VM anemometer

All the aforementioned measurements are recorded by a datalogger model 34970A by AGILENT® which includes two acquisition cards AGILENT® 34901A. Data is send via GPIB port to the PC. Moreover, along with the measurement of the atmospheric conditions, a first check on the reliability of the irradiance measures is performed. The irradiance is recorded before and after the *I-V* curve acquisition and the two values are compared with each other. This is done to check for possible variation of the meteorological conditions during the measure that could be caused by passing clouds. If the difference between the two is higher than 5%, the measure is classified through a checkbit as unreliable, since it could lead to some errors in the analysis. This checkbit will be referred to as 'irradiance checkbit' and it will be used in chapter 4-5 to filter the data.

The central aspect of the measuring system is related to the module selection, which is performed by the switching unit. The system needs to be able to record for each module the measure of irradiance, temperature, voltage and to close the circuit between the module and the capacitive load to record the current. This requires signals both for control and power. In particular, the aforementioned datalogger has an additional slot which is equipped with a digital multifunction Module 34907A by AGILENT® that is used to control the multiplexing system and subsequentially select each module. This port has 8 pins, four of which are going to be used to perform the module selection while the other four are used to control the capacitive load and record the *I-V* characteristic curve. This will be discussed in more details in section 4-3.

A simple schematic of the switching unit used to select the PV module under test is presented in the picture below:

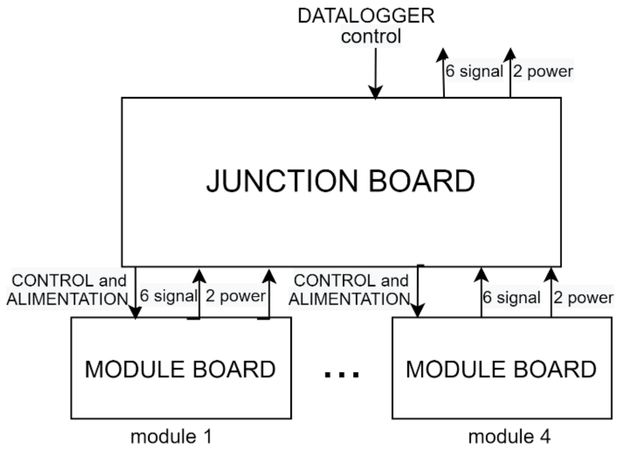

Figure 4-8: Scheme of the switching unit used to select the PV module under test

As shown in figure (4-8), each module is equipped with an electronic board where the main information of the electrical parameters and of temperature are collected. This component was designed by the IDEA research group and is placed in a waterproof box attached to the tracker. Each module board is then connected to the junction board. Its main purpose is to collect and merge the wires from each module board in a single line that is sent down to the laboratory. This electrical link is made by two power cables and 18 wires for the signal and the control.

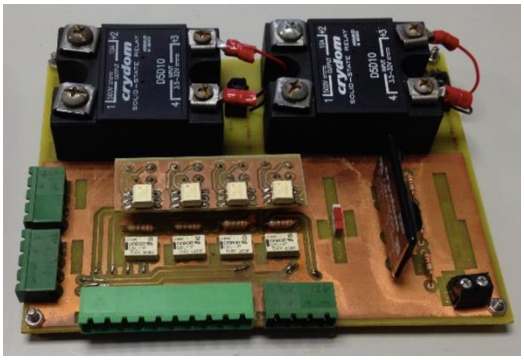

Figure 4-9: Picture of multiplexing module board equipped for each module

The multiplexing module board is shown in figure (4-9). It essentially consists of a series of relays with the corresponding control circuit. Depending on the signal send by the datalogger, the boards can connect one at the time each module to the instruments in the laboratory. Then, in the laboratory, measures of the electrical parameters and of temperature are collected by the available instrumentation shown in figure (4-4). In particular, in figure (4-9) is possible to identify many electronic components: a relay to turn on/off the board, which is commanded by 5V in order to protect the digital port of the datalogger, four MOSFET transistors for the voltage measure, four electromechanical relays connected to the Pt100 sensor and two solid state relays for the power lines that connect the PV module and the capacitive load. In addition, a small manual switch is available to turn on/off all the relays and bypass the 5 V line.

Moreover, it is possible to identify a series of jumpers (figure 4-9 in green). J1 represents the pins used to send the power supply and the control signal from the datalogger (through the junction board), while J3 and J4 gather the measurements of temperature and voltage from the sensors physically connected to the PV module. In addition, there are 8 more pins available in J2, only six of which are used to connect the board to the laboratory and gather the information about temperature and voltage. The pins are divided as follows:

1. Two wires for the voltage measure;
2. Four wires for the Pt100 sensor which uses a 4-wires resistance measures.

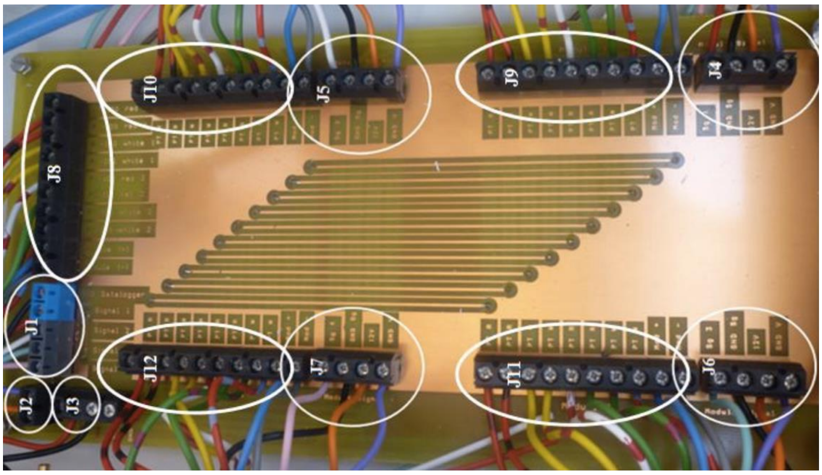

Figure 4-10: Picture of the junction board

A picture of the junction board used to collect the measure from the various module is shown in figure (4-10). Contrary to the multiplexing board it doesn't have any active components as its only purpose is to collect and merge the many wires to be send to the PC laboratory.

As shown in figure (4-4), once the module to measure is selected and the corresponding circuit is closed, two digital multimeter AGILENT® 34411A are used to measure of voltage and current. The first one takes the voltage measurement from the rooftop at the very terminals of the PV module to avoid the influence of the voltage drop due to the resistance of the wiring, while the second one is performed indirectly in the laboratory downstairs by measuring the voltage drop across a shunt resistance 10A-150mV by KAINOS®, class 0.5[1]. The synchronization of the two measures (voltage and current) to record the *I-V* curve, is achieved by means of an external trigger generated by the datalogger. The source of the trigger signal varies according to the two measuring systems, which will be discussed later.

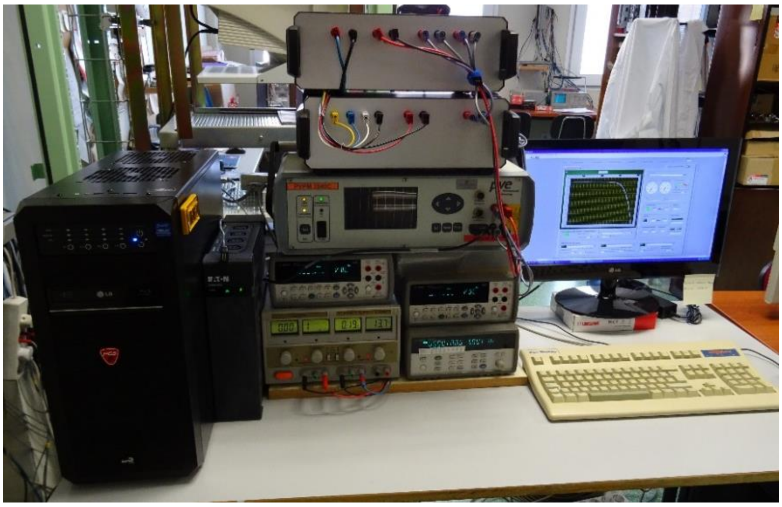

Figure 4-11: Laboratory equipment and PC with LABVIEW program

The measuring system is controlled through an application in LABVIEW®, which is able to connect the various equipment used for the measure of the *I-V* pairs and module temperature and of the atmospheric conditions, as well as any other sensor present in the system. All measurement devices are attached to the PC through a GPIB connections, except for the spectroradiometer which requires a RS485-RS232 serial connection. The laboratory equipment in shown in figure (4-11). The program saves as output the data from the described sensors and instruments in a single 'csv' file at each acquisition.

[1] Class 0.5 means 0.5% of deviation with respect to the nominal value.

4.3 Differences between Tracker and Fixed system

The main differences between the two systems are related to the way the *I-V* curves are measured and how the synchronization of the multimeter is achieved. Both systems use a capacitive load to trace the *I-V* curve, the tracker system uses a handmade device whilst the fixed system uses a commercial one. In the following sections these differences will be discussed in more details.

4.3.1 Tracker system

The tracker system, shown in figure (4-8), displays a BSQ D150/6 Solar 2-axes configuration and it is placed on the roof of the Higher Technical College of the University of Jaén as mentioned before. The system is designed to hold the PV modules always perpendicularly to the direct sun light with a misalignment of ±0.5° to avoid possible angular reflection losses.

The system description provided in chapter 4.2 can be applied to this system as it is connected to the meteorological station and the aforementioned equipment. Moreover, to achieve the measurement of all the other quantities, the overall tracker system is equipped with on plane and horizontal pyranometers, as well as a pyrheliometer and a spectroradiometer. An anemometer is used to check the wind speed in order to 'park' the tracking system in horizontal position (defence mode) whenever the wind is too high. A picture of the tracker system is shown in figure (4-12)

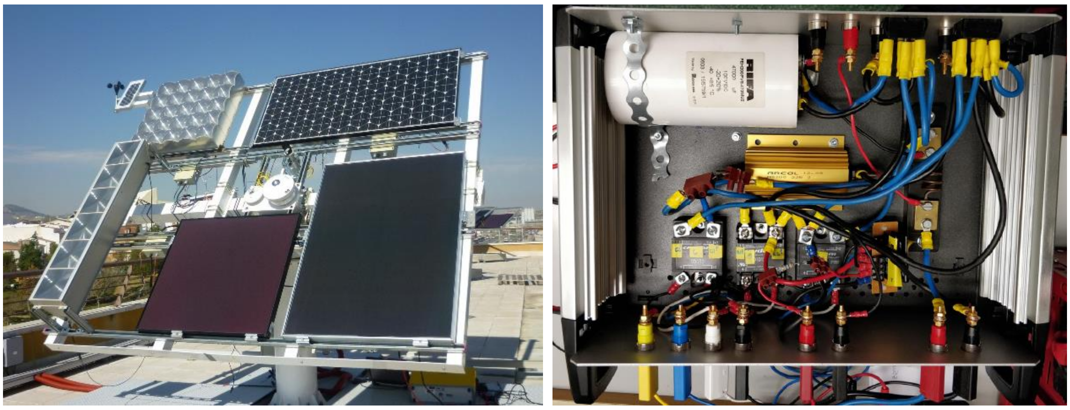

Figure 4-12: Picture of the experimental Tracker System (left) and of the capacitive load (right)

In addition, the tracker system includes a capacitive load for *I-V* tracing purposes, as shown in figure (4-12) on the right. A simple schematic of the circuit is shown in figure (4-13). The equivalent circuit is made of three sub-circuits. The first one contains the capacitor and the corresponding switch (S1) used to connect the PV module and the capacitor (C). The second one is the discharging circuit already described in section 4.1, which consists of a resistance (R) and a switch (S2). The only addition with respect to the design commented in section 4.1 in the pre-charging circuit, which consist of a voltage power supply (V) and the corresponding switch (S3), that is able to supply a negative voltage. This additional process is necessary to achieve the negative pre-charging of the capacitor, which is essential to guarantee the correct measure of the short circuit current of the PV module under test.

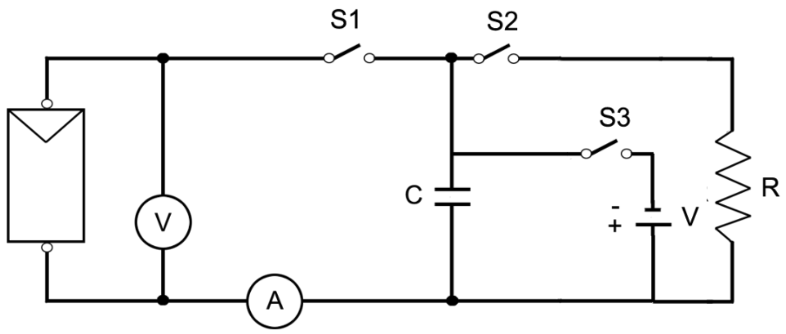

Figure 4-13: Schematic of the capacitor circuit for the measure of the *I-V* curve implemented in the tracker measuring system

As mentioned in the previous section, the Digital Multifunction Module 34907A by AGILENT® has four pins that are used to control the capacitive load circuit and to achieve the synchronization of the measures. Three pins are used to command the switches included in the capacitive load circuit: one for S1 to connect the module under test with the capacitor, one for S2 to achieve discharge and one for S3 to achieve precharge. The fourth pin is used to send the trigger for current and voltage synchronization.

4.3.2 Fixed system

The Fixed System, shown in figure 4-13, consists of a rigid structure oriented with a 0° zenith and a 35° tilt angle, on which the modules are mounted. The system description provided in chapter 4-2 can be applied to this system as all the equipment is mounted on the structure along with the module. The only difference compared to the previous system consists of the tracing device used to record the *I-V* curve. For this purpose, the system uses a commercial *I-V* curve tracker based on a PVE PVPM 2540C that is controlled by the LABVIEW program described before. Moreover, the source of the trigger to achieve synchronization of current and voltage is provided by a signal generator 33220A. The connection between the LABVIEW program and the *I-V* curve tracker is achieved directly through an RS232 link.

Figure 4-14: Picture of the experimental Fixed System

4.4 Uncertainty of the measurements

The estimation of the uncertainties related to data collected through the measurement systems is essential to guarantee the accuracy of the study. Moreover, it allows to compare the theoretical and the experimental results in order to quantify the precision associated with the models under study.

The Guide to the Expression of the Uncertainty in Measurement [20] has been used to estimate the uncertainty of each measurand. A summary of the main sources of uncertainty and the uncertainty associated with the worst scenario for the considered measurements are summarized in table 4-1. The term 'worst' indicates the scenario in which the relative tolerance ($U_{x,worst}$) is computed in the worst scenario with regard to the measurement range of the Agilent^{TM} 34970A data-logger and Agilent^{TM} 34411A digital multimeter, as well as the uncertainty associated to the specific equipment of the measurand under study.

Measurand	*Sources of uncertainty*	$U_{x,worst}$ *(%)*
Voltage (V)	Agilent™ 34411A digital multimeter	± 0.02
Current (A)	10A-150mV Kainos™ shunt resistor CL0.5 Agilent™ 34411A digital multimeter	± 1.0
Maximum Power (W)	10A-150mV Kainos™ shunt resistor CL0.5 Agilent™ 34411A digital multimeter	± 1.3
Irradiance (W/m²)	Kipp & Zonnen™ CMP 11 pyranometer Agilent™ 34970A data-logger	± 0.61
Temperature (°C)	Pt100 sensor Agilent™ 34970A data-logger	± 1.16
Wind speed (m/s)	Young™ 05305VM anemometer Agilent™ 34970A data-logger	± 0.66

Table 4-1: Measurement Uncertainty of the various measurand

4.5 Pre-processing of the data

The pre-processing step was necessary prior to starting the analysis in order to prepare properly the measured data. In particular, having to deal with a large set of available measure, to select only the measures with the best characteristics in terms of *I-V* curves and accuracy was paramount in order to guarantee as much as possible the integrity of the study.

The data pre-processing is performed automatically using the GUI previously mentioned in chapter 3. The app is able to read directly the csv files generated from the measuring system and to extract from it the information of interest after applying a series of filters:

1. *Cleaning of the I-V curves*: all the curves are filtered to remove the initial transient. This step is necessary due to the way the *I-V* curve experimental measure is performed, which presents some noise at the beginning of the transient that need to be discarded before applying the fitting procedures. In fact, only the points of the *I-V* curve of the first quadrant are considered valid. The filter looks for the 'sign change' between the two quantities to find the starting and the ending points of the *I-V* curves. In particular, the

starting point is searched for in correspondence of the last voltage sign change whilst the ending point of the curve is found in correspondence of the first current sign change at the maximum voltage value.
Once the *I-V* curve is cleaned the most important quantities are extracted from the curve: I_{sc}, V_{oc}, I_{mpp}, V_{mpp}, P_{max} and FF. In particular, depending on the kind of measure performed, the open circuit voltage is either measured or calculated by linearly fitting the last portion of the curve. On the other hand, the short circuit current is always calculated by linearly fitting the initial portion of the curve.

2. *Reduction of experimental points*: this step is necessary to solve the problem related to the non uniform distribution of the measured points in the *I-V* curve. The reduction procedure firstly searches for the maximum and mean space between two consecutive points to identify the admissible space to apply. This admissible space is set as the limit. If the gap between two consecutive points is lower than this value, the second point is deleted. On the other end, if the new gap is higher than the limit by a certain threshold, the point is re-added. This operation is performed on all the points starting from short circuit to open circuit.
As a consequence of the reduction, the computational cost of the fitting procedure is reduced as well and the whole operation is cosniderably speed up. In fact, by reducing the number of points, each iteration requires less time to be carried out.
In addition, having a more uniform distribution of points, makes it so that the fitting procedure is able to work more efficiently. In fact, while with a non-uniform distribution more weight would be given to specific portions of the curve with a higher concentration of points, with a uniform distribution the entire curve is considered without giving weight to particular portions.

3. *Mismatch detector filter and monotonicity filter*: this filter is necessary to remove those curves with multiple peaks and ripples caused by shadowing effects.
The mismatch detector filter works on the whole curve. It simultaneulsy looks for multple peaks in the P-V curve and for steps or sudden changes in the current value in the initial portion of the *I-V* curve. If either one of those searches has a positive outcome, the measures is affected by the phenomena.

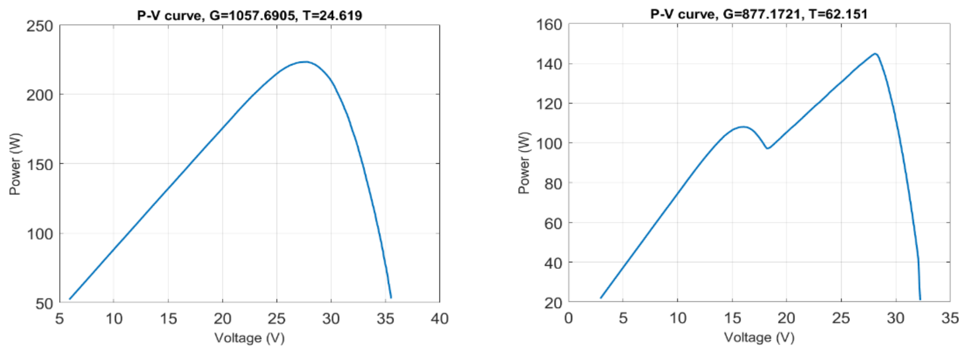

Figure 4-15: Example of a non-shaded (left) and a shaded (right) P-V curve for a monocrystalline PV module

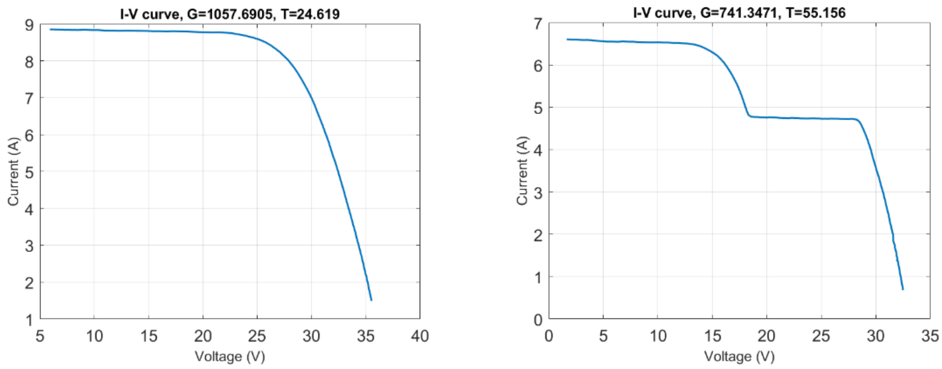

Figure 4-16: Example of a non-shaded (left) and a shaded (right) *I-V* curve for a monocrystalline PV module.

On the other hand, the monotocity filter is able to detect cripple effects on voltage and current. Depending on how far the trend is for the monotoic behaviour, the filter returns a value between 0 and 1, where 1 is strictly monotonic. The computation is performed with the MATLAB ‘monotonicity’ function.

4. *Irradiance check bit filter*: this step is performed to guarantee the accuracy of the irradiance measure. The check bit is generated automatically in the measuring procedures to identify less accurate measures. Its value is equal to 1 whenever a variation in the value of irradiance is detected between the starting and the ending of the measure. Since this variation could lead to inaccuracy of the measure, all curves with irradiance check bit equal to 1 have been discarted.

5. *Wind speed filter*: this last step is necessary to guarantee the accuracy of the temperature measure. It is reported in literature that high discrepancies between the temperature of the solar cell and that at the back of the module can be obtained under non-steady conditions. For this reason only measures recorded with wind speed lower than 5 m/s were taken into consideration for the study.

Chapter 5

Parameters Extraction

The parameters extraction procedure is the most important and crucial step of the innovative technique used to develop a suitable model that is able to describe the behaviour of PV modules with irradiance and temperature. In particular, as mentioned in chapter 3, the main difficulty is related to the implementation of the correct fitting algorithm in order to guarantee simultaneously a high accuracy of the results and a low computational cost. Furthermore, another issue is related to the selection of the correct initial conditions. This is necessary in order to guarantee the convergence of the algorithms, as some of them are very sensible to the choice of the initial conditions. For these reasons, an analytical-numerical method has been used to estimate the initial conditions. Moreover, two different methods employing different algorithms have been applied to perform the fitting procedure:

- Levenberg Marquard algorithm.
- Simulated Annealing coupled with Nelder-Mead method.

In particular, in the first sub-chapter an overview of the main optimization algorithms will be presented, providing some additional information on those used in this study. Then, in the second sub-chapter the analytical numerical method used to estimate the initial condition will be described in detail whilst in the third sub-chapter the details of the fitting procedure used in this study will be thoroughly discussed. Lastly, in the fourth sub-chapter, an overview of the post-processing procedure applied to the extracted parameter will be presented. This step is necessary to prepare the data for the application of the correlations, which will be discussed in the next chapter.

In the following sections, the parameters extraction procedure used in this study will be described. Firstly, an overview of the main optimization algorithms will be presented, providing some additional information on those used in this study. Secondly, the analytical numerical method used to estimate the initial condition will be described in detail whilst in the third sub-chapter the details of the fitting procedure used in this study will be thoroughly discussed. Lastly, an overview of the post-processing procedure applied to the extracted parameter will be presented. This step is necessary to prepare the data for the application of the correlations, which will be discussed in the next chapter.

5.1 Optimization Algorithms

Optimization algorithms are useful tools that can be used to find a good approximation of the optimal value of a specific problem whenever the function describing its behaviour is too complex to find an exact analytical solution. In particular, when dealing with global optimization problems, the goal is to discover the best solution, according to a specific criterion (objective function), when several local solutions are possible. Due to their many possible applications, optimization algorithms have been the subject of numerous studies. As a consequence, there are many optimization algorithms in literature as there is no single algorithm suitable for all problems. The right choice of an optimization algorithm can be crucially important to find the right solution for a given optimization problem. [21] [22]

Depending on the characteristics taken into consideration, optimization algorithms can be classified in many ways. A first distinction can be made between gradient-based (e.g. Gauss-Newton) and gradient-free methods (e.g. Nelder-Mead downhill simplex method), depending on whether they exploit the derivative information of the objective function in the algorithm or not. Considering a different point of view, algorithms can be divided in trajectory-based (e.g. Simulated Annealing) or population-based methods (e.g. Genetic Algorithms). The first category includes those algorithms in which there is a single solution point which will trace out a path as the iterations and optimization process continue. On the other hand, those belonging to the second category exploit multiple agents that interact with each other and trace out multiple paths simultaneously as the optimization process continues. Lastly, another subdivision can be made considering the way the algorithm evolves between two successive iterations. Focusing on this last classification in more details, it is possible to identify two categories: deterministic and stochastic methods.

Deterministic algorithms (e.g. Levenberg Marquardt algorithm or Nelder-Mead downhill simplex method) follow a precise sequence of actions without any random nature. In this sense, design variables and objective functions can have the same values and repeat the same solution route, which means that the algorithm will be able to reach the same final solution when starting with the same initial point.

Stochastic algorithms (e.g. Simulated Annealing or Genetic algorithm) on the other end, always involve randomness as they include uncertainty into the model. Therefore, each time the algorithm will reach a different point even though the starting initial point is always the same. They provide an effective framework to solve complex optimization problems, whenever the derivative information is not available. These kinds of algorithms take advantage of the fact that the probability distributions governing the data are known and can be estimated even when data cannot be known accurately.

In general, when dealing with global optimization problems, the fitting algorithm needs to be written as a minimization problem. In this sense, the objective function to minimize can be expressed as the sum of the square of the error between the estimated function and measured data in each available point. This function is expressed as follows:

$$resnorm = F(\theta) = \sum_{i=0}^{N} \left(y_{measured,i} - y_{estimated,i}(\theta)\right)^2 \tag{5-1}$$

Where:

- $y_{measured,i}$, is the measured data in point i.
- $y_{estimated,i}(\theta)$, is the fitted value estimated in point i.
- θ, is the vector containing the set of parameters on which the optimization is performed.

During the fitting procedure a new set of parameters is estimated at each iteration until the objective function is below the tolerance value requested. Once the objective function is minimized the solution is accepted.

The three algorithms used in this study will be discussed in more detail in the following sections.

5.1.1 Levenberg Marquardt Algorithm

Levenberg Marquardt algorithm is gradient-based method used for the optimization of nonlinear least squares problems. It is typically used for parameter extraction of semiconductor devices, and in this sense, it is very suitable for this specific application. The major difficulty of this algorithm resides in the strong dependence on the values of the initial parameters. A good initial estimation is paramount to guarantee its convergence and to avoid being stuck in local minimum configurations. [23] [24]

Furthermore, the LM method is a hybrid technique that interpolates between the Gauss-Newton algorithm and the Steepest Descent method to converge to an optimal solution. The combination between the two methods is controlled by the 'damping factor' λ. For large values of λ, LM behaves as steepest descent method, whereas when λ takes low values LM becomes similar to the Guess-Newton method. Low values of λ are typically achieved closed to the optimum, where the optimization procedure is less sensitive to the initial values. The switching between the two methods is done automatically inside the LM algorithm.

At each iteration, the set of parameters undergoes a certain perturbation which can be written with the following expression:

$$h_{LM} = [(J(\theta)^T J(\theta) + \lambda \cdot I)^{-1} J^T(\theta)(\, y_{meas} - y_{est}(\theta))]_{\,\theta=\theta_i} \qquad (5\text{-}2)$$

Where:

- θ, is the vector containing the set of parameters on which the optimization is performed.
- $J(\theta)$, is the Jacobian matrix of the partial derivative of the fitting function with respect to the parameters θ for reach value of measured voltage.
- λ , is the damping factor.
- I, is the identity matrix.

Depending on the values of the damping factor, the methods will behave differently at each iteration.

- For high values of λ, the algorithm behaves like the Steepest Descent method. Considering α ast the size of the movement in the 'downhill direction' it is possible to write:

$$h_{SD} = \alpha\, J^T(\theta)(y_{meas} - y_{est}(\theta) \qquad (5\text{-}3)$$

- For small values of λ, the algorithm behaves like the Gauss-Newton method. Considering equation (3-2) it can be written:

$$h_{GN} = [\left(J(\theta)^T J(\theta)\right)^{-1} J^T(\theta)(\, y_{meas} - y_{est}(\theta))]_{\,\theta=\theta_i} \qquad (5\text{-}4)$$

5.1.2 Simulated Annealing

Simulated Annealing is one of the simplest meta-heuristic methods known. It is typically used to address global optimization problems in which the objective function is not explicitly given and needs to be evaluated through a simulation. For this reason, is very used to approach real life problems such as that of parameters extraction in PV applications, because it can be used to avoid being trapped in a local minima. To do so, it is necessary to define a process that is able to accept transitions to states that momentarily reduce the performance of the current solutions. [25] [26] [27]

The Metropolis algorithm is the basic component of the SA method. The algorithm is based on Monte Carlo techniques which consist in generating a sequence of states following specific probabilistic criterions. In particular, the algorithm exploits the analogy between the optimization problems and the physical process of annealing of materials, in which the heating and cooling of materials is controlled in order to guarantee the crystallization and the reduction of defects, thus lowering the free energy of the material.

In order to apply this analogy to the optimization problems, the following equivalences are made:

- The possible solutions (θ) represent the possible states of the solid;
- The objective function($F(\theta)$) represent the energy of the solid that needs to be minimized.

In addition, a control parameter ‘c’ is introduced, which works as a temperature.

Consequently, in order to reproduce faithfully the evolution of the physical structure of material undergoing annealing, for each point of the state space, information is provided about the neighbourhood and the mechanism for generating a solution in this neighbourhood.

The first step of the procedure consists in the initialization of the state space (θ_0, initial condition) to provide a starting point for the searching method. At each iteration, the algorithm will evolve from state space θ_i to state space θ_j. This evolution is called transition and it represents the replacement of the current solution with a neighbouring solution. This operation is typically carried out in two stages: generation and acceptance. Thus, it is possible to define an acceptance principle for the new solution, which is given by the following probability:

$$p\left(accept\ \theta_j\right) = \begin{cases} 1 & if\ F\left(\theta_j\right) < F(\theta_i) \\ e^{\frac{F(\theta_i) - F\left(\theta_j\right)}{c}} & otherwise \end{cases} \qquad (5\text{-}5)$$

Where:

- $F(\theta_i)$ is the objective function estimated in state point i.
- $F\left(\theta_j\right)$ is the objective function estimated in the neighbouring state point j.
- c is the control temperature parameter. At first it has a high value and its decreased during the procedure to simulate the cooling process.

One peculiar feature of simulated annealing is the ability to accept a transition that degrades the objective function. If fact, as shown in equation (4-26), if the objective function is reduced in the transition, the new solution is always accepted, whereas if the objective function undergoes degradation, the new solution has a certain probability to be accepted. At the beginning of the process the control parameter which simulates the temperature is high, thus increasing the probability to accept transitions with high objective degradation and thereby explore the state space thoroughly. On the contrary, as the control parameter decreases, only the transitions improving the objective function or those with low deterioration can be accepted. For this reason, simulated annealing is a useful tool that can be used to avoid being stuck in local minimum configurations whenever dealing with global optimization problems.

5.1.3 Nelder-Mead Algorithm

The Nelder-Mead algorithm, also known as simplex search algorithm, is a direct search method used for multidimensional unconstrained optimization problems. The basic algorithm is very simple and for this reason is very popular in many fields of science and technology. This method does not require information about the derivative, therefore is very suitable for problems with complex non-smooth functions. In fact, it can also be used for problems with discontinuous function whose values are subjected to uncertainty and noise. [28]

As previously mentioned, the Nelder-Mead algorithm is simplex based. Therefore, in order to understand how the method works, it is important to clarify what a simplex is. A simplex S in R^n is defined as the convex hull of n+1 vertices ($\theta_0, \dots, \theta_n \in R^n$). For example, a simplex in R^2 is a triangle (3 vertices) whilst a simplex in $R^3$is a tetrahedron (4 vertices).

In particular, in simplex-based direct search method, each vertices of the simplex correspond to a set of independent variables (θ) for which is possible to evaluate directly the objective function (F(θ)). The method begins with n+1 points ($\theta_0, \dots, \theta_n \in R^n$) that are considered the vertices of the working simplex. At each iteration a new point of the simplex is generated to replace the point for which the objective function assumes the worst value among all the others. The algorithm allows for termination whenever the objective function is sufficiently small compared to the imposed tolerance or if the user-specified number of iterations has been exceeded.

In particular, at each iteration, the new point of the simplex is generated according to following modifications. Starting from a sorting procedure, the worst point (x_W) is identified. Then, the modification steps are the following:

1. *Reflection*: the new point (x_R) is generated by reflecting the worst point of the simpelx with respect to the centre of the simplex. If the new point has an intermediate value of objective function compared to the other points in the simplex, it is accepted in place of the worst point. Otherwise, if the new point has an objective function lower that the best point, a new modification is performed (expansion). At the same time, if the reflected point has an higher objective function compared to the worst point, it means that the modification was unsuccesfull and a different type of modification is perfomerd (inside or outside contraction).

2. *Expansion*: the new point (x_E) is generated in the same direction as before with a higher distance from the centre of the simplex. If the objective function is lower than that of the reflected point, this point will replace the worst point. Otherwise the worst point is replaced by the reflected point.
3. *Outside Contraction*: the new point (x_{OC}) is generated by contracting toward the outer direction the worst point. If the objective function is lower the new point is accepted, otherwise a new contraction is performed.
4. *Inside Contraction*: the new point (x_{IC}) is generated by contracting toward the inner direction of the worst point. If the objective function is lower, the new point replace the worst point.
5. *Shrink*: when no one of the previous procedure has caused an improvement, the whole simplex is replaced through a shrinking process.

One of the main issues of the Nelder-Mead algorithms is that it is not guaranteed to converge. For this reason, it is better when coupled with other algorithms to find an initial good approximation in which to start the search away from local minimums.

5.2 Estimation of the Initial Conditions

Before applying the optimization algorithm, an initial set of parameters needs to be estimated. This set of parameters works as a starting point for the search of the optimal configuration. For this reason, it is better for it to not be too far off from the final result. Furthermore, it is imperative that the initial values still carry some sort of physical meaning, otherwise the fitting procedure could easily lead to incorrect results or require a higher computational effort to find the correct results.

In literature there are many analytical correlations and methods that can be used to perform a rough estimation of the parameters of the single diode model. In particular, in this study, a combination of analytical and numerical method has been implemented to guarantee a good first estimation of the initial parameters and simplify the accurate extraction of the five parameters with the optimization algorithms.

In reality, the initial value of the diode ideality factor is assumed constant and equal to 1.5, while the other four parameters are extracted with the procedure mentioned above. It requires only the coordinates of three key points of the *I-V* curves: the open circuit voltage (V_{oc}), the short circuit current (I_{sc}) and the voltage and current at maximum power point (V_{mpp}, I_{mpp}). From these points, it is possible to determine all parameters according to the series resistance (R_s). The series resistance is thus determined using a rapid and iterative algorithm that solves a nonlinear equation. Once its value is extracted, the other parameters are calculated accordingly, avoiding having to deal with too many mathematical approximations.

Considering the transcendental equation of the equivalent circuit (1-23), three equations can be derived for the three key points of the *I-V* curve:

- The open circuit point (V_{oc},0):

$$0 = I_{ph} - I_0\left(e^{\frac{V_{oc}}{V_{th}\cdot N_S\cdot n}} - 1\right) - \frac{V_{oc}}{R_{sh}} \tag{5-6}$$

- The short circuit point (0,I_{sc}):

$$I_{sc} = I_{ph} - I_0\left(e^{\frac{R_S\cdot I_{SC}}{V_{th}\cdot N_S\cdot n}} - 1\right) - \frac{R_s \cdot I_{sc}}{R_{sh}} \tag{5-7}$$

- The maximum power point (V_{mpp}, I_{mpp}):

$$I_{mpp} = I_{ph} - I_0\left(e^{\frac{V_{mpp}-R_S\cdot I_{mpp}}{V_{th}\cdot N_S\cdot n}} - 1\right) - \frac{V_{mpp} + R_s \cdot I_{mpp}}{R_{sh}} \tag{5-8}$$

From (5-6) is possible to obtain an explicit formulation for the photogenerated current, which can be substituted in equations (5-7) and (5-8).

$$I_{ph} = I_0\left(e^{\frac{V_{oc}}{V_{th}\cdot N_S\cdot n}} - 1\right) + \frac{V_{oc}}{R_{sh}} \tag{5-9}$$

$$I_{sc} = I_0\left(e^{\frac{V_{oc}}{V_{th}\cdot N_S\cdot n}} - e^{\frac{R_S\cdot I_{SC}}{V_{th}\cdot N_S\cdot n}}\right) + \frac{V_{oc} - R_s \cdot I_{sc}}{R_{sh}} \tag{5-10}$$

$$I_{mpp} = I_0\left(e^{\frac{V_{oc}}{V_{th}\cdot N_S\cdot n}} - e^{\frac{V_{mpp}-R_S\cdot I_{mpp}}{V_{th}\cdot N_S\cdot n}}\right) + \frac{[\![V_{oc}-(V]\!]_{mpp}+R_S\cdot I_{mpp})}{R_{sh}} \tag{5-11}$$

To clarify the equations and simplify the discussion, it is possible to define some variables:

$$X_{oc} = e^{\frac{V_{oc}}{V_{th}\cdot N_S\cdot\cdot n}} \tag{5-12}$$

$$X_{sc} = e^{\frac{R_S\cdot I_{SC}}{V_{th}\cdot N_S\cdot\cdot n}} \tag{5-13}$$

$$X_{mpp} = e^{\frac{V_{mpp}+R_s \cdot I_{mpp}}{V_{th} \cdot N_S \cdot \cdot n}} \tag{5-14}$$

While X_{oc} can be estimated at STC using the information provided by the manufacturer in the datasheet, X_{sc} and X_{mpp} can be estimated only if Rs is determined. Nonetheless, these variables can be used to rewrite equations (5-10) and (5-11) as follows:

$$I_{sc} \cdot \left(1 + \frac{R_s}{R_{sh}}\right) = I_0(X_{oc} - X_{sc}) + \frac{V_{oc}}{R_{sh}} \tag{5-15}$$

$$I_{mpp} \cdot \left(1 + \frac{R_s}{R_{sh}}\right) = I_0\left(X_{oc} - X_{mpp}\right) + \frac{V_{oc} - V_{mpp}}{R_{sh}} \tag{5-16}$$

Looking at typical values found in literature, R_s is usually in the order of a few tenths of Ohms whilst R_{sh} is in the order of a few hundred. Considering these as typical values $R\_sh \gg R\_s$, so it is possible to introduce a simplifying assumption:

$$1 + \frac{R_s}{R_{sh}} \cong 1 \tag{5-17}$$

Introducing this assumption in equation (5-15) and (5-16), it can be obtained:

$$I_{sc} = I_0(X_{oc} - X_{sc}) + \frac{V_{oc}}{R_{sh}} \tag{5-18}$$

$$I_{mpp} = I_0\left(X_{oc} - X_{mpp}\right) + \frac{V_{oc} - V_{mpp}}{R_{sh}} \tag{5-19}$$

Lastly, from these equations it is possible to obtain a formulation for the saturation current and the shunt resistance.

$$I_0 = \frac{V_{oc} \cdot \left(I_{sc} - I_{mpp}\right) - V_{mpp} \cdot I_{sc}}{V_{oc} \cdot \left(X_{mpp} - X_{sc}\right) - V_{mpp} \cdot (X_{oc} - X_{sc})} \tag{5-20}$$

$$R_{sh}^{-1} = \frac{I_{sc} \cdot \left(X_{mpp} - X_{oc}\right) + I_{mpp} \cdot (X_{oc} - X_{sc})}{V_{oc} \cdot \left(X_{mpp} - X_{sc}\right) - V_{mpp} \cdot (X_{oc} - X_{sc})} \tag{5-21}$$

It can be observed that in these equations the only unknowns are X_{mpp} and X_s, which depends on the series resistance. In fact, the short circuit current and the open circuit voltage, as well as the maximum power point voltage and current, are all estimated in the pre-processing step of the procedure.

Therefore, the photogenerated current (5-9), the saturation current (5-20) and the shunt resistance (5-21) are all dependent only on the series resistance. Moreover, to fully solve the problem an additional equation is needed. This equation can easily be derived exploiting the maximum power point definition.

$$\left.\frac{dP}{dV}\right|_{(V_{mpp},I_{mpp})} = V_{mpp} \cdot \left(\frac{dI}{dV}\right) + I_{mpp} = 0 \tag{5-22}$$

$$\left.\frac{dI}{dV}\right|_{(V_{mpp},I_{mpp})} = -\frac{I_{mpp}}{V_{mpp}} \tag{5-23}$$

The derivative of the current with respect to the voltage is evaluated considering the first derivative of the transcendental equation (1.23).

$$\frac{I_{mpp}}{V_{mpp}} = \frac{I_0}{V_{mpp} N_S n}\left(1 - \frac{R_S I_{mpp}}{V_{mpp}}\right) e^{\frac{V_{mpp}+R_S I_{mpp}}{V_{th} \cdot N_S \cdot n}} + \frac{1}{R_{sh}}\left(1 - \frac{R_S I_{mpp}}{V_{mpp}}\right) \tag{5-24}$$

$$\frac{I_{mpp}}{V_{mpp}} = \left(1 - \frac{R_s \cdot I_{mpp}}{V_{mpp}}\right)\left(\frac{I_0 \cdot X_{mpp}}{V_{th} \cdot N_S \cdot n} + \frac{1}{R_{sh}}\right) \tag{5-25}$$

Finally, after some manipulations, it is possible to obtain the following relationship that allows to compute the value of the series resistance $R_{s,cal}$.

$$R_{s,cal} = \frac{V_{mpp}}{I_{mpp}} - \frac{1}{\left[\frac{I_0 \cdot X_{mpp}}{V_{th} \cdot N_S \cdot n} + \frac{1}{R_{sh}}\right]} \tag{5-26}$$

This equation is strongly nonlinear, and it can be solved numerically to find the value of R_s only through a simple and accurate iterative algorithm. A simple schematic of the iterative procedure used is shown in the figure below.

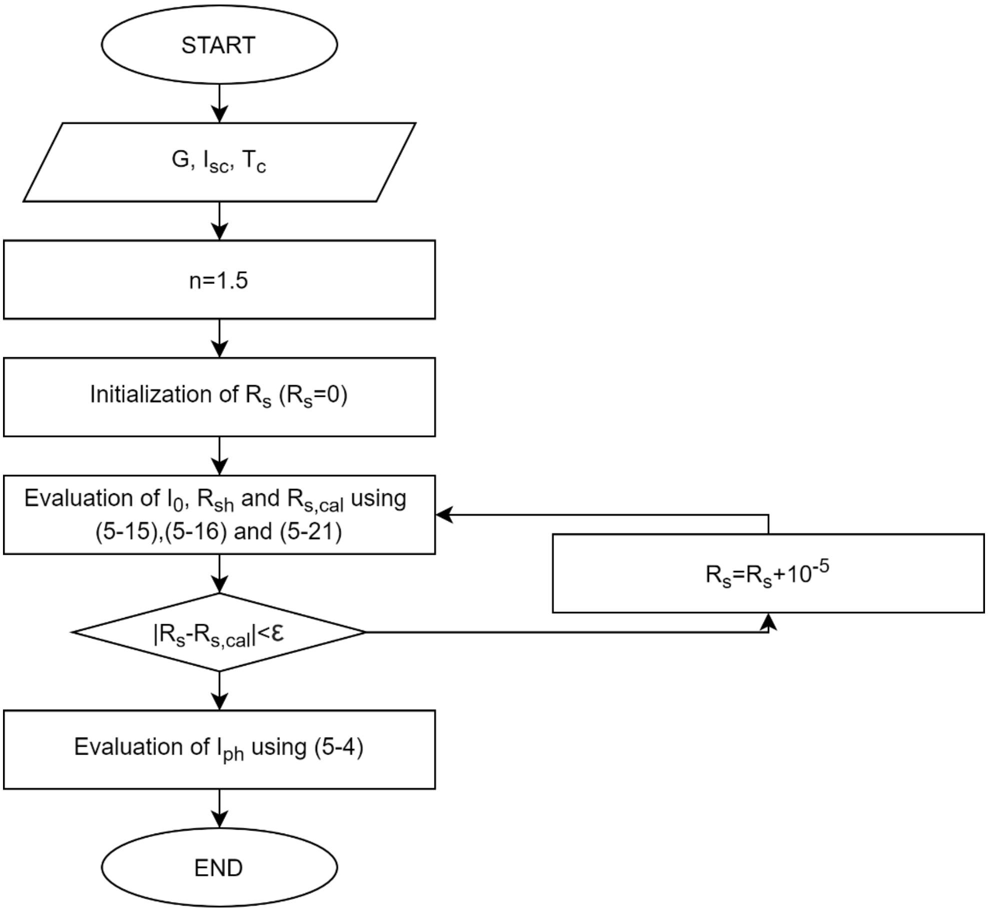

Figure 5-1, Flowchart of the iterative procedure used to estimate the initial conditions

As shown in figure (5.1), the series resistance is initialized considering Rs=0 and is gradually increased by a factor 10^{-5} at each iteration. For each value, I_0 and R_{sh} are evaluated using equations (5.20) and (5.21), as well the calculated series resistance $R_{s,cal}$ which is compared with R_s to check the validity of the parameters found. The algorithm converges whenever the difference between R_s and $R_{s,cal}$ is below a certain threshold.

5.3 Applied Fitting Procedure

As previously stated, many different approaches can be found in literature to address the problem of parameters extraction of solar cells. In particular, regarding this study, two different methods have been implemented, with the idea to compare them in terms of accuracy and computational effort:

1. The first method uses the Levenberg Marquardt algorithm.
2. In the second method Simulated Annealing and Nelder-Mead algorithm were coupled together to accurately extract the parameters of the equivalent circuit model.

In the first method, the explicit form of the transcendental equation with Lambert W-function (eq. 1-24) was used as the fitting function to estimate the *I-V* curve as a function of the five parameters, whereas in the second method the implicit formulation (eq. 1-23) was preferred to speed up the fitting procedure. Nonetheless, in order to fit the experimental *I-V* characteristic curve, the extraction problem needs to be written as a minimization problem. In this sense, the definition presented in chapter 3 can be used (Eq. 5-1). Therefore, in both methods the objective function can be expressed as follows, considering θ as the vector containing the five parameters.

$$F(\theta) = \sum_{i=1}^{N_{points}} \left(I_{measured} - I_{estimated}(V_{measured}, \theta)\right)^2 \tag{5-27}$$

In both methods, the initial condition θ_0 has been estimated using the procedure explained in the previous chapter. This step was paramount especially for the application of the Levenberg Marquardt algorithm since it is very sensible to the choice of the initial conditions. Furthermore, the main differences between the two methods have been summarized in the table below:

	Algorithm	*Minimum Iterations*	*Tolerance*
1st method	Levenberg Marquardt	1000	10^{-30}
2nd method	Simulated Annealing	4000	10^{-30}
	Nelder Mead	8000	

Table 5-1: Table of the most important parameters of the two fitting methods.

Whereas the same tolerance has been requested in both methods, the overall minimum number of iterations is remarkably higher in the second one. This has been done to guarantee a good level of accuracy whilst taking into consideration the computational cost of the three algorithms. As a matter of fact, even though the first method is able to reach convergence in a shorter number of iterations, the time required for each iteration is considerably higher with the Levenberg-Marquardt algorithm compared to the other two algorithms. In this sense, a comparison between the computational effort and the accuracy of the two methods, regarding this specific application, will be carried out in details in later chapters.

5.4 Post-Processing and Validation of the Results

The post-processing step is essential to guarantee the accuracy of the results and the proper operation of the overall energy estimation procedure. In this sense, the results obtained from the fitting (θ_{opt}) were filtered in three ways, taking into consideration the normalized root mean square error, the error on the estimation of the maximum power and the physical meaning of the extracted parameters.

This last step is necessary to overcome the overfitting problem mentioned before, which is intrinsic with the use of optimization algorithms. In this regard, the results were manually filtered to remove the un-physical data (e.g. values of the series resistance around 20 ohm) which were easily identified with respect to the overall observable trend. Additional filters on the temperature values have been applied to address possible error in the temperature measure with the PT100 sensor.

Moreover, focusing on the first two filters mentioned, a precise definition can be given to estimate their values as for filtering purposes a limit has been imposed on the two quantities.

The *normalized root mean square error (NRMSE)*, is a measure of the error between the experimental current and the estimated current with the optimized parameters. In this sense, it can be considered as a measure of the 'goodness' of the optimization algorithm as it gives information about how well the algorithm was able to work to extract the optimal value of the parameters. The lower this value, the better the estimated *I-V* curve approximate the experimental curve.

It is given by the following formula:

$$NRMSE = \frac{\sqrt{\frac{\sum_{i=1}^{N_{points}}\left(I_{measured}-I_{estimated}\left(V_{measured},\theta_{opt}\right)\right)^2}{N_{points}}}}{\frac{\sum_{i=1}^{N_{points}} I_{measured}}{N_{points}}} \cdot 100 \tag{5-28}$$

Where:

- $V_{measured}$, is the experimental voltage value. (V)
- $I_{measured}$, is the experimental current value. (A)
- $I_{estimated}(\theta_{opt})$, is the estimated current evaluated with the explicit formulation (Eq 1.24). (A)
- N_{points}, is the number of points in the experimental *I-V* curve.

The *error on the estimation of the maximum power (Err_{Pmax})*, is the percentage error on the maximum power (%). Once again, it gives an information about the 'goodness' of the result, focusing on a specific point of the *I-V* curve which is that of maximum interest for the purpose of this study. In fact, a correct estimation of the maximum power point with respect to the experimental value is paramount to guarantee the accuracy of the energy estimation procedure.

It is given by the following formula.

$$Err_{Pmax} = \frac{P_{\max_{\text{measured}}} - P_{\max_{estimated}}(\theta_{opt})}{P_{\max_{\text{measured}}}} \cdot 100 \tag{5-29}$$

Where:

- $P_{\max_{\text{measured}}}$, is the experimental maximum power. (W)
- $P_{\max_{estimated}}(\theta_{opt})$, is the estimated power. (W)

The details on how the filters were applied to each module analysed in the study will be presented in later chapters. The results of each module differ slightly depending on the typology of the module under test and on the specific details of the measuring campaign that was carried out.

Chapter 6

Parameters Correlations

As stated at the beginning of chapter 3, the goal of this study is to obtain some correlations that can predict the behaviour of the various electrical parameters with respect to the environmental conditions, such as module irradiance and temperature. This is achieved by applying a non-linear fitting procedure to the equations presented in the following sub-chapters. [17]

For simplicity, the nomenclature of the atmospheric parameters used in all the correlations is presented here to avoid repetition. This includes irradiance and temperature both in standard test condition and the measured values.

- $G_{STC}\ \left(\frac{W}{m^2}\right)$, is the irradiance in standard test conditions ($1000\,\frac{W}{m^2}$).
- $T_{c,STC}\ (°C)$, is the temperature in standard test conditions (25 °C).
- $G\ \left(\frac{W}{m^2}\right)$, is the irradiance.
- $T_c\ (°C)$, is the temperature.

Furthermore, it is important to note that the regression is applied separately to the parameters extracted with the two methods previously mentioned, LM (Levenberg Marquardt) and SA-NM (Simulated Annealing and Nelder-Mead) respectively. Therefore, in the end, two different sets of correlations will be obtained.

6.1 Photogenerated Current

The photogenerated current is proportional with the irradiance and linear with Temperature through the alpha coefficient, which is usually given by manufacturer. In particular, its equation can be expressed with the following formula

$$I_{ph} = I_{ph,STC} \cdot [1 + \alpha(T_c - T_{c,STC})] \cdot \frac{G}{G_{STC}} \tag{6-1}$$

Where:

- $\alpha\ \left(\frac{1}{K}\right)$, is the temperature coefficient provided by the manufacturer datasheet (b).
- $I_{ph,STC}\ (A)$ is the photogenerated current in standard test conditions. Its value is unkown and it is the coefficient that needs to be estimated to optimized with the nonlinear regression (a).

6.2 Saturation Current

The saturation current has a cubic correlation proportional with the temperature. In this regard, the following equation can be written for the monocrystalline technology:

$$I_0 = I_{0,STC} \cdot \left(\frac{T_c}{T_{c,STC}}\right)^3 \cdot e^{\left(\frac{E_{g,STC}}{T_{STC}} - \frac{E_g(T_c)}{T_c}\right) \cdot \frac{1}{k_b}} \tag{6-2}$$

$$E_g(T_c) = E_{g,STC} \cdot \left[1 - 0.0002677 \cdot \left(T_c - T_{c,STC}\right)\right] \tag{6-3}$$

$$E_{g,STC} = 1.121\ \cdot q_e \qquad {\scriptstyle for\ mi-Si} \tag{6-4}$$

Where:

- $k_b\ \left(\frac{J}{K}\right)$, is the Boltzmann constant ($1.381\ 10^{-23}\ \frac{J}{K}$).
- $E_g(T_c)\ (J)$, is the energy gap at T_c condition. It is defined by equation (5.27).
- $E_{g,STC}\ (J)$, is the energy gap in standard test conditions. For monocrystalline technology is defined as equation (5.28).
- $q_e\ (C)$, is the charge of the electron ($1.602\ 10^{-19} C$).
- $I_{0,STC}$ (A), is the saturation current in standard test condition. Its value is unkown and it is one of the coefficients that needs to be estimated to optimized with the nonlinear regression (a).

Furthermore, since the equation above mentioned is valid and can be used only for technology whose band gap is well known as those employing monocrystalline silicon, some modifications are required. In this sense, a new adimensional empirical coefficient χ is added to take into consideration the different behaviours of the various technologies in terms of energy gap. With this coefficient the equation can be used for all technologies.

$$I_0 = I_{0,STC} \cdot \left(\frac{T_c}{T_{c,STC}}\right)^3 \cdot e^{\chi \cdot \left(\frac{E_{g,STC}}{T_{STC}} - \frac{E_g(T_c)}{T_c}\right) \cdot \frac{1}{k_b}} \tag{6-5}$$

Where:

- $\chi\ (-)$, is the empirical coefficient used to simulated the different behaviour of the various technologies (b). It can be fitted when dealing with non-standard tecnhologies or fixed to a constant value. In particular, in the case of monocrystalline tecnologies its value is fixed to 1.

6.3 Diode ideality factor

The diode ideality factor is often considered as constant in most applications. In reality, it has a slightly linear trend both with irradiance and temperature which can be expressed by the following formula:

$$n = a + b \cdot G + c \cdot T_c \tag{6-6}$$

Where:

- $a\ (-)$, is the intercept term.
- $b\ \left(\frac{m^2}{W}\right)$, is the irradiance coefficient, which expresses the linear dependence of the diode ideality factor with irradiance.
- $c\ \left(\frac{1}{°C}\right)$, is the temperature coefficient, which expresses the linear dependence of the diode ideality factor with temperature.

All three coefficient are unknown and are optimized in the nonlinear regression procedure.

6.4 Series Resistance

The series resistance is proportional with the temperature and logarithmical with irradiance. The following equation can be written:

$$R_s = R_{s,STC} \cdot \frac{T_c}{T_{c,STC}} \cdot \left[1 - \lambda_{R_s} \cdot log\left(\frac{G}{G_{STC}}\right)\right] \tag{6-7}$$

Where:

- $R_{s,STC}$ (Ω), is the series resistance in standard test conditions. Its value is unkown and it is the first coefficients that needs to be optimized with the nonlinear regression (a).
- λ_{R_s} ($-$), is an adimensional empirical coefficient proportional to the logarithmic variation of irradiance. Its value is unkown and it is the second coefficient that needs to be otpmized with the nonlinear regression (b).

Equation (6-7) is correct when dealing with monocrystalline technologies. Furthermore, it has been observed that in some cases, when dealing with non-standard technologies, the actual behaviour of the series resistance differs from the expected behaviour and thus equation (6-7) cannot correctly fit the experimental points. In those cases, due to the high dispersion of the extracted parameters, the series resistance was considered constant with both temperature and irradiance.

6.5 Shunt Resistance

The shunt resistance presents no influence with respect to temperature and is only inversely proportional with irradiance instead. Its expression can be written as follows:

$$R_{sh} = R_{sh,STC} \cdot \frac{G_{STC}}{G} \tag{6-8}$$

Where:

- $R_{sh,STC}$(Ω), is the shunt resistance in standard test condition. It is the coefficient that needs to be optimized with the nonlinear regression procedure (a).

In many applications found in literature, the four parameters model is preferred to the five parameters one due to the negligible contribution of the shunt resistance to the I-V curve formulation. For this same reason, the extracted values of the shunt resistance in some cases were very disperse and not following the expected behaviour. Therefore, even if the five parameters model was still preferred to guarantee a higher accuracy, the value of the shunt resistance has been considered constant both in terms of temperature and irradiance whenever its tendency with the two measure was unclear.

6.6 Validation and Accuracy of the correlations

The procedure is carried out separately for each of the 5 parameters. Coefficients $I_{ph,STC}$, $I_{0,STC}$, χ, a, b, c, $R_{s,STC}$ and λ_{R_s} are optimized at each iteration until the optimal configuration is achieved. In the end, an optimal surface will be obtained for each of the five parameters as a function of both irradiance and temperature.

Furthermore, to check the '*quality*' of the estimated correlations, the *normalized root mean square error (NRMSE)* is used again to compute the errors between the experimental and the fitted surfaces of each parameter. Its implementation is performed with the following formula, where θ represent the parameter under analysis ($I_{ph}, I_0, n, R_s \ or \ R_{sh}$):

$$NRMSE_\theta = \frac{\sqrt{\frac{\sum_{i=1}^{N_{points}}\left(\theta_{correlation} - \theta_{experimental}\right)^2}{N_{points}}}}{\frac{\sum_{i=1}^{N_{points}} \theta_{experimental}}{N_{points}}} \cdot 100 \qquad (6\text{-}9)$$

Where:

- $\theta_{correlation}$, is the parameter estimated from correlation.
- $\theta_{experimental}$, is the experimental value of the parameter.
- N_{points}, is the number of experimental point.

The goal is to have the value of NRMSE as low as possible to guarantee a good estimation of each parameters. To have good correlations is essential to achieve a good approximation of the estimated energy, as it will be shown in the following chapter.

Chapter 7

Power and Energy estimation

The last step of this study consists in the energy estimation, which is achieved through the integration in time of the power at maximum power point. Since the goal of this study is to compare different methods to estimate the energy, the power is estimated according to two different approaches:

- Through the use of correlations, in order to compute the measured *I-V* curve with respect to the estimated parameters.
- Through the Osterwald method.

In this sense, the energy estimation has been done considering four values: the experimental measured value, the one estimated with the Osterwald method and those estimated with the parameters correlations mentioned in the previous chapters, LM (Levenberg Marquardt) and SA-NM (Simulated Annealing and Nelder-Mead), respectively. Lastly, a comparison between the experimental values and the estimated ones has been performed to analyse the accuracy of the different methods employed.

As mentioned in chapter 3, the energy estimation process can be divided in four simple steps which will be discussed in detail in the following sections.

7.1 Pre-processing of the data

The measured data have been filtered to guarantee the integrity of the energy estimation procedure, similarly to the filtering process performed prior to the parameter extraction (see 4.4). Despite the similarity, the filtering process is less strict to have a wider range of different operating conditions in order have a large set of data on which to test the different energy estimation methods.

In particular, on the cleaned *I-V* curves obtained from the MATLAB application (see the first filter in chapter 4.4), three additional filters have been applied on all the available measure:

1. *Shadow filter*: its application is less strict compared to that employed for the parameter extraction procedure. The goal is only to remove those curves affected by mismatch which presents multiple maximum power points, since neither of the proposed methods can predict this kind of behaviour. In this sense, only the filter on the power curve is performed to check if there are multiple peaks. All the curves with multiple peaks are descarted from the analysis.
2. *Irradiance check bit filter*.
3. *Sunny, Cloudy and Partially Cloudy Day filter*: this last filter is applied simply to divide the available measures in three different categories, depending on the kind of day on which the measures were taken. This is achieved by analyzing the measured irradiances curves of each day.

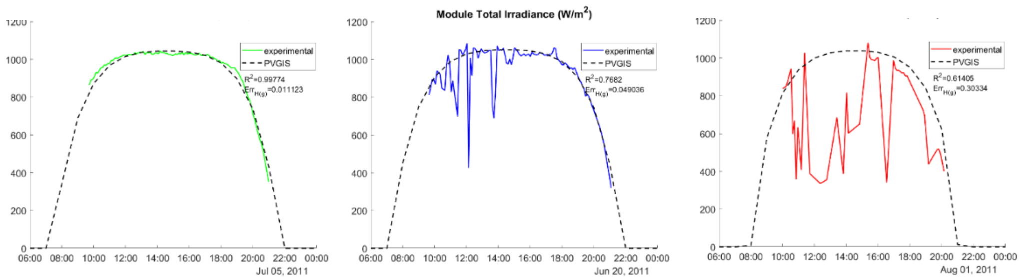

Figure 7-1: Distinction between the three days categories: sunny (green), partially cloudy (blue), cloudy (red)

As shown in figure (7-1), it is possible to identify three typologies of days. Sunny days, when the day is characterizes by the overall clear sky condition and a regular shape of the irradiance curve. Partially cloudy days, when there are a few clouds that temporary shade the sun from view. In these kinds of days it is still possible to recognize the typical shape of the irradiance curve. Cloudy days, when the day is characterized by overall cloudy condition and the irradiance curve presents many irregularities.
The distinction between the three days is achieved by applying two types of filters. The first is able to detect the sunny day by checking if the shape of the irradiance curve presents some irregularities. This is achieved by comparing the irradiance curve with a Fourier series of fourth order. The results of this analysis is the R^2 parameter which is compared to the tolerance value selected. If $R^2 \geq 0.98$, the day is detected as sunny.
Furthermore, in the second filter, the irradiance day curves are compared with the average clear sky irradiance curve taken from PVGIS. PVGIS,

acronim of Photovoltaic Geographical Internation system, is a database that contains a wide range of information about solar radiation for any given location in Europe and Africa. For the application of this filter, the average monthly values of the irradiance day curve in clear sky condition is extracted for the location in which the measuring took place (Higher Technical College of the University of Jaèn). This average curves are then used to compare the measured values. In fact, as shown in figure (5-3), the presence of a cloud is always associated with an irradiance drop. Thus, by computing the error between the expected irradiation in clear sky conditions and the irradiation computed with the measured value, it is possible to identify partially cloudy day from cloudy day. The irradiation calculation is implemented through the estimation of the integral of the irradiance over time, considering the irradiance curve as a step wise function. The computation is achieved by using the MATLAB function 'trapz'. The error is then estimated with the following formula:

$$Err_g = \frac{|H_{measured} - H_{PVGIS}|}{H_{PVGIS}} \tag{7-1}$$

Where:

- $H_{measured}\ \left(\frac{J}{m^2}\right)$, is the irradiation obtained from the measured irradiance values.
- $H_{PVGIS}\ \left(\frac{J}{m^2}\right)$, is the irradiation obtain from the average values taken from PVGIS.

This value is compared with the selected tolerance value. If $Err_g \geq 0.27$, the day is detected as partially cloudy. Else, the day is detected as cloudy. It is important to state that all tolerance values have been found after testing the filter on a wide range of data.

7.2 Power computation

The procedure receives as input the filtered set of data and performs the computation of maximum power point in four different ways, considering every given couple of irradiance and temperature.

Firstly, the experimental values are simply evaluated from the measured P-V curves by finding the maximum. Then, the correlations found in chapter 6 are used to estimate the five parameters for all the available measure of irradiance and temperature. Then, these parameters are used to draw the *I-V* curve and find the maximum power point. Lastly, the Osterwald method is used to estimate the power at maximum point. Its equation can be expressed as follows:

$$P_{Osterwald} = P_{STC} \cdot \frac{G}{G_{STC}} \cdot \left[a + \frac{\gamma}{100}\left(T_c - T_{c,STC}\right)\right] \tag{7-2}$$

Where:

- $G_{STC}\ \left(\frac{W}{m^2}\right)$, is the irradiance in standard test conditions ($1000\,\frac{W}{m^2}$).
- $T_{c,STC}\ (K)$, is the temperature in standard test conditions ($298.15\ K$) .
- $P_{STC}\ (W)$, is the power in standard test conditions from the manufacturer datasheet.
- $G\ \left(\frac{W}{m^2}\right)$, is the irradiance.
- $T_c\ (K)$, is the temperature.
- $\gamma\ \left(\frac{\%}{K}\right)$, is the power thermal coefficient from the manufacturer datasheet.

7.3 Energy computation

The last step of the procedure consists in the energy estimation. The estimation of energy is implemented by integrating in time the maximum power point values. The integration is made considering the power as a step wise function on which it is possible to apply the rectangular rule. This means that for each ‘step’, the integral is estimated as the area of the triangle (base times height), where the height is given by the maximum power point value and the base by the width of the step. A step is usually considered as the time difference between each successive measurement acquisition. In this sense, the MPP point is adopted at midpoint. In addition, a maximum step is imposed to avoid the integration on a large time step whenever there is a lack of measuring points close with each other.

The energy is calculated with the following formula:

$$E = \sum_{i=1}^{N_{tot}} \mathrm{P}_{\mathrm{MPP,i}} \cdot \Delta t_i \tag{7-3}$$

Where:

- $\mathrm{P_{MPP,i}}$ (W), is the maximum power point of step i.
- Δt_i (s), is the time step used to compute the energy. It is equal to the time step between two successive measures if its value is lower that the maximum step. Otherwise it is equal to the maximum.

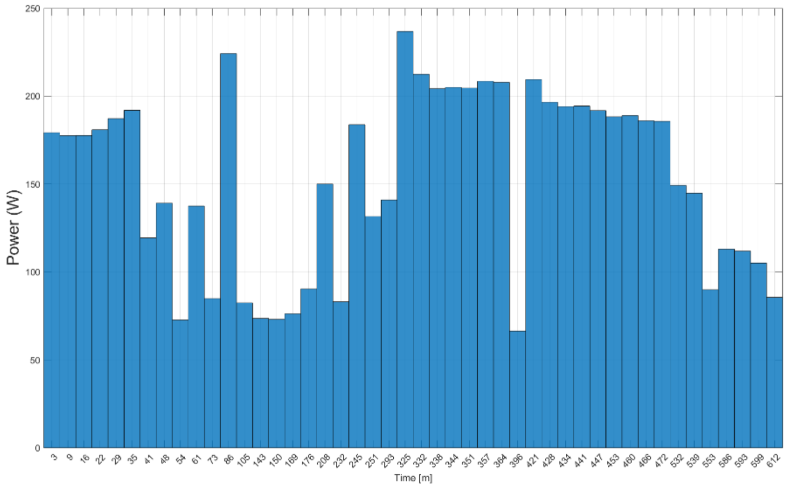

Figure 7-2: Graphical representation of the energy estimation procedure

As shown in figure (7-2) it is possible to see the integration time step over which the energy estimation procedure is carried out. Each bar has an height equal to the fixed value of maximum power for the specific time step. Moreover, at the centre of the bar is possible to observe the time (in minute) with respect to the starting of the measure, for which the time is set to 0. The daily energy is simply given by the area of the various rectangle (in blue).

7.4 Validation of the results

In order to compare the three methods used (LM, SA-NM and Osterwald) in terms of accuracy, the results are compared with respect to the experimental values. In this sense, two additional quantities are estimated to assess the goodness of the energy estimation procedure:

The *normalized root mean square error (NRMSE) on power*. This error is computed between the experimental and the estimated values of power for each method used. Its expression is the following:

$$NRMSE_{P_{MPP}} = \frac{\sqrt{\frac{\sum_{i=1}^{N_{points}}\left(P_{MPP_{estimated}} - P_{MPP_{experiment}}\right)^2}{N_{points}}}}{\frac{\sum_{i=1}^{N_{points}} P_{MPP_{experiment}}}{N_{points}}} \cdot 100 \qquad (7\text{-}4)$$

Where:

- $P_{MPP_{estimated}}$ (W), is the estimated maximum power point with the method in analysis.
- $P_{MPP_{experiment}}$ (W), is the experimental value of the maximum power point.
- N_{points}, is the number of experimental points.

The *percentage error on energy estimation*. This error is computed between the experimental and estimated values of energy for each method used. Its expression is the following:

$$Err_E = \frac{E_{estimated} - E_{experiment}}{E_{experiment}} \cdot 100 \qquad (7\text{-}5)$$

Where:

- $E_{estimated}$ (J), is the estimated energy with the method in analysis.
- $E_{experiment}(J)$, is the experimental energy.

Chapter 8

Experimental Campaigns

Data from previous experimental campaigns carried out in 2011 and 2012 have been used in order to overcome the lockdown aftermaths. In fact, given the exceptional circumstance which had to be faced due to Covid-19, the planned six-month experimental campaign that this work was supposed to be based on could not be conducted.

The measuring system described in chapter 4 was used to carry out the experimental campaign. Moreover, the PV module selected for this study belong to HIT and thin films technologies (such as CIGS and CdTe). In particular, the HIT (Sanyo) module was measured by the Tracker system whilst the CIGS (Avancis) and the CdTe (First Solar) modules were measured by the Fixed system. In addition, it is important to state that prior to starting the experimental campaign all the PV module under test were calibrated by an independent certified laboratory (CIEMAT laboratory). The aim of the calibration was to obtain the main electrical characteristics and check for the electrical response of the modules. This step was necessary to guarantee non-defective *I-V* curves and therefore to ensure the accuracy and the significance of the overall study.

In this chapter a brief description of the module under-test and of the corresponding experimental campaign will be carried out, with particular emphasis on the data set available and on the filtering procedure applied for the purpose of this study.

8.1 HIT module

The HIT technology (Heterojunction with Intrinsic thin layer) is composed of a mono thin crystalline silicon wafer surrounded by ultra-thin amorphous silicon layer. As already described in chapter 2.3.4, it presents many advantages and is considered a promising low-cost alternative to traditional crystalline silicon based solar cells.

In particular, the model of the module under test is a Sanyo HIT 240-HDE4 module. The main specification from manufacturer and calibration are summarized in the following tables:

	P_{MPP} (W)	*V_{MPP} (V)*	*I_{MPP} (A)*	*V_{oc} (V)*	*I_{sc} (A)*	*FF (%)*
manufacturer	240	35.5	6.77	43.6	7.37	74.8
CIEMAT lab	233	32.3	7.23	42.2	7.54	73.3

Table 8-1: Main specification of the Sanyo HIT module

	α (I_{sc}) (%/°C)	*β (V_{oc}) (V/°C)*	*γ (P_{max}) (%/°C)*	*NOCT (°C)*
manufacturer	0.03	-0.109	-0.30	45

Table 8-2: Temperature coefficients of the Sanyo HIT module

The calibration of the PV module was performed in May 2011. The PV module was mounted on the Tracker measuring system. The corresponding experimental campaign was carried out between June and December 2011, with an interruption between October and November. In the seven months experimental campaign a large set of data was recorded in a wide range of operating conditions. In this sense, an overview of the most important atmospheric parameters will be provided to get an idea of the available data set.

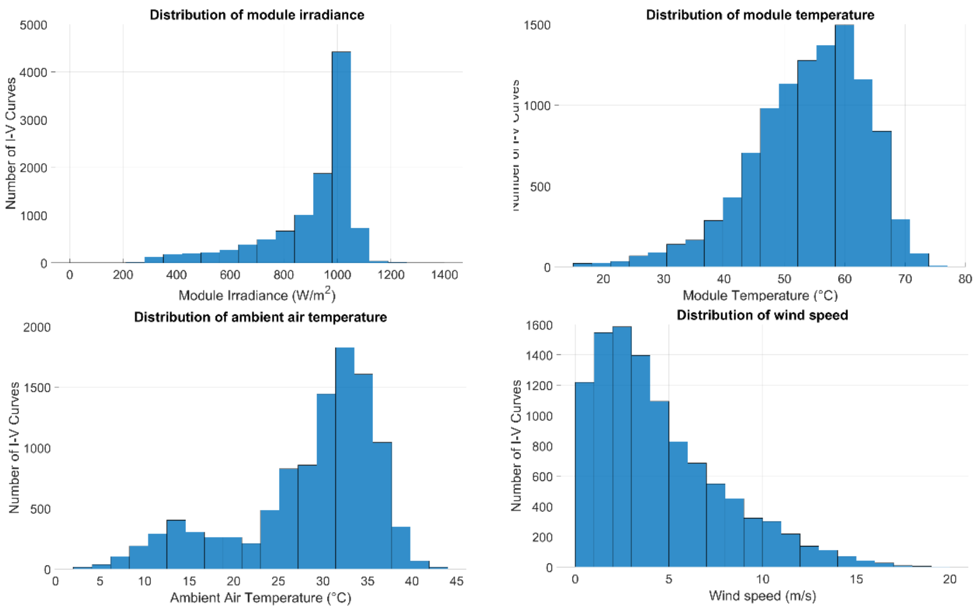

Figure 8-1: Density distribution of the most important atmospheric parameters over the overall set of experimental points for Sanyo HIT module.

Firstly, the density distribution of these parameters can be observed in figure (8-1). Due to the use of the Tracker system to perform the measurements, the irradiance distribution presents a higher concentration of values around 1000 W/m^2. The cell temperature distribution on the other hand presents a more spread range of values, even though there still is a higher concentration of values at higher temperatures (around 50-60 °C). This is comprehensible since higher temperatures can be expected at higher values of irradiance as the module undergoes a stronger heating when subjected to more intense sun light. Moving on to the atmospheric conditions that are not related to the module itself, it can be observed that the wind distribution presents a decreasing trend as the wind speed values increase. This is good since it is better to have values below 5 m/s to guarantee a good accuracy of the measurements. Moreover, the ambient air temperature is more or less spread out across the overall range, with the exception of a higher concentrations of points around 30°C. This could be related to the fact that most of the experimental campaign was carried out in the warmer months of the year.

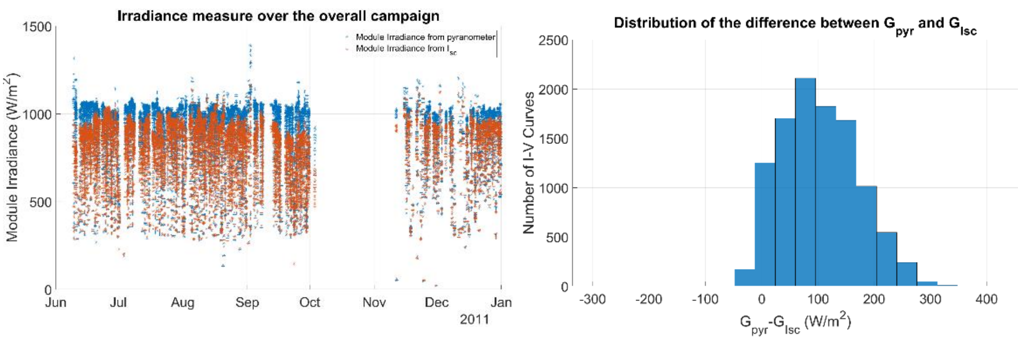

Figure 8-2: Irradiance measures over the entire campaign (left) and distribution of the difference between the two irradiance measure (right) for Sanyo HIT module.

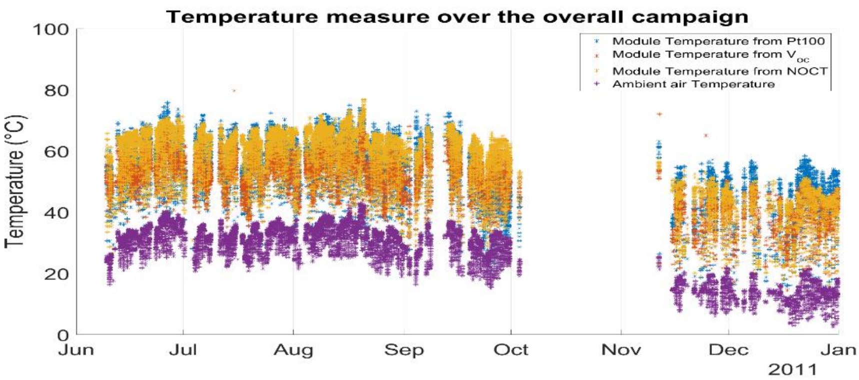

Figure 8-3: Temperature measures over the entire campaign for Sanyo HIT module.

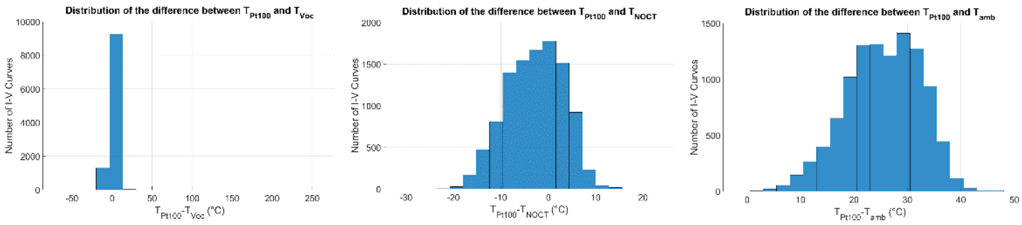

Figure 8-4: Distribution of the difference between the measured temperature with PT100 sensor and the other available temperature measures for Sanyo HIT module.

In addition, it is possible to check the reliability of the measures by analysing the irradiance and temperature data. In particular, focusing on the irradiance, it is possible to check the reliability of the measure by comparing the measured value with that computed from the short circuit current (Eq 1-20). The results are shown in figure (8-2). Since the irradiance computed from short circuit current has only a theoretical nature, its value should only be used for reference purposes, to check if the measured irradiance is behaving as expected. In this sense, measures whose difference is above 100 W/m^2 should be considered unreliable or at least should be checked further to guarantee reliability. Similarly, focusing on the module temperature, it is possible to check the reliability of the PT100 sensor by comparing the value with those obtained from open circuit voltage (Eq 1-21) and from the NOCT formulation (Eq 2-2), as well as ambient air temperature. The results of the analysis are presented in figure (8-3) and (8-4). Regarding the difference with the ambient air temperature, the measure provided by the PT100 should always be around 10 °C higher (acceptable in the morning). This lower bound is imposed since it is very unlikely for the heated PV module to maintain a temperature this close to that of the surrounding air, even when irradiance is low. Moreover, concerning the module temperature, the temperature estimated through V_{oc} and NOCT should only be used for references purposes. In this sense, a difference between those values and that measured by PT100 sensor should always be below 10 to guarantee the reliability of the measure. However, it is important to state that the range of operation of the NOCT formulation is around 800-1000 W/m^2 for irradiance and around 20 °C for ambient air temperature. Outside this range, the formulation loses its effectiveness, therefore the presence of points in the distribution outside the 10 °C mark could simply be related to this limit.

Finally, for the specific purpose of this study, the information provided by the experimental measures and the filtering procedure discussed in chapter 5, were combined to filter the dataset available for the Sanyo HIT module. The overall filtering process can be summarized in the following table

Filtering process for the parameter extraction procedure	*Filtering process for the energy estimation procedure*
Irradiance check-bit filter Complete shadow filter Wind speed < 5 m/s Monotonicity > 0.6	Irradiance check-bit filter Partial shadow filter

Table 8-3: Filtering process for the Sanyo HIT module.

In the end, of the 11123 measures acquired, only 10599 are reliable and have been used for energy estimation purposes. Moreover, for what concerns the parameter extraction, only 1545 curves remained after the various filter

8.2 CIGS thin film module

The CIGS (Copper Indium Gallium Selenide) solar cells belong to the thin films technology. In particular, the module under test is an Avancis PowerMax 120FB module. Moreover, the main specification from manufacturer and calibration are summarized in the following tables:

	P_{MPP} (W)	V_{MPP} (V)	I_{MPP} (A)	V_{oc} (V)	I_{sc} (A)	FF (%)
manufacturer	120	43.1	2.79	59.7	3.18	63.3
CIEMAT lab	113	41.9	2.69	59	3.09	61.7

Table 8-4: Main specification of the Avancis module

	α (I_{sc}) (%/°C)	β (V_{oc}) (V/°C)	γ (P_{max}) (%/°C)	NOCT (°C)
manufacturer	0.008	-0.52	-0.37	52.6

Table 8-5: Temperature coefficients of the Avancis module

The calibration of the PV module was performed in May 2011. The corresponding experimental campaign was carried out between January and December 2012. In particular, the measurement was achieved by means of the Fixed system presented in chapter 4. As with the previous module, an overview of the most important atmospheric parameters will be provided to get an idea of the available data set.

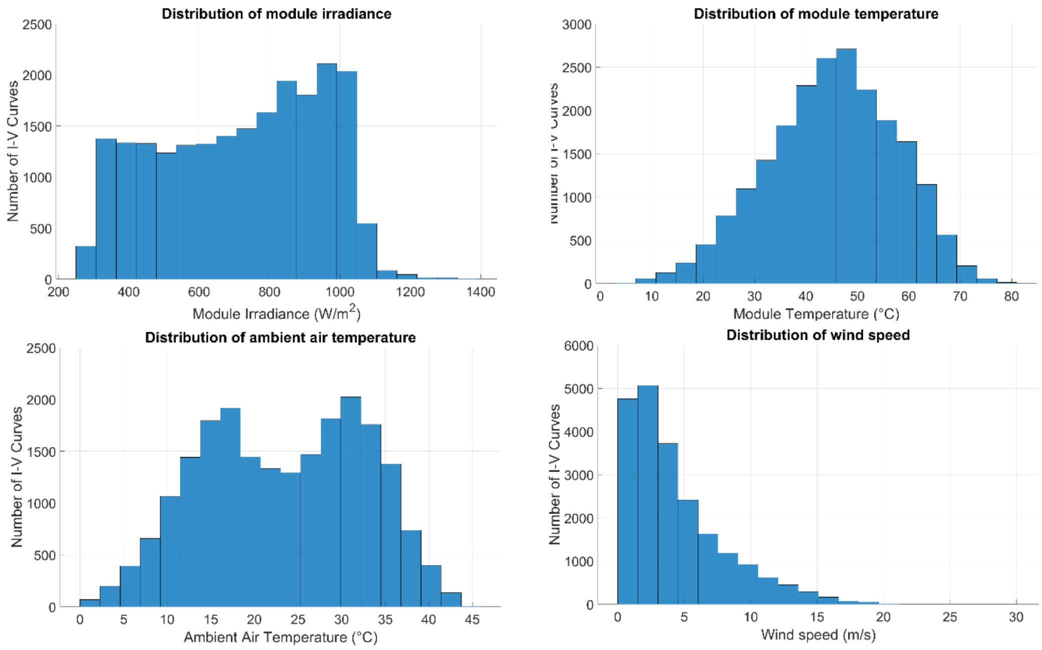

Figure 8-5: Density distribution of the most important atmospheric parameters over the overall set of experimental points for Avancis module.

As shown in figure (8-5), the irradiance distribution presents a more homogeneous distribution compared to that of the previous experimental campaign for the HIT module. In fact, the use of the Fixed system is cause of some angular losses. This means that when the sun rays are not perpendicular to the surface, the pyranometer is not able to measure as accurately the irradiance value. Similar observation as those presented in chapter 8.1 can be made on the other parameters. Moreover, the ambient air temperature presents a more homogeneous distribution due to the fact that the experimental campaign was carried out over the whole year.

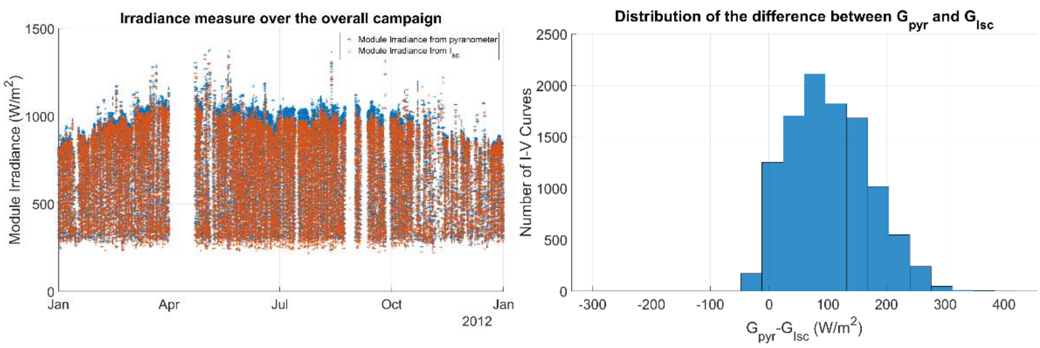

Figure 8-6: Irradiance measures over the entire campaign (left) and distribution of the difference between the two irradiance measure (right) for Avancis module.

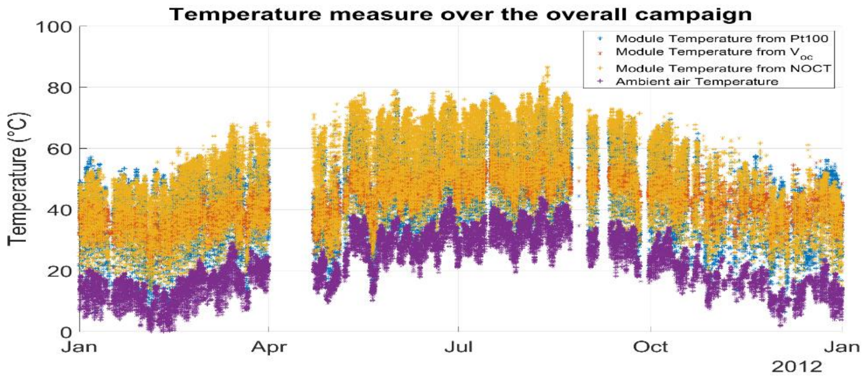

Figure 8-7: Temperature measures over the entire campaign for Avancis module.

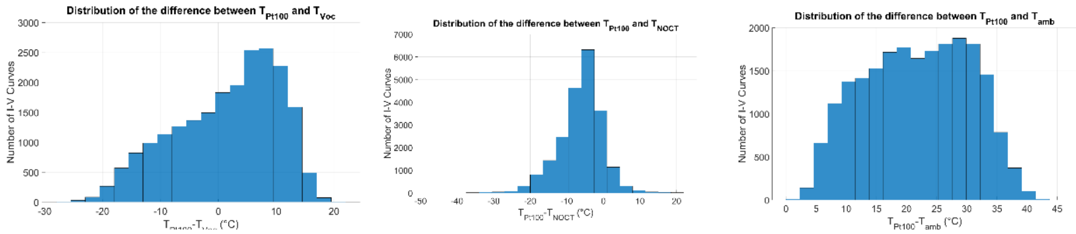

Figure 8-8: Distribution of the difference between the measured temperature with PT100 sensor and the other available temperature measures for Avancis module.

By looking at figures (8-6), (8-7) and (8-8) it is possible to analyse the accuracy of the available dataset. In particular, the reliability of the irradiance measure is guaranteed by the distribution of the difference between the two irradiance values, which is almost always below 100 W/m^2 in absolute terms. Similarly, the reliability of the temperature measure is guaranteed as well, as all the distribution present in figure (8-8) comply with the criteria identified in chapter 8.1.1.

Finally, the filtering procedure applied to this dataset is summarized in the following table. In the end, from the 23304 available measurements, 21328 were kept for the energy estimation and only 907 for the parameter extraction procedure.

Filtering process for the parameter extraction procedure	*Filtering process for the energy estimation procedure*
Irradiance check-bit filter Complete shadow filter Wind speed < 5 m/s Monotonicity = 1 $T_{PT100} - T_{amb} \geq 15\ °C$	Irradiance check-bit filter Partial shadow filter

Table 8-6: Filtering process for the Avancis module.

8.3 CdTe thin film module

The CdTe (Cadmium Telluride) solar cells belong to the thin films technology. The prominent manufacturer of CdTe thin film technology is the company First Solar. In particular, the module under test is a First Solar FS270 module. The main specification from manufacturer and calibration are summarized in the following tables:

	P_{MPP} (W)	V_{MPP} (V)	I_{MPP} (A)	V_{oc} (V)	I_{sc} (A)	FF (%)
manufacturer	70	65.5	1.07	88.0	1.23	64.7
CIEMAT lab	67.3	66.7	1.01	91.1	1.19	62.1

Table 8-7: Main specification of the First Solar module

	α (I_{sc}) (%/°C)	β (V_{oc}) (V/°C)	γ (P_{max}) (%/°C)	NOCT (°C)
manufacturer	0.04	-0.25	-0.25	52.6

Table 8-8: Temperature coefficients of the First Solar module

The calibration of the module was performed in July 2010. The experimental campaign exploiting the Fixed system was carried out between January and December of 2012.

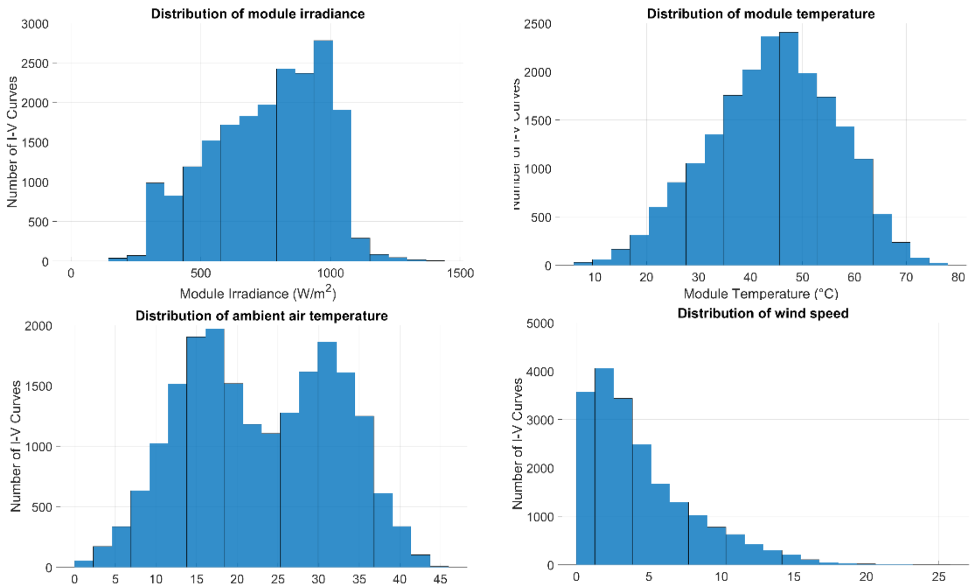

Figure 8-9: Density distribution of the most important atmospheric parameters over the overall set of experimental points for First Solar module.

In figure (8-9) the density distribution of the most important atmospheric parameters over the overall set of experimental points can be observed. The various tendencies follow the same behaviour as that shown in figure (8-5) since both modules were mounted on the same Fixed system when the experimental campaign was carried out. For this reason, the same observations can be made for the reliability of the irradiance and temperature measurements, shown in figures below.

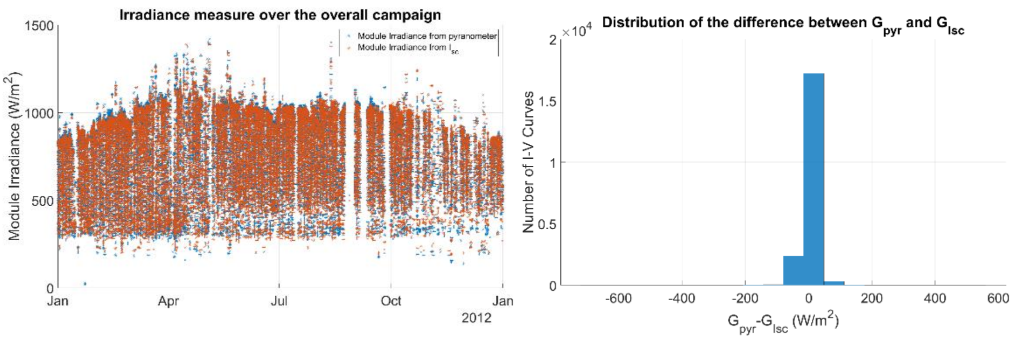

Figure 8-10: Irradiance measures over the entire campaign (left) and distribution of the difference between the two irradiance measure (right) for First Solar module.

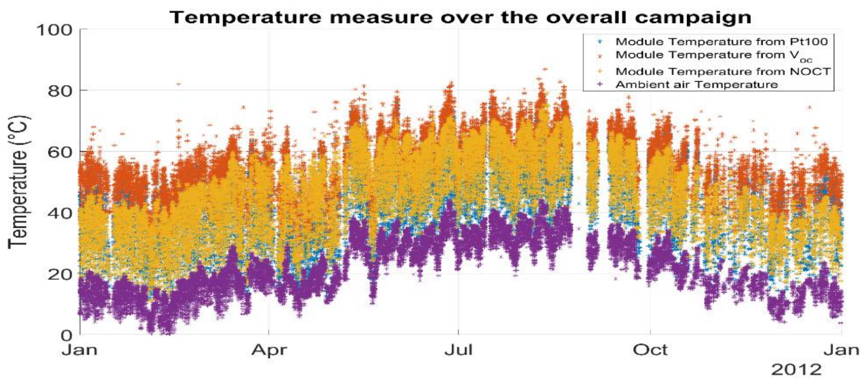

Figure 8-11: Temperature measures over the entire campaign for First Solar module.

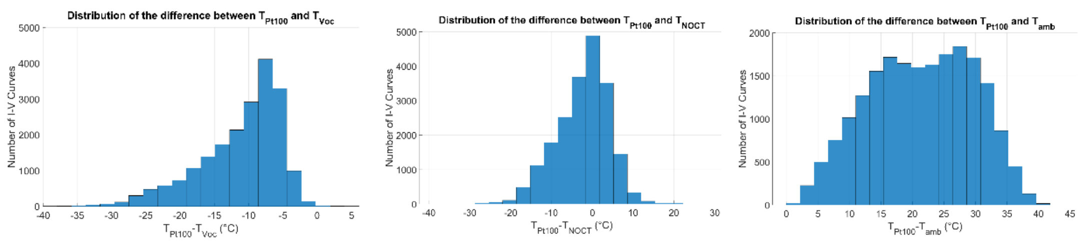

Figure 8-12: Distribution of the difference between the measured temperature with PT100 sensor and the other available temperature measures for First Solar module.

The filtering procedure applied to this dataset is summarized in the following table.

Filtering process for the parameter extraction procedure	*Filtering process for the energy estimation procedure*
Irradiance check-bit filter Complete shadow filter Wind speed < 5 m/s Monotonicity = 1	Irradiance check-bit filter Partial shadow filter

Table 8-9: Filtering process for the First Solar module.

In the end, from the 24559 available measurements, 20084 were kept for the energy estimation and only 9373 for the parameter extraction procedure.

Chapter 9

Analysis of the results

In this chapter the results of the experimental analysis will be presented. In particular the discussion will be carried out separately for the three modules analysed, focusing on three main aspects:

- The results of the parameters extraction procedure in terms of accuracy, quality and computational cost in order to compare the performance of LM and SA-NM.
- The discussion of the obtained correlations and of the error associated to each parameter.
- The comparison of the three methods previously discussed for power and energy estimation purposes.

9.1 HIT module

I. Parameters extraction

As mentioned in the previous chapter, the goal of the parameters extraction procedure is to obtain a set of parameters that is able to approximate as best as possible the *I-V* curve in analysis using the explicit transcendental equation (Eq 1.26). This process has been applied to all the 1545 curves. Nonetheless, after the extraction, the set of parameters has been filtered to remove those affected by overfitting. The following filters have been applied:

- Series Resistance below 0.3 Ω.
- Shunt Resistance below 5000 Ω.
- NRMSE below 0.015
- Error on Maximum Power below 2%.

In the end, the feasible parameters left were 601 for Levenberg-Marquardt algorithm and 881 for Simulated-Annealing and Nelder-Mead.

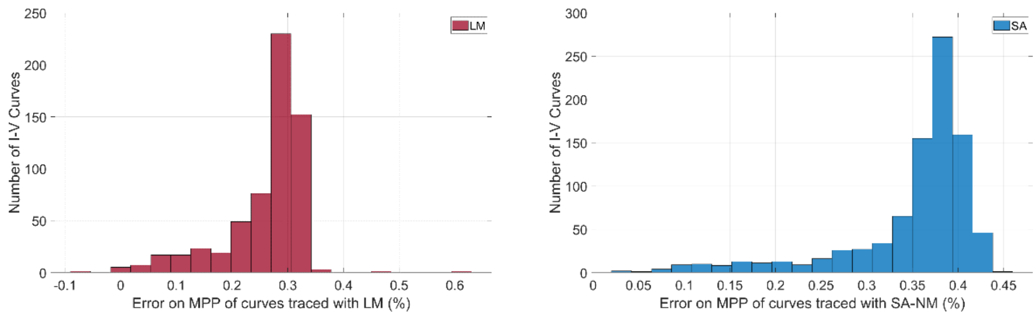

Figure 9-1: Error on Maximum Power of the fitting procedure for Sanyo HIT module.

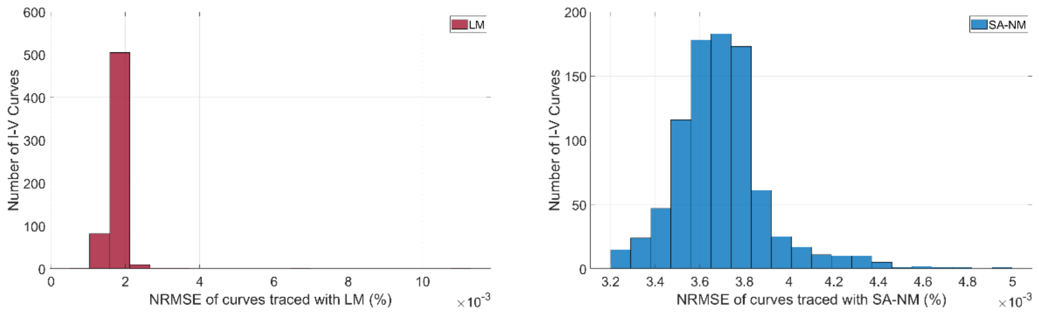

Figure 9-2: NRMSE of the fitting procedure for Sanyo HIT module.

	Levenberg-Marquardt	*Simulated-Annealing & Nelder-Mead*
$NRMSE_{,avg}$ *(-)*	0.0018	0.0037
$ErrPmax_{,avg}$ *(%)*	0.26	0.36
$FittingTime_{,avg}$ *(s)*	59.7	18.6

Table 9-1: Average parameters of the fitting procedure for Sanyo HIT module

In figure (9-1) and (9-2) the density distribution of the NRMSE and of the error on maximum power point for the remaining curves is presented. While both methods have proven to be valid for this application, it can be observed that the method using Levenberg-Marquardt algorithm performs slightly better in terms of accuracy. Moreover, a further comparison can be made taking into consideration the fitting execution time, which is a measure of the computational cost associated with the implementation of each algorithm. Considering the average values, shown in table (9-1), the SA-NM method has proven to be a lot faster compared to LM, balancing out the previously mentioned difference. In fact, the higher accuracy of the LM algorithm is paid by the higher computational cost.

In figure (9-3) is shown a comparison between the measured curves and those estimated with the parameters extracted with Levenberg-Marquardt algorithm. In particular, it can be observed that the applied procedure is able to accurately predict the shape of the *I-V* curve at any given conditions. A similar graph can be made for the curves estimated with SA-NM, but the results are exactly the same since both methods have proven to be valid for this application.

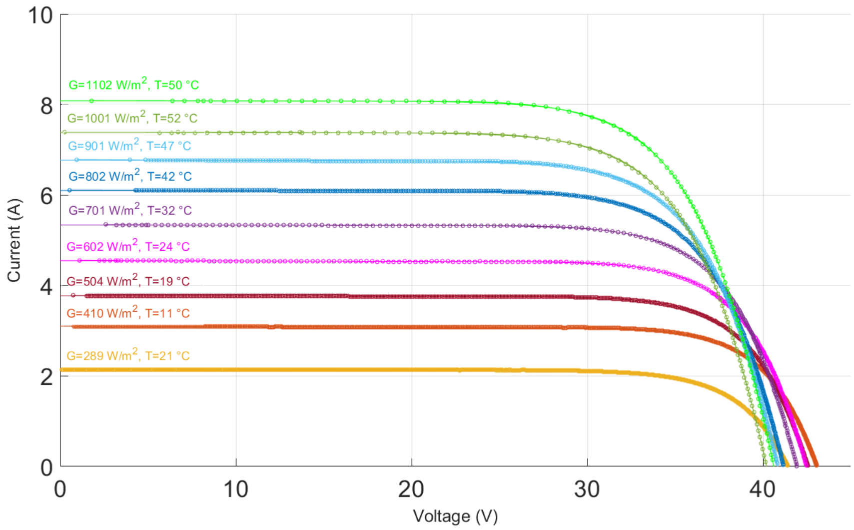

Figure 9-3: Measured (circles) and extracted *I-V* curves at different values of irradiance and temperature with LM algorithm for Sanyo HIT module.

II. Parameters Equations

The extracted parameters have been used to estimate the correlations that describes their behaviour as a function of the atmospheric conditions. The correlations used are those presented in chapter 6. In particular, the procedure has been applied both on the parameters extracted with LM method and on those extracted with SA-NM method. All the parameters will be analysed separately to discuss the accuracy of the correlations as well as the physical meaning associated with each behaviour. Nonetheless the coefficients of the correlations obtained from the non-linear regressions are summarized in the following tables. A detailed description of each coefficient is available in chapter 6.

	I_{ph} (A)	I_0 (A)	n (-)	R_s (Ω)	R_{sh} (Ω)
a	7.44	$2.35\ 10^{-7}$	1.59	0.18	1774
b	0.0003	0.66	$4.64\ 10^{-5}$	-0.20	
c		1.121	$5.15\ 10^{-4}$		

Table 9-2: Coefficients of the correlations with LM method for Sanyo HIT module

	I_{ph} (A)	I_0 (A)	n (-)	R_s (Ω)	R_{sh} (Ω)
a	7.39	$2.63\ 10^{-7}$	1.59	0.18	1898
b	0.0003	0.62	$5.72\ 10^{-5}$	-0.21	
c		1.121	$2.15\ 10^{-4}$		

Table 9-3: Coefficients of the correlations with SA-NM method for Sanyo HIT module

1. Photogenerated Current

As expected, the photogenerated current has proved to be linearly proportional to the irradiance value, whilst is very disperse with respect to temperature. The final correlations presented in equations (9-1) and (9-2) which are obtained by performing a non-linear regression on equation (6-1). The result of the regression consists only on the value of the optimal a ($I_{ph,STC}$), as the temperature coefficient has been taken from the manufacturer datasheet and considered constant. Moreover, the graphs which shows the correlations of the photogenerated current with respect to irradiance for LM and SA-NM method are shown in figure (9-4) and (9-5).

$$I_{ph} = \mathbf{7.44} \cdot [1 + 0.0003(T_c - T_{c,STC})] \cdot \frac{G}{G_{STC}} \tag{9-1}$$

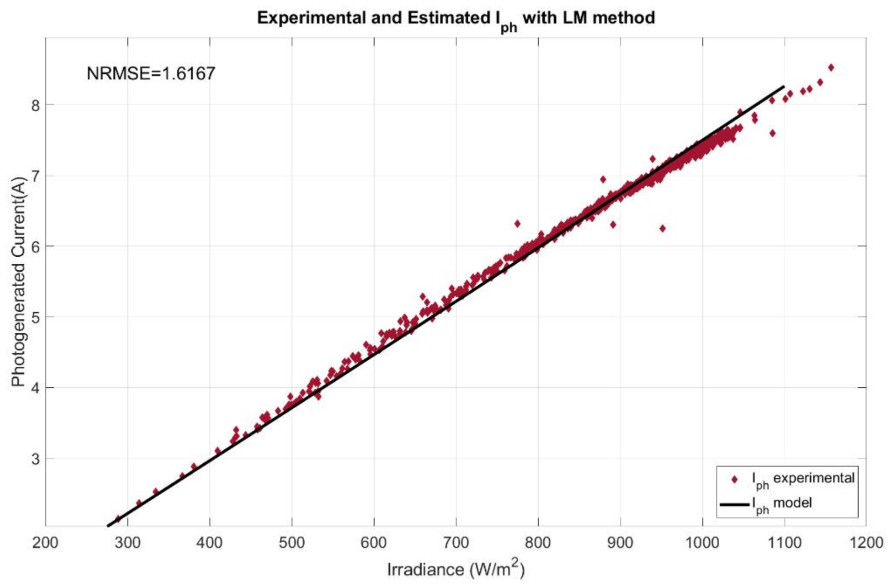

Figure 9-4: Results of the non-linear regression for the photogenerated current estimated with LM method for Sanyo HIT module.

$$I_{ph} = \mathbf{7.39} \cdot [1 + 0.0003(T_c - T_{c,STC})] \cdot \frac{G}{G_{STC}} \tag{9-2}$$

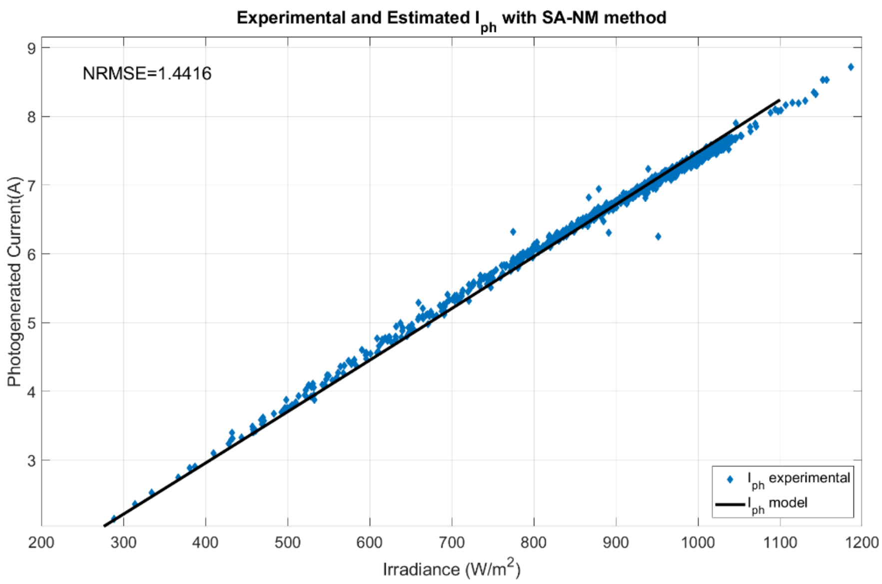

Figure 9-5: Results of the non-linear regression for the photogenerated current estimated with SA-NM method for Sanyo HIT module.

With both methods the NRMSE is very low, around 1.6 % for LM and 1.4 % for SA-NM. This means that the correlations are able to accurately predict the behaviour of the photogenerated current. Moreover, it seems that the correlation obtained with SA-NM method is slightly better.

2. Saturation Current

As expected, the saturation current has proved to be related mainly to the temperature. The non-linear regression aims to optimize the value of a ($I_{0,STC}$). Moreover, since HIT modules is characterized different materials compared to classical monocrystalline module, the coefficient b (χ) has been optimized as well. For this purpose equation (6-5) has been used.

The correlations obtained for the two methods are shown in the following figures. In particular, equation (9-3) and figure (9-6) show the results with LM method, whilst equation (9-4) and figure (9-7) show the results with SA-NM.

$$I_0 = \mathbf{2.35\ 10^{-7}} \cdot \left(\frac{T_c}{T_{c,STC}}\right)^3 \cdot e^{\mathbf{0.66} \cdot \left(\frac{E_{g,STC}}{T_{STC}} - \frac{E_g(T_c)}{T_c}\right) \cdot \frac{1}{k_b}} \tag{9-3}$$

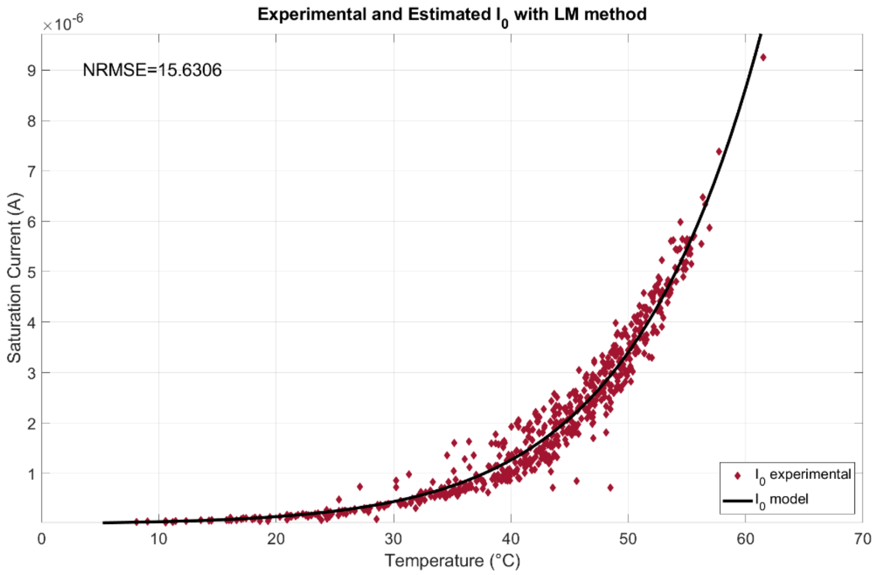

Figure 9-6: Results of the non-linear regression for the saturation current estimated with LM method for Sanyo HIT module.

$$I_0 = \mathbf{2.63\ 10^{-7}} \cdot \left(\frac{T_c}{T_{c,STC}}\right)^3 \cdot e^{\mathbf{0.62} \cdot \left(\frac{E_{g,STC}}{T_{STC}} - \frac{E_g(T_c)}{T_c}\right) \cdot \frac{1}{k_b}} \tag{9-4}$$

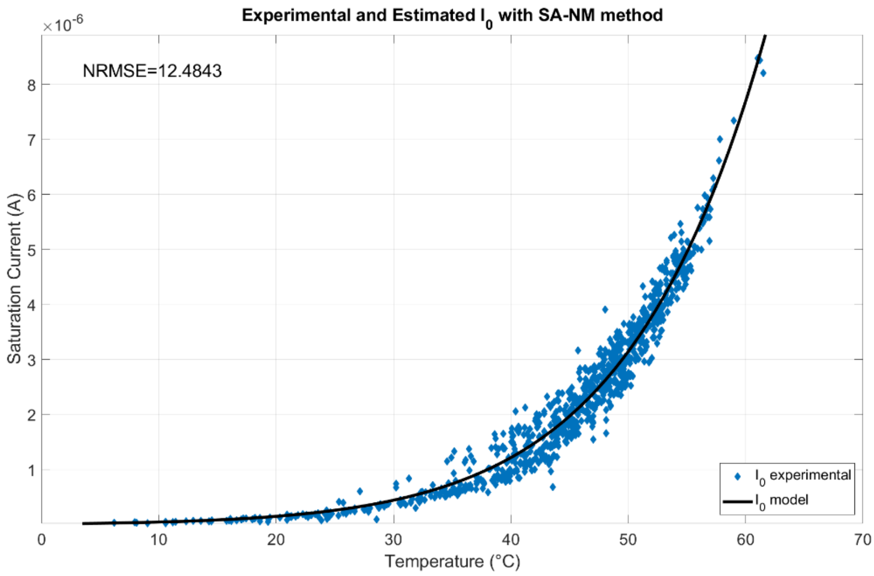

Figure 9-7: Results of the non-linear regression for the saturation current estimated with SA-NM method for Sanyo HIT module.

Once again, the trends follow closely the behaviour of the experimental points even if there is a slightly higher dispersion compared to the photogenerated current. Nonetheless, the NRMSE associated to both correlations is relatively low, around

15% for LM and 12.5% for SA-NM. In particular, the correlation obtained for the SA-NM model is once again better.

3. Diode Ideality Factor

As mentioned in chapter 6, the diode ideality factor is often considered constant in most applications since it doesn’t have a clear relationship with irradiance and temperature. Nonetheless, the results of the non-linear regression applied to the correlations (Eq 6-6), show a linear tendency between the values of n and those of irradiance and temperature. Moreover, it seems that n increases as temperature and irradiance increase. The results for both LM and SA-NM method are shown below both in graphical and mathematical form. The optimization has been performed on the values of a, b and c.

$$n = \mathbf{1.59} + \mathbf{4.64\ 10^{-5}} \cdot G + \mathbf{5.15\ 10^{-4}} \cdot T_c \tag{9-5}$$

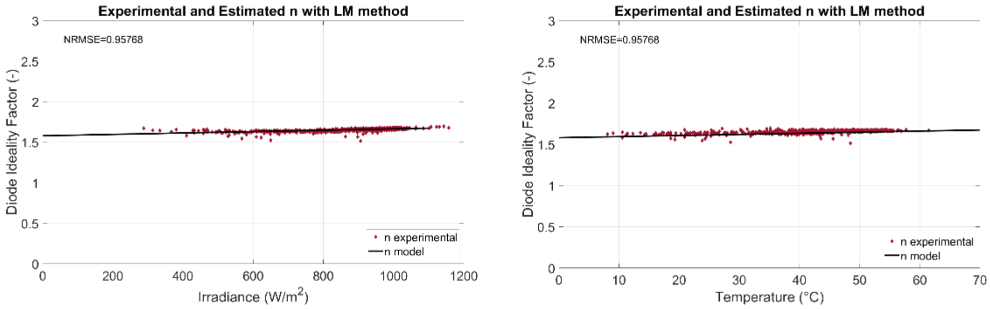

Figure 9-8: Results of the non-linear regression for the diode ideality factor estimated with LM method for Sanyo HIT module.

$$n = \mathbf{1.59} + \mathbf{5.72\ 10^{-5}} \cdot G + \mathbf{2.15\ 10^{-4}} \cdot T_c \tag{9-6}$$

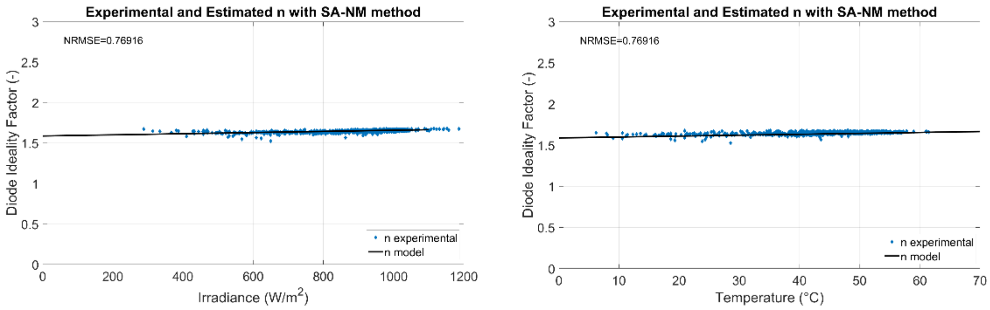

Figure 9-9: Results of the non-linear regression for the diode ideality factor estimated with SA-NM method for Sanyo HIT module.

Once again, the correlations can closely approximate the behaviour of the diode ideality factor. In fact, with both method the NRMSE is below one, being slightly better for SA-NM.

4. Series Resistance

The series resistance has a dependence on both irradiance and temperature. In particular, during the regression performed on equation (6-7), the optimized coefficient are the a ($R_{s,STC}$) and the b (λ_{R_s}). The equations modelling the two correlations for the two methods are (9.7) and (9.8), for LM and SA-NM respectively. Furthermore, in the graphs below, the results of the non-linear regression are presented. It has been decided to show only the dependence with respect to irradiance as it was more relevant compared to that with temperature. In fact, the correlations seem to closely follow the behaviour of the experimental points.

$$R_s = \mathbf{0.18} \cdot \frac{T_c}{T_{c,STC}} \cdot \left[1 - (\mathbf{-0.20}) \cdot log\left(\frac{G}{G_{STC}}\right)\right] \tag{9-7}$$

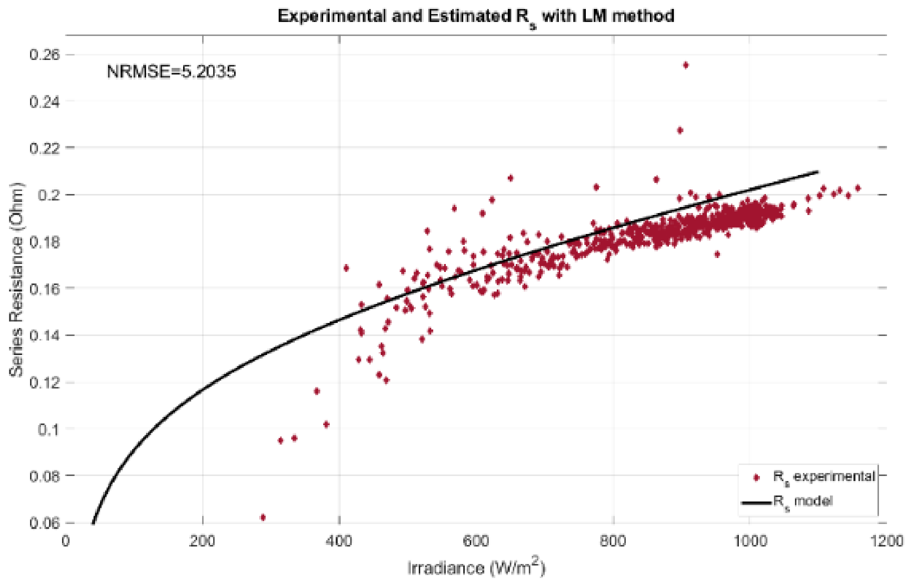

Figure 9-10: Results of the non-linear regression for the series resistance estimated with LM method for Sanyo HIT module.

$$R_s = \mathbf{0.18} \cdot \frac{T_c}{T_{c,STC}} \cdot \left[1 - (\mathbf{-0.21}) \cdot log\left(\frac{G}{G_{STC}}\right)\right] \tag{9-8}$$

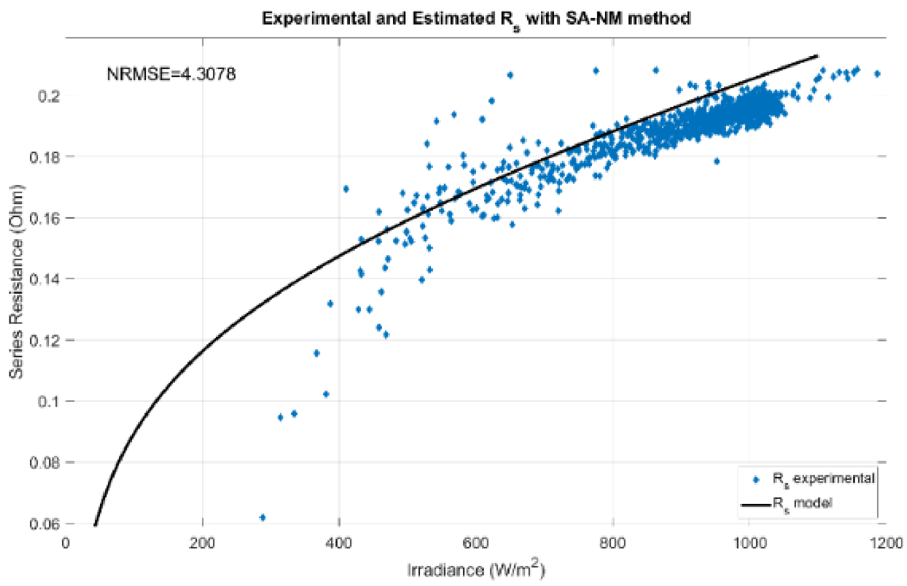

Figure 9-11: Results of the non-linear regression for the series resistance estimated with SA-NM method for Sanyo HIT module.

With both methods, the series resistance has similar tendencies with both irradiance and temperature. In fact, the parameter λ_{R_s} is negative since the series resistance increases with both. Moreover, as expected, the values of the series resistance are around 0.1 and 0.22, which are the typical values for these kinds of technologies.

Lastly, regarding the NRMSE on the correlation, its value is 5.2% for LM and 4.3 for SA-NM, which proves once again that the correlations achieved with SA-NM are able to accurately predict the behaviour of the parameters.

5. Shunt Resistance

The shunt resistance presents a very disperse behaviour both with irradiance and temperature. This can simply be related to the fact that the effect of the shunt resistance is very negligible on the overall I-V curve equation and therefore is not possible to identify a clear trend. Its value could have been considered constant, but it has been decided to apply the correlations nonetheless. In particular, during the non-linear regression procedure, the parameter to be optimized was a ($R_{sh,STC}$) in equation (6-8). The mathematical expression of the correlations implemented with the two methods is presented below.

$$R_{sh} = \mathbf{1774} \cdot \frac{G_{STC}}{G} \tag{9-9}$$

$$R_{sh} = \mathbf{1898} \cdot \frac{G_{STC}}{G} \tag{9-10}$$

Due to the high dispersion of the points, it has been decided to not insert the graphical representation of the experimental points and of the correlations since there is no clear observable tendency. In fact, the NRMSE of both correlations is very high. Nonetheless, the one with the SA-NM method is still better, being 50% compared to the 52.7% of the one with LM.

Figure (9-12) shows the normal root mean square error associated with each correlation. As mentioned before, the SA-NM method is able to provide correlation with higher accuracy for all five parameters. Nonetheless, it's important to note that this could also be related to the fact that the number of experimental points available for the SA-NM regression is higher compared to that employed in the LM one.

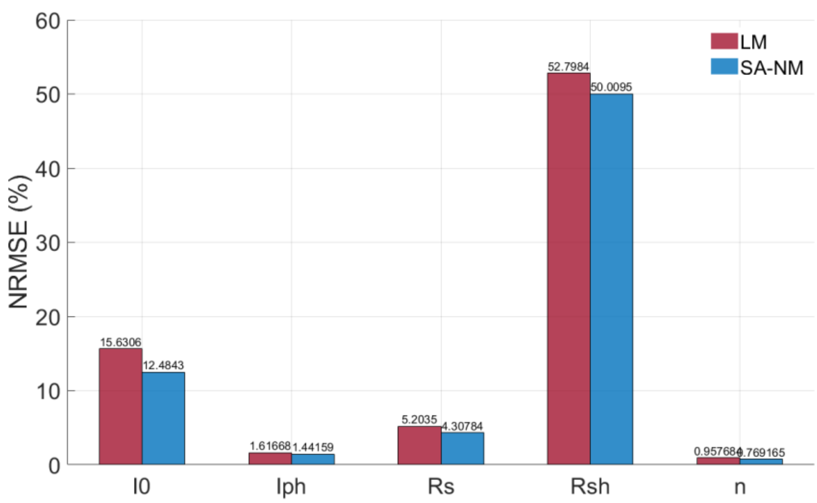

Figure 9-12: NRMSE of each parameters correlation for Sanyo HIT module

Lastly, in figure (9-13) the same curves presented in figure (9-3) are shown, comparing the measured curves with those estimated using the correlations and the transcendental equation. As expected, the results are not as accurate as they were in figure (9-3) since the parameters associated to each curve are no longer those optimized precisely to approximate that shape. Nonetheless, the curve estimated through the correlation are still very accurate.

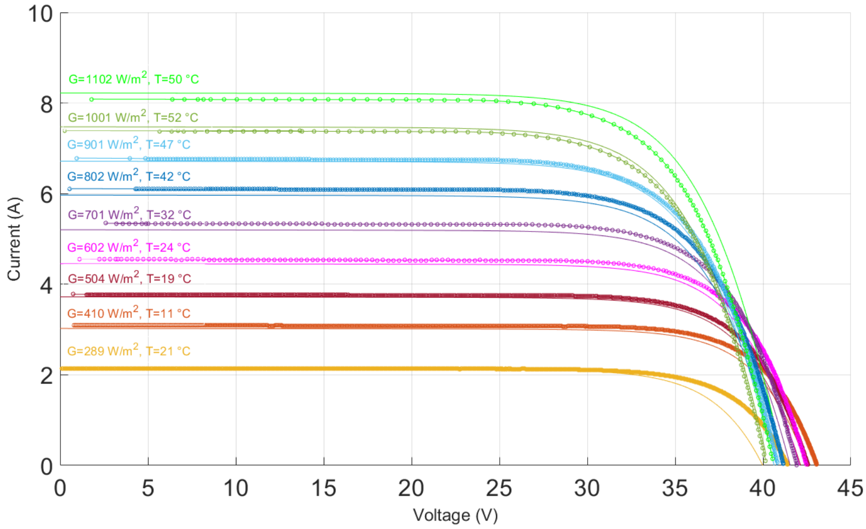

Figure 9-13: Measured (circles) and modelled *I-V* curves at different values of irradiance and temperature with LM correlations for Sanyo HIT module

III. Power and Energy estimation

The last step of the analysis consists in the power and energy estimation to compare the three methods: LM, SA-NM and Osterwald. The dataset used for this estimation is no longer the same used to extract the parameter and evaluate the correlations. This new dataset is larger and less restrictive in order to test the validity of the various method to a wide range of different operating conditions.

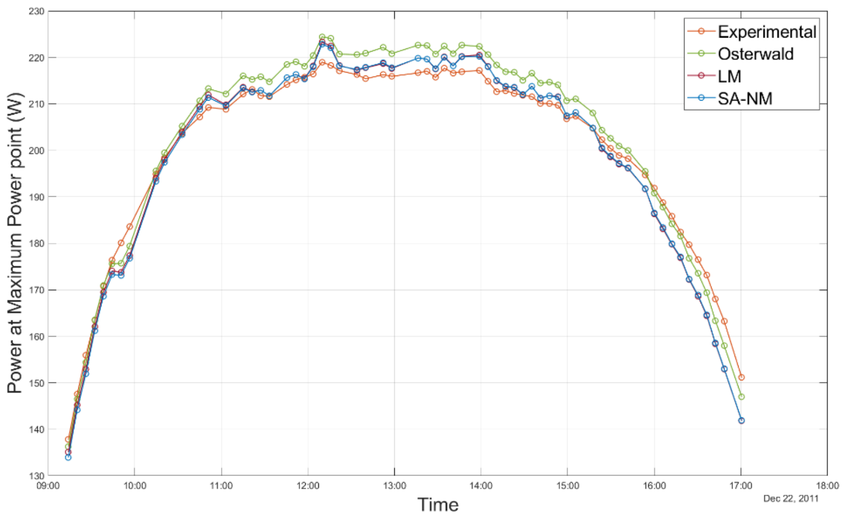

Figure 9-14: Power at Maximum Power Point for a given day for Sanyo HIT module

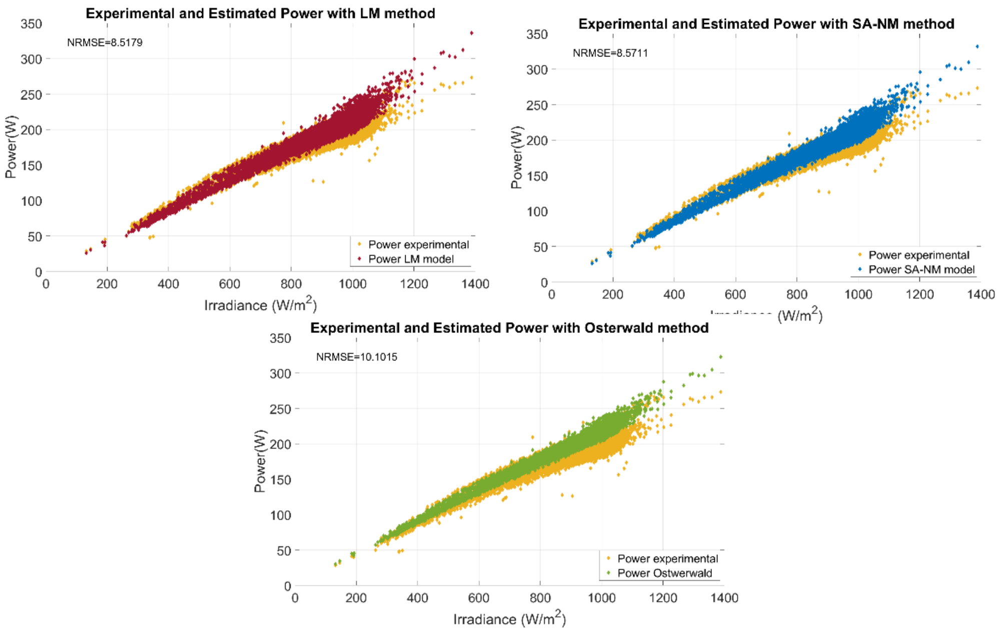

Figure 9-15: Comparison of power at MPP between experimental points and those estimated with the various method for Sanyo HIT module

Firstly, the power estimated according to the three method can be compared for a typical day. As shown in figure (9-14), LM and SA-NM models are very closed to each other and are able to follow closely the real evolution of the experimental measured. On the contrary, Osterwald method is often overestimating the power, especially at higher values of irradiance (during mid-day). Moreover considering the analysis over the complete time in which the measure are available, it's possible to compare the experimental points with those obtained from LM and SA-NM method, as well as those obtained with Osterwald method. In particular, figure (9-15), shows the distribution of the experimental and estimated points as a function of irradiance. All three methods overestimate the power at higher values of irradiance. Nonetheless LM and SA-NM are slightly better compared to Osterwald. In this sense, to better compare the three methods, it's possible to compute the error on the estimation of energy and the NRMSE on the estimation of maximum power. The results are shown in the figure below. As mentioned in chapter 7, a distinction between three types of day has been made in order to check the ranges of validity of the methods. In particular, it can be observed that Osterwald method is always the worst for any type of day. Moreover, it seems that the higher errors are associated with sunny days and partially cloudy day. This is related to the overestimation that all three methods make at higher irradiance. In fact, for cloudy day, when the irradiances are lower, all three methods seem to perform better.

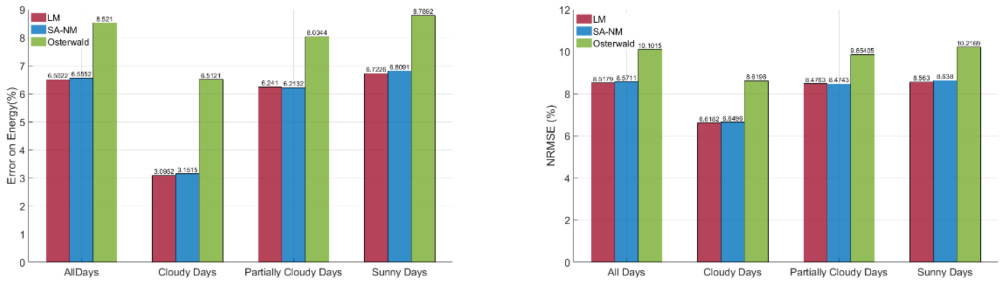

Figure 9-16: Error on estimated energy and NMRSE on maximum power for Sanyo HIT module.

9.2 CIGS thin film module

I. Parameters extraction

As mentioned in chapter 8.2, after the filtering procedure, only 907 curves were left and have been used to extract the parameter. Moreover, after the extraction, the set of parameters has been further filtered to remove those affected by overfitting. In particular the following filters have been applied:

- Series Resistance below 2 Ω and above 1.4 Ω.
- NRMSE below 0.02
- Error on Maximum Power below 2%.

In the end, the feasible parameters left were 629 for Levenberg-Marquardt algorithm and 633 for Simulated-Annealing and Nelder-Mead.

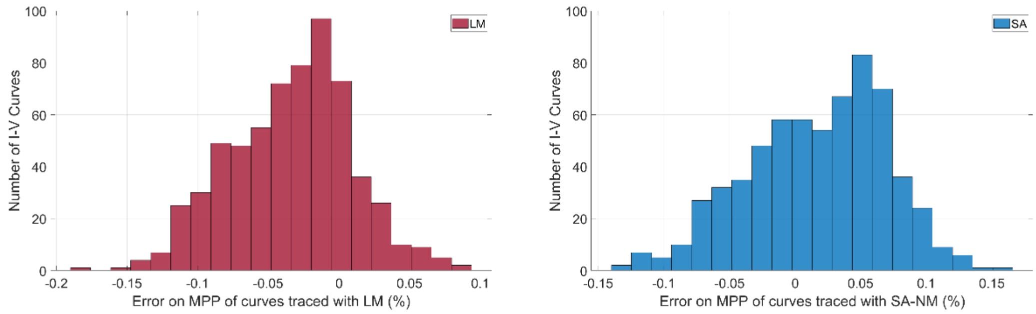

Figure 9-17: Error on Maximum Power of the fitting procedure for Avancis module.

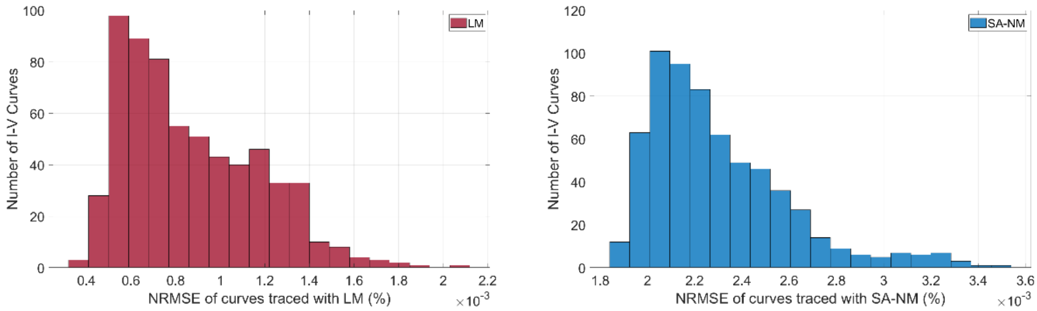

Figure 9-18: NRMSE of the fitting procedure for Avancis module.

Figures (9-17) and (9-18) show the density distribution of the NRMSE and of the error on maximum power point for the remaining curves. Once again both methods perform well, but Levenberg Marquardt performs slightly better and it's characterized by higher accuracy. In table (9-4), the average values of the NRMSE, error on maximum power point and fitting execution time are summarized. As previously stated, the NRMSE of LM is around 0.0008 whilst that of SA-NM is almost an order of magnitude higher, around 0.0023. However, by looking at the error on the maximum power, for LM it seems that is shifted more toward negative values, which means that the power is more often underestimated. For SA on the other hand, the average value is lower and shifted more toward positive values. Nonetheless, results are still good for both methods. The last comparison can be made considering the fitting execution time. In this sense SA-NM is once again characterized by the lower computational cost.

	Levenberg-Marquardt	*Simulated-Annealing & Nelder-Mead*
$NRMSE_{,avg}$ (-)	0.0008	0.0023
$ErrPmax_{,avg}$ (%)	-0.034	0.017
$FittingTime_{,avg}$ (s)	93.7	21.1

Table 9-4: Average parameters of the fitting procedure for Avancis module

In figure (9-19), the *I-V* curves at different values of irradiance and temperature are shown considering both the measured curves (the circles) and those estimated through the extracted parameter (line) with Levenberg-Marquardt algorithm. The two curves perfectly overlap each other at any value of irradiance and temperature, which means the applied procedure is able to accurately predict the shape of the *I-V* curve at any given condition. The same graph can be obtained also for the curves extracted through SA-NM method, but the results are exactly the same.

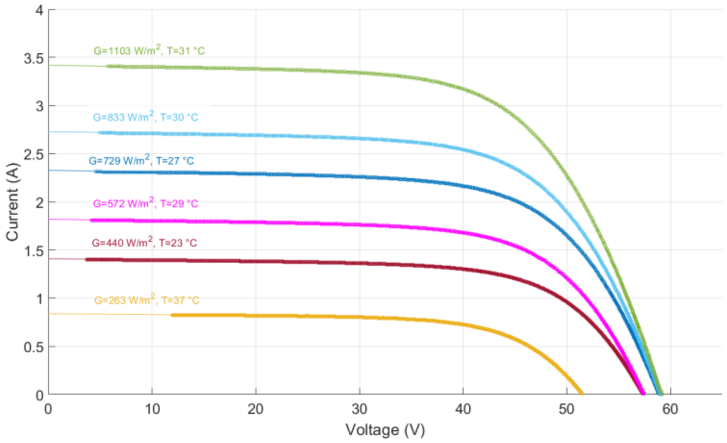

Figure 9-19: Measured (circles) and extracted *I-V* curves at different values of irradiance and temperature with LM algorithm for Avancis module

II. Parameters Equations

The results of the coefficients of the correlations obtained from the non-linear regressions are summarized in the following tables. Due to the high dispersion of the points in the available dataset, some correlations has been adjusted to properly fit the specific application. In particular, the series resistance has been considered constant at any given value of irradiance and temperature. The discussion of each correlation will be carried out in the following pages in more details.

	I_{ph} (A)	I_0 (A)	n (-)	R_s (Ω)	R_{sh} (Ω)
a	3.05	$5.27\ 10^{-6}$	1.83	0.17	376
b	0.00008	0.42	$1.37\ 10^{-4}$		
c		1.121	$-2.9\ 10^{-3}$		

Table 9-5: Coefficients of the proposed correlations with LM method for Avancis module

	I_{ph} (A)	I_0 (A)	n (-)	R_s (Ω)	R_{sh} (Ω)
a	3.05	$5.07\ 10^{-6}$	1.82	0.17	376
b	0.00008	0.43	$1.57\ 10^{-4}$		
c		1.121	$-2.8\ 10^{-3}$		

Table 9-6: Coefficients of the proposed correlations with SA-NM method for Avancis module

1. Photogenerated Current

The photogenerated current is linearly proportional to the irradiance, whilst is very disperse with respect to temperature. The final correlations are presented in equations (9-11) and (9-12). The result of the regression consists only on the value of the optimal a ($I_{ph,STC}$), as the temperature coefficient has been taken from the manufacturer datasheet and considered constant. The graphs which shows the correlations of the photogenerated current with respect to irradiance for LM and SA-NM method are shown in figure (9-20) and (9-21) respectively.

$$I_{ph} = \mathbf{3.05} \cdot [1 + 0.0008(T_c - T_{c,STC})] \cdot \frac{G}{G_{STC}} \tag{9-11}$$

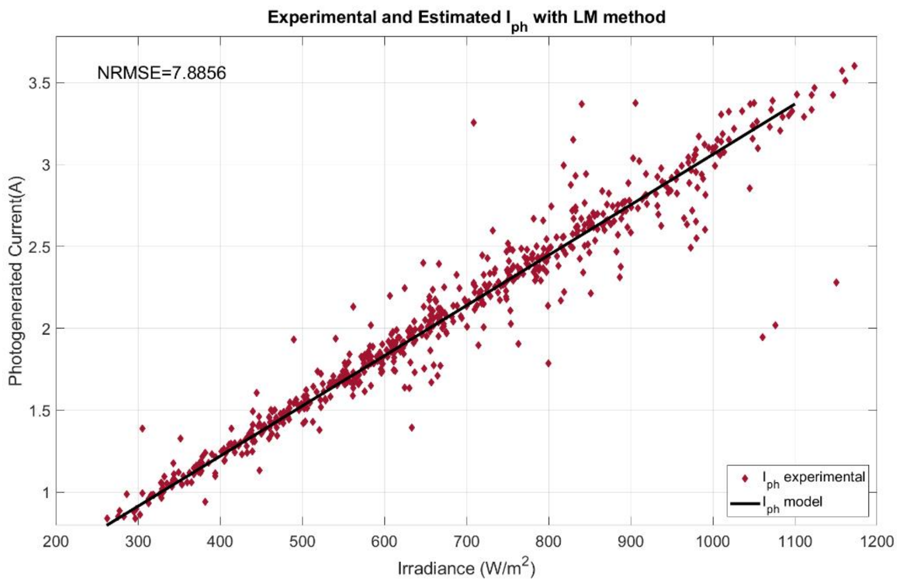

Figure 9-20: Results of the non-linear regression for the photogenerated current estimated with LM method for Avancis module.

$$I_{ph} = \mathbf{3.05} \cdot [1 + 0.0008(T_c - T_{c,STC})] \cdot \frac{G}{G_{STC}} \tag{9-12}$$

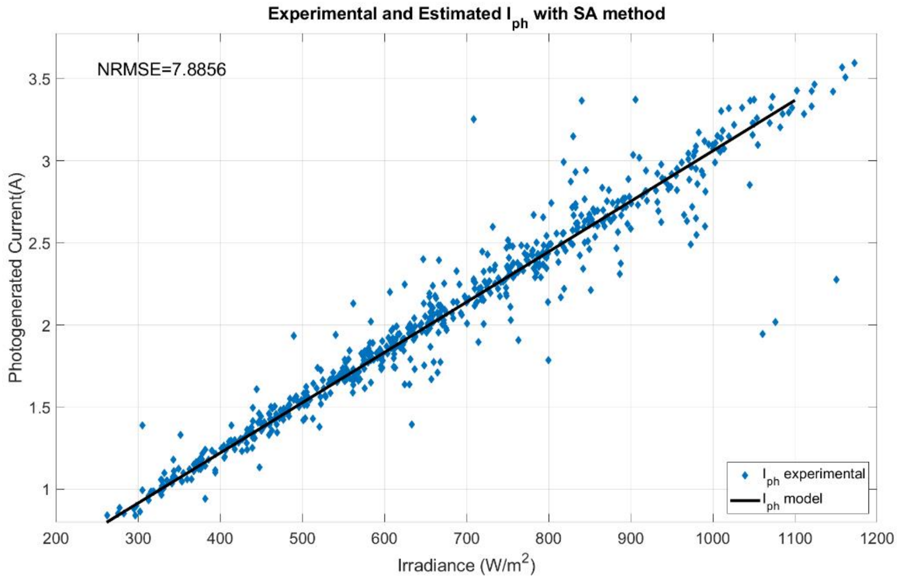

Figure 9-21: Results of the non-linear regression for the photogenerated current estimated with SA-NM for Avancis module.

Compared to the previous module, the experimental points present a higher level of dispersion. For this reason, both methods are characterized by a higher NRMSE, around 7.89 % both for LM and SA-NM. Nonetheless, the correlations are still able to predict the behaviour of the photogenerated current as there is an overall trend that is increasing with irradiance.

2. Saturation Current

The saturation current presents a higher level of dispersion compared to the previous module as well. But there is still a visible trend increasing with temperature. Considering the correlation presented in chapter 6, precisely the corrected formulation for non-monocrystalline modules, the non-linear regression is applied to the values of a ($I_{0,STC}$) and b (χ).

Moreover, the equations that describes the two models are (9-13) and (9-14), represented in figure (9-22) and (9-23) for LM and SA-NM respectively.

$$I_0 = \mathbf{5.27\ 10^{-6}} \cdot \left(\frac{T_c}{T_{c,STC}}\right)^3 \cdot e^{\mathbf{0.42} \cdot \left(\frac{E_{g,STC}}{T_{STC}} - \frac{E_g(T_c)}{T_c}\right) \cdot \frac{1}{k_b}} \tag{9-13}$$

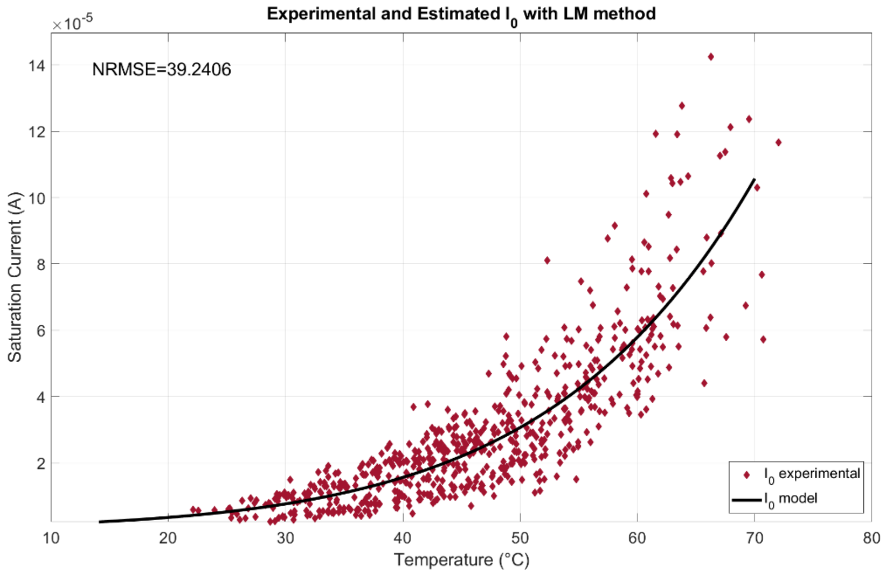

Figure 9-22: Results of the non-linear regression for the saturation current estimated with LM method for Avancis module.

$$I_0 = \mathbf{5.07\ 10^{-6}} \cdot \left(\frac{T_c}{T_{c,STC}}\right)^3 \cdot e^{\mathbf{0.43} \cdot \left(\frac{E_{g,STC}}{T_{STC}} - \frac{E_g(T_c)}{T_c}\right) \cdot \frac{1}{k_b}} \tag{9-14}$$

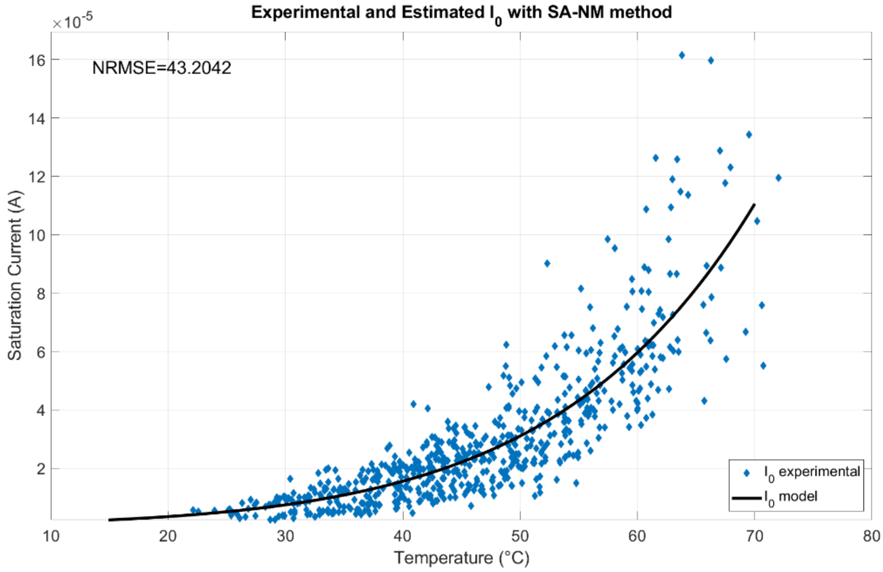

Figure 9-23: Results of the non-linear regression for the saturation current estimated with SA-NM method for Avancis module.

As expected by the higher dispersion, the NRMSE associated to both correlations is relatively high, around 39.24% for LM and 43.2% for SA-NM. The correlation obtained for the LM model performs slightly better, but the error is still very high for both.

3. Diode Ideality Factor

The results for both LM and SA-NM method are shown below both in graphical and mathematical form. The regression has been performed on the a, b and c.

$$n = \mathbf{1.83} + \mathbf{1.37\ 10^{-4}} \cdot G - \mathbf{2.91\ 10^{-3}} \cdot T_c \tag{9-15}$$

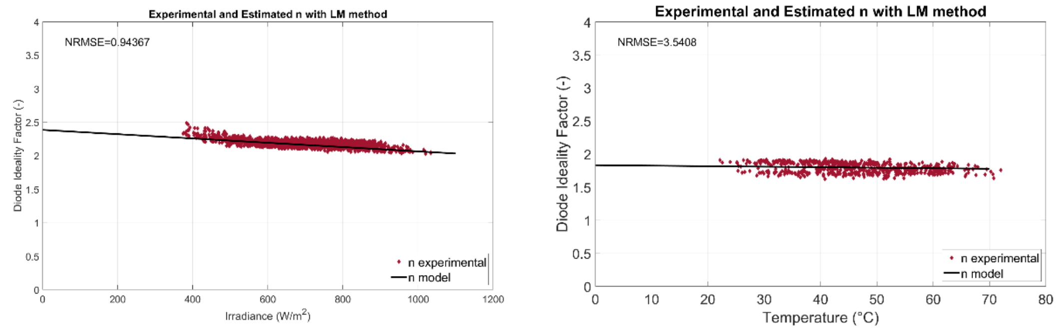

Figure 9-24: Results of the non-linear regression for the diode ideality factor estimated with LM method for Avancis module.

$$n = \mathbf{1.82} + \mathbf{1.57\ 10^{-4}} \cdot G - \mathbf{2.83\ 10^{-3}} \cdot T_c \tag{9-16}$$

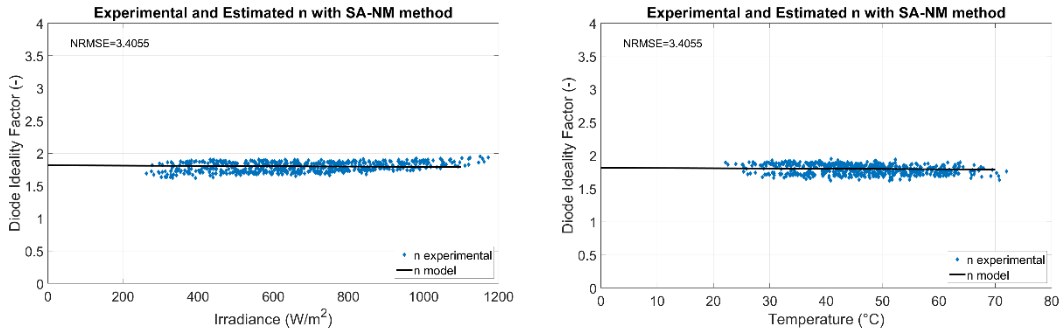

Figure 9-25: Results of the non-linear regression for the diode ideality factor estimated with SA-NM method for Avancis module.

For this module, the behaviour of the diode ideality factor with respect to irradiance and temperature is more constant, around 1.8. In fact, for both correlations the temperature and irradiance coefficients are very low. Nonetheless, it seems that the correlations can closely approximate the behaviour of the diode ideality factor since the NRMSE is relatively low. In fact, its value is 3.54 for LM and 3.4 for SA-NM, which means that for this parameter the correlation obtained with SA-NM is more accurate.

4. Series Resistance

The series resistance presents a high dispersion of points and no clear tendency that follow the correlation presented in chapter 6. For this reason, it has been decided to consider the series resistance constant across the whole range of irradiance and temperature since it was the best solution to reduce the error associated with the correlations. Its value has been imposed to 1.7 for both methods after looking at the distribution of experimental points. In the graphs below, the results are presented for both method as a function of irradiance in order to show the higher dispersion of the experimental points.

For this reason, considering the high dispersion of the points, the NRMSE is still within acceptable ranges since it's around 8.22 and 7.98 for LM and SA-NM respectively.

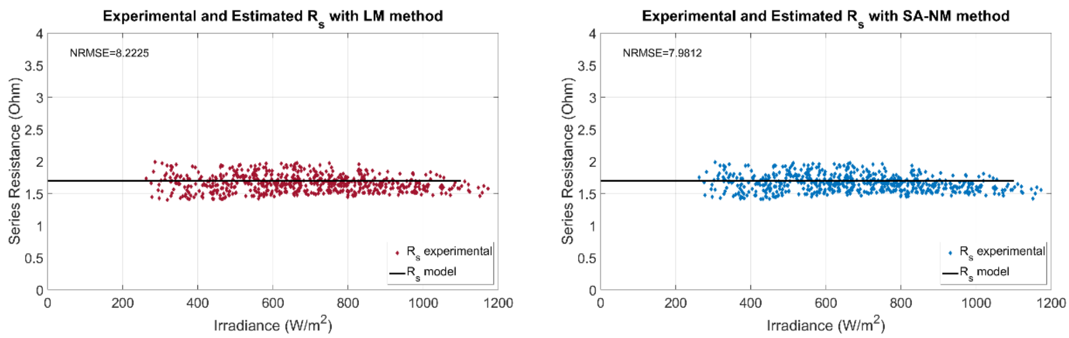

Figure 9-26:Dependence of series resistance with respect to irradiance estimated with LM and SA-NM method for Avancis module.

5. Shunt Resistance

The shunt resistance presents a very disperse behaviour both with irradiance and temperature. Nonetheless, the non-linear regression has been applied anyway to find the correlations by optimizing a $(R_{sh,STC})$. The final results are the same for both methods but due to the high dispersion of the points it has been decided to not include the graphical representation has no clear tendency was observable. The equations describing the behaviour of the shunt resistance is presented below.

$$R_{sh} = \mathbf{375.8} \cdot \frac{G_{STC}}{G} \tag{9-17}$$

$$R_{sh} = 375.8 \cdot \frac{G_{STC}}{G} \tag{9-18}$$

Due to the high dispersion of the points, the NRMSE of both correlations is very high. Still, the one with the LM method is slightly better, being 34.54% compared to the 36.29% of the one with SA-NM.

Figure (9-27) shows the normal root mean square error associated with each correlation. As mentioned before, even though the SA-NM method had a slightly lower NRMSE for the series resistance and the diode ideality factor, the LM performs better overall. In fact, regarding the saturation current and the shunt resistance, which are the parameters affected by the higher error, LM method is able to provide correlation with better accuracy.

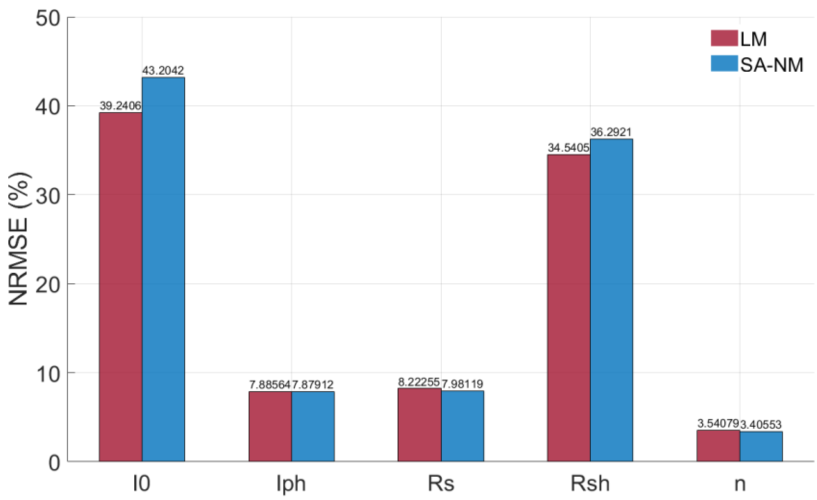

Figure 9-27: NRMSE of each parameters correlation for Avancis module

Lastly, in figure (9-28) the same curves presented in figure (9-19) are shown, comparing the measured curves with those estimated through the use of the correlations and of the transcendental equation. As expected, the results are not as accurate as they were in figure (9-19) since the parameter estimated through the correlations are affected by a lower level of accuracy. This seem to be the case especially for lower irradiances, when the estimated optimal power point is further from the experimental one.

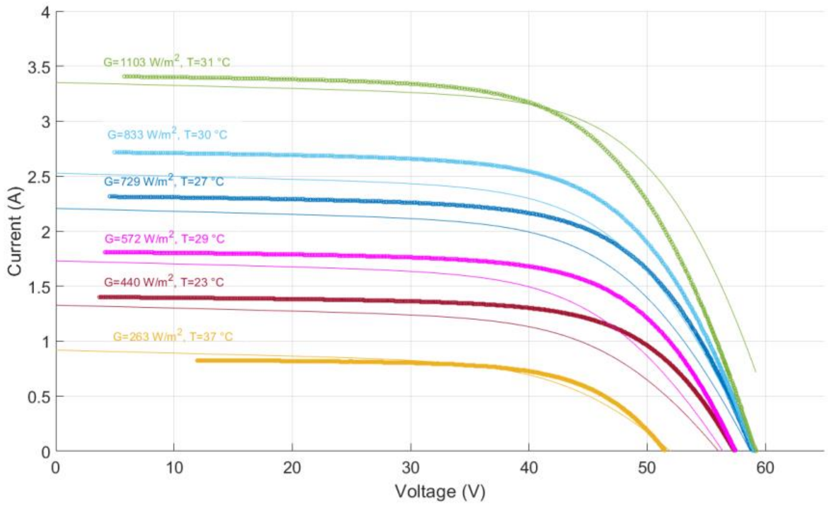

Figure 9-28: Measured (circles) and modelled *I-V* curves at different values of irradiance and temperature with LM correlations for Avancis module

III. Power and Energy estimation

The last step of the analysis consists in the power and energy estimation to compare the three methods: LM, SA-NM and Osterwald. Despite the high NRMSE associated to the correlations, it seems that they perform well to estimate the maximum power.

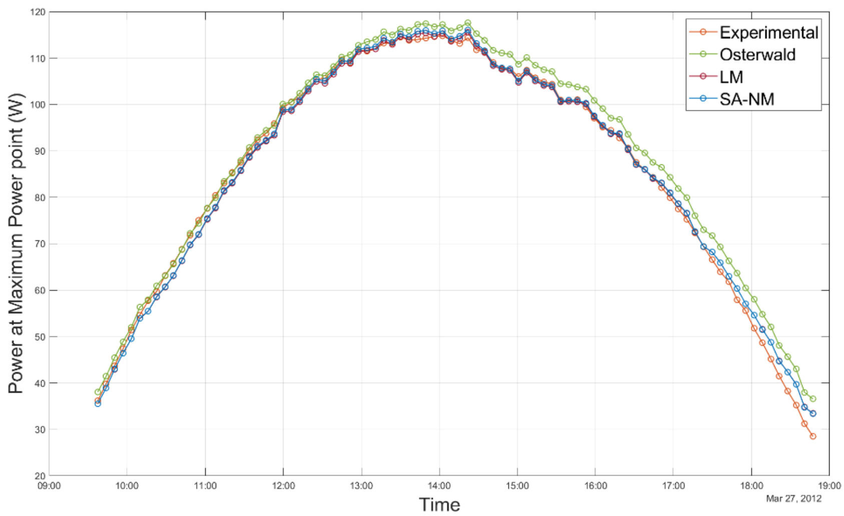

Figure 9-29: Power at Maximum Power Point for a given day for Avancis module

Figure (9-29) shows the daily evolution of power considering both the experimental values and those estimated with the three models. In particular, it seems that both LM and SA-NM are able to closely approximate the experimental curve, which means that the power is estimated with a high level of accuracy for both higher and lower levels of irradiance. Osterwald method on the other hand, is often overestimating the power, especially after the morning hours.

A more detailed analysis considering all the available measure in dataset can be performed on each applied model to compare the estimated results with the experimental ones. Figure (9-30) shows the power with LM (red) and SA-NM (blue). In both figures it’s possible to notice that the models accurately follow the experimental behaviour for any value of irradiance and temperature. Osterwald method (green) on the other hand, slightly overestimate the experimental values, which results in a higher error.

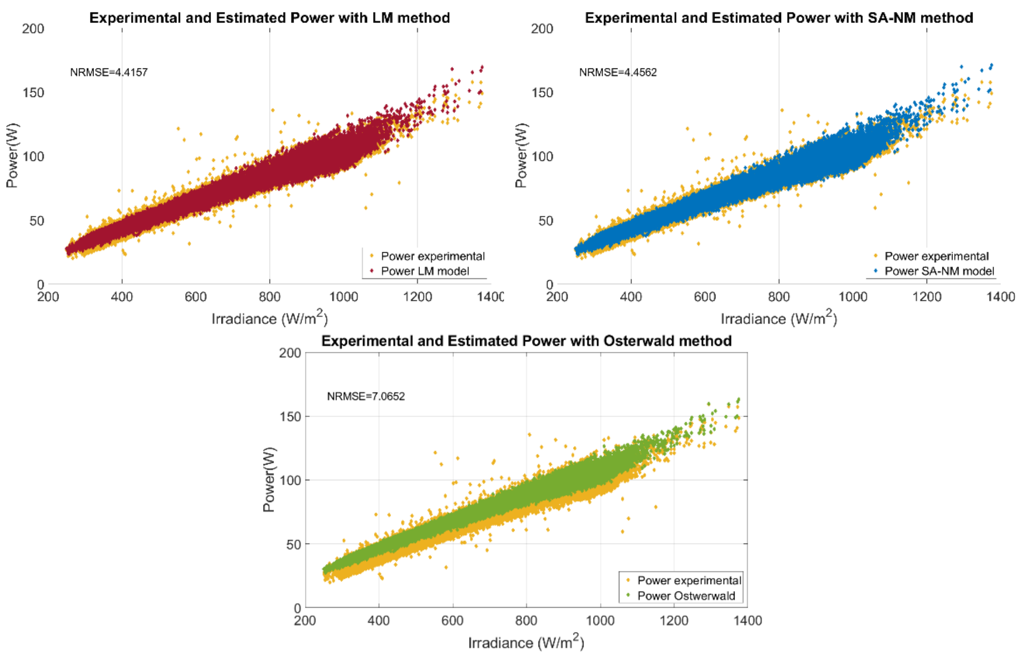

Figure 9-30: Comparison of power at MPP between experimental points and those estimated with the various method for Sanyo HIT module

Finally to compare the three methods, it’s possible to compute the error on the estimation of energy and the NRMSE on the estimation of maximum power. The results are shown in figure (9-31). It’s clear that the models developed with the innovative technique presented in this study are characterized by a higher accuracy since both errors are lower than Osterwald. In particular, the error on the estimated energy is less than half compared to Osterwald, even though this could also be linked to the error compensation related to the change of sign. However, the NRMSE on the power still presents a high difference, which further proves the goodness of the experimental models extracted.

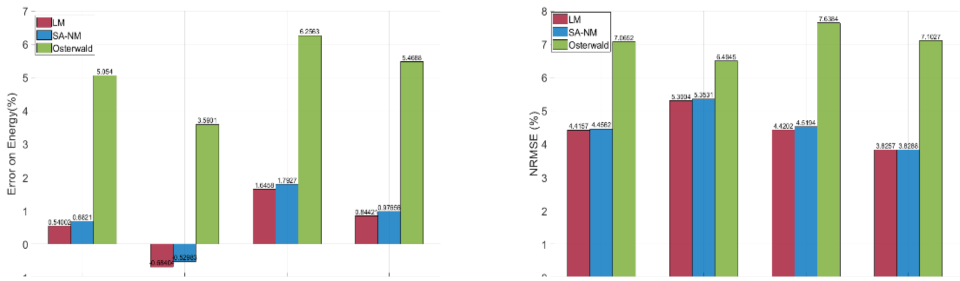

Figure 9-31: Error on estimated energy and NMRSE on maximum power for Avancis module.

Moreover, considering the NRMSE, it's important to notice that the error associated to the experimental models is higher for cloudy days and decreases for partially and sunny days. This means that the models are able to work with higher accuracy for the days characterized by overall clear sky conditions. On the contrary, Osterwald model has the opposite behaviour and works better for cloudy days.

9.3 CdTe thin film module

For the First Solar module, the parameters of the 9373 curves used to perform the parameter extraction procedure have been filtered as follow:

- Manuel filter on series resistance, shunt resistance and saturation current
- NRMSE below 0.015
- Error on Maximum Power below 2%.

In particular, the manual filter consists in a series of iterations in which the correlations obtained from the non-linear regression are used to filter out the points that do not follow the tendency. At first the non-linear regression is applied to the complete set of parameters, then at each iteration is applied to the filtered parameters to obtain new correlations that are used to perform a new filtering. The value of the tolerance associated to each error has been chosen arbitrary at each iteration by looking at the distribution of the error between the estimated and experimental value of the before mentioned parameters. Moreover, after four iterations it has been decided to stop the filtering procedure in in order to not reduce too much the available dataset. In the end, the feasible parameters left were 2023 for Levenberg-Marquardt and 2041 for Simulated-Annealing and Nelder-Mead.

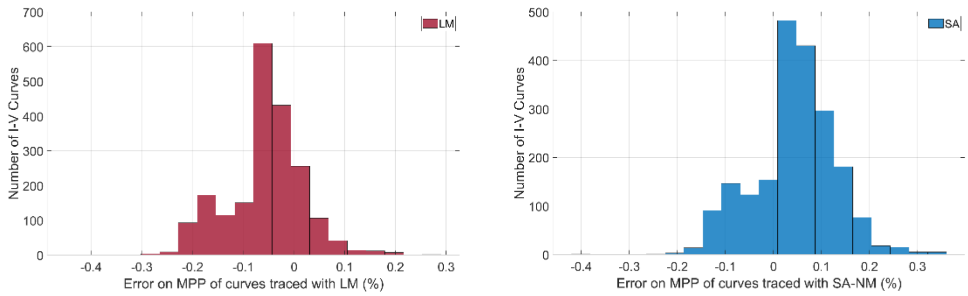

Figure 9-32: Error on Maximum Power of the fitting procedure for First Solar module.

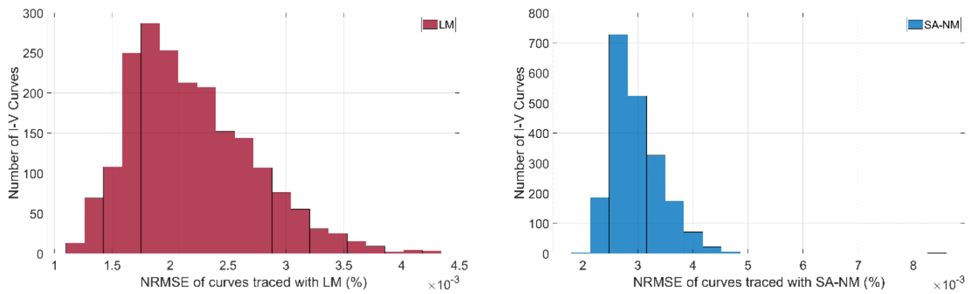

Figure 9-33: NRMSE of the fitting procedure for First Solar module.

In figure (9-32) and (9-33) the density distribution of the NRMSE and of the error on maximum power point for the remaining curves is presented. Once again it seems that Levenberg-Marquardt algorithm performs slightly better in terms of accuracy. In this sense, table (9-7) summarize the main average specifications associated to the two algorithms. Contrary to what happen for the other modules, it seems that the Levenberg-Marquardt algorithm is not only characterized by a higher accuracy, but also by a lower computational cost.

	Levenberg-Marquardt	*Simulated-Annealing & Nelder-Mead*
$NRMSE_{,avg}$ (-)	0.0022	0.0030
$ErrPmax_{,avg}$ (%)	-0.0564	0.0442
$FittingTime_{,avg}$ (s)	10.020	14.360

Table 9-7: Average parameters of the fitting procedure for First Solar module

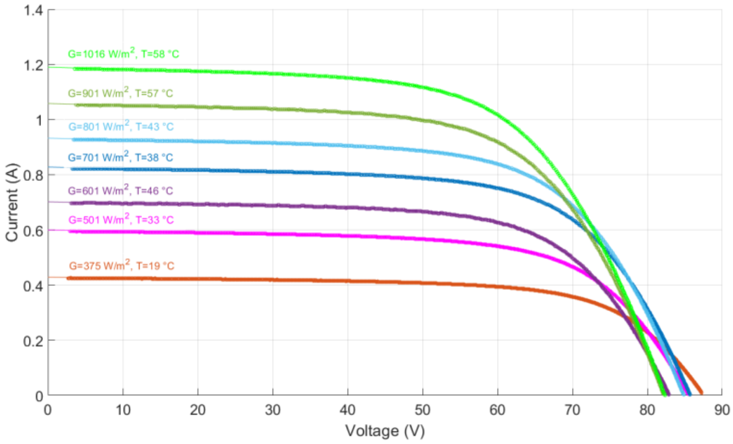

Figure 9-34: Measured (circles) and extracted *I-V* curves at different values of irradiance and temperature with LM algorithm for First Solar module.

In figure (9-34), the curves estimated using the parameters from the fitting procedure are compared with the experimental ones. It's clear that the method is able to accurately predict the shape of the *I-V* curve at any value of irradiance. The graph is only related to the parameters extracted with Levenberg-Marquardt algorithm, but the exact same observation can be made for those obtained with Simulated-Annealing and Nelder-Mead.

I. Parameters Correlations

The filtered set of parameters has been used to extract the final correlations. Similarly to what has been done for the other modules, a non-linear regression has been applied to the correlations discussed in chapter 6. The results of the coefficients of the correlations obtained from the non-linear regressions are summarized in the following tables, both for LM and SA-NM.

	I_{ph} (A)	I_0 (A)	n (-)	R_s (Ω)	R_{sh} (Ω)
a	1.17	$1.45\ 10^{-6}$	2.38	6.2	1194
b	0.0004	0.28	$9.3\ 10^{-5}$	0.26	
c		1.121	$-6.5\ 10^{-4}$		

Table 9-8: Coefficients of the proposed correlations with LM method for First Solar module

	I_{ph} (A)	I_0 (A)	n (-)	R_s (Ω)	R_{sh} (Ω)
a	1.17	1.09 10^{-6}	2.32	6.24	1165
b	0.0004	0.33	9.66 10^{-5}	0.33	
c		1.121	-5.53 10^{-4}		

Table 9-9: Coefficients of the proposed correlations with SA-NM method for First Solar module

Moreover, each correlation will be discussed in more details in the following pages. In particular, a distinction between each parameter and the methods applied has been made to compare them in term of accuracy.

1. Photogenerated Equations

The correlation for the photogenerated current has been obtained by optimizing the value of ‘a’ ($I_{ph,STC}$) in the equation presented in chapter 6. The graphs which shows the correlations of the photogenerated current with respect to irradiance for LM and SA-NM method are shown in figure (9-35) and (9-36) respectively.

$$I_{ph} = \mathbf{1.17} \cdot [1 + 0.0004(T_c - T_{c,STC})] \cdot \frac{G}{G_{STC}} \tag{9-19}$$

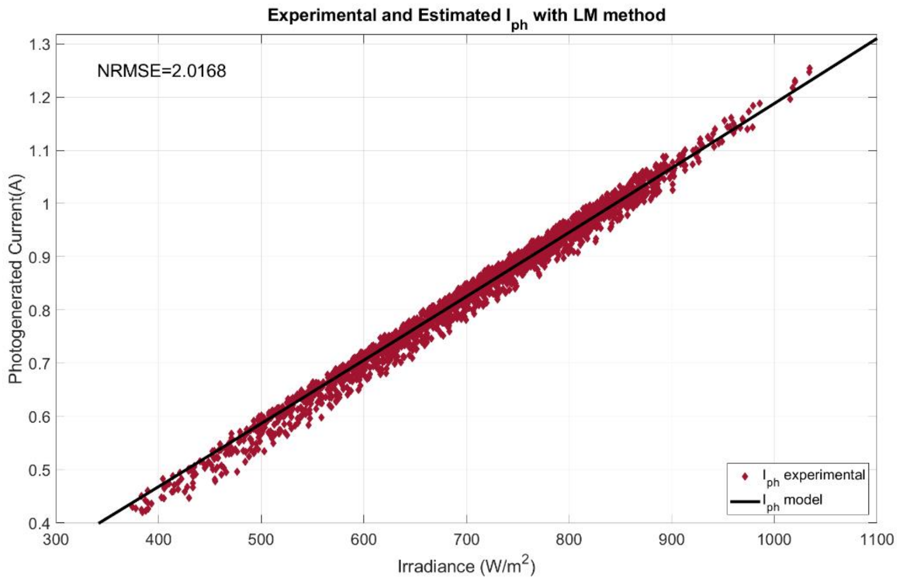

Figure 9-35: Results of the non-linear regression for the photogenerated current estimated with LM method for First Solar module.

$$I_{ph} = \mathbf{1.17} \cdot [1 + 0.0004(T_c - T_{c,STC})] \cdot \frac{G}{G_{STC}} \tag{9-20}$$

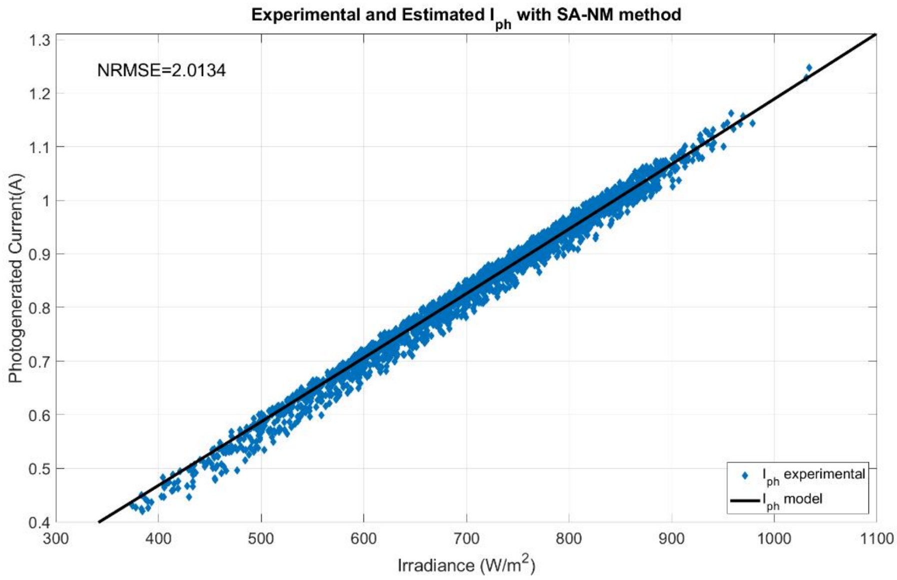

Figure 9-36: Results of the non-linear regression for the photogenerated current estimated with SA-NM for First Solar module.

Compared to the other two modules on which this procedure has been applied, the dataset available for the First Solar module was larger, therefore some parameters are characterized by a higher dispersion. Nonetheless, with both methods the NRMSE is still very low, around 2.02% for LM and 2.01% for SA-NM. This means that the correlations are able to accurately predict the behaviour of the photogenerated current.

2. Saturation Current

Once again, the saturation current presents a behaviour that is strictly related to the temperature and not so much to the irradiance. For this reason equation (6-5) can be used to fit this tendency. In particular, since this module is made of non-monocrystalline materials, the parameters optimized in the non-linear regressions are ‘a’ ($I_{0,STC}$) and ‘b’ (χ).

The correlations obtained for the two methods are shown in the following figures. In particular, equation (9-21) and figure (9-37) show the results with LM method, whilst equation (9-22) and figure (9-38) show the results with SA-NM.

$$I_0 = \mathbf{1.45\ 10^{-6}} \cdot \left(\frac{T_c}{T_{c,STC}}\right)^3 \cdot e^{\mathbf{0.28} \cdot \left(\frac{E_{g,STC}}{T_{STC}} - \frac{E_g(T_c)}{T_c}\right) \cdot \frac{1}{k_b}} \tag{9-21}$$

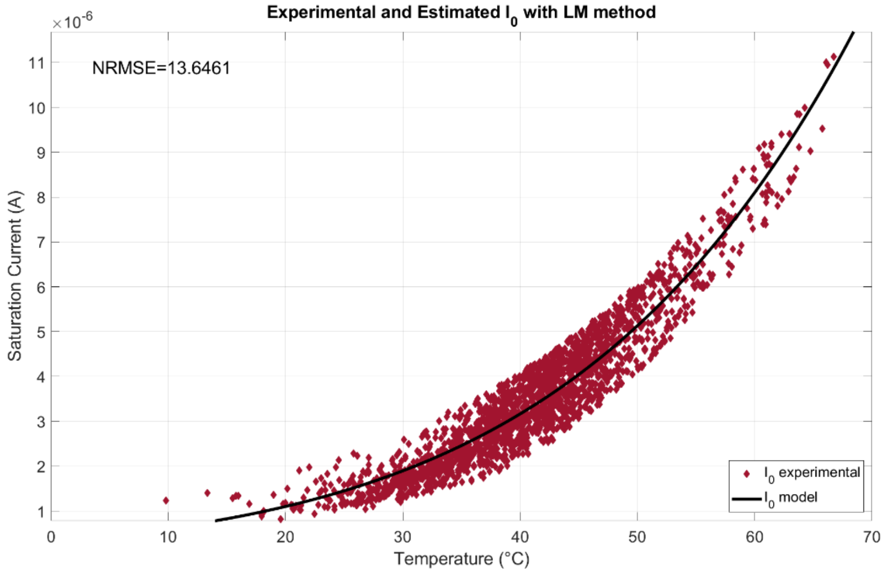

Figure 9-37: Results of the non-linear regression for the saturation current estimated with LM method for First Solar module.

$$I_0 = \mathbf{1.09\ 10^{-6}} \cdot \left(\frac{T_c}{T_{c,STC}}\right)^3 \cdot e^{\mathbf{0.33} \cdot \left(\frac{E_{g,STC}}{T_{STC}} - \frac{E_g(T_c)}{T_c}\right) \cdot \frac{1}{k_b}} \tag{9-22}$$

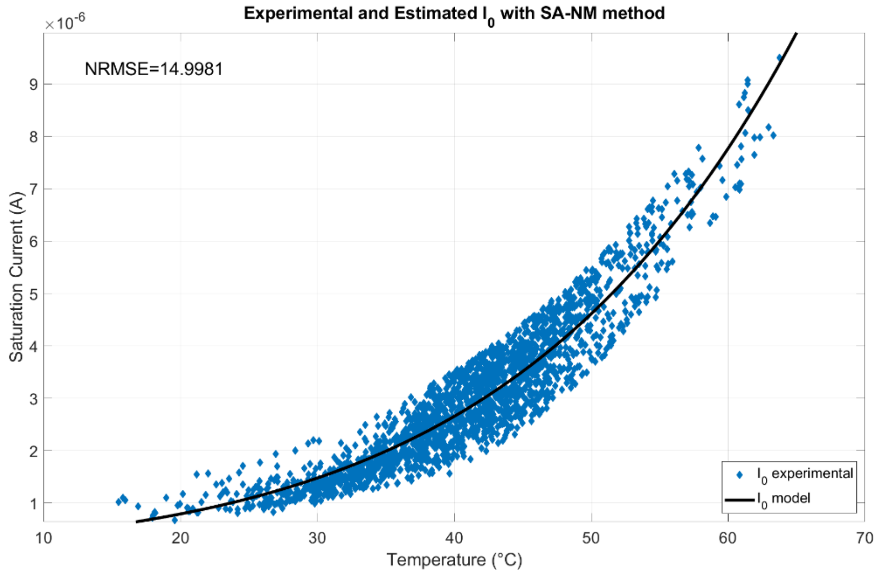

Figure 9-38: Results of the non-linear regression for the saturation current estimated with SA-NM method for First Solar module.

The trends follow closely the behaviour of the experimental points even if some dispersion is still observable. Nonetheless, the NRMSE associated to both correlations is relatively low, around 13.65% for LM and 15% for SA-NM. This means that the correlation obtained for LM model is slightly better.

3. Diode Ideality Factor

The diode ideality factor presents a tendency that seems to be related more to temperature that to irradiance. Moreover, it seems that n decreases with temperature and irradiance, even though the behaviour with irradiance seems almost constant besides for lower and higher values. Considering the linear correlation presented in chapter 6, the optimization has been performed on the values of a, b and c of equation (6-7). The results for both LM and SA-NM method are shown below both in graphical and mathematical form in the following figures and equations.

$$n = \mathbf{2.384} + \mathbf{9.30\ 10^{-5}} \cdot G - \mathbf{6.5\ 10^{-3}} \cdot T_c \tag{9-23}$$

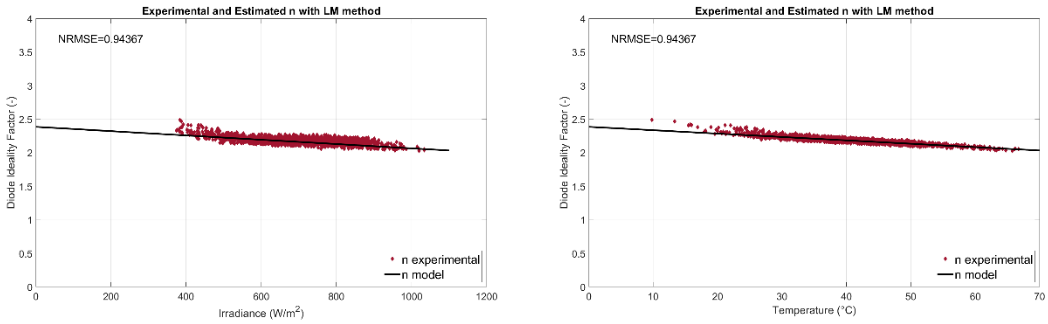

Figure 9-39: Results of the non-linear regression for the diode ideality factor estimated with LM method for First Solar module.

$$n = \mathbf{2.32} + \mathbf{9.66\ 10^{-5}} \cdot G - \mathbf{5.53\ 10^{-3}} \cdot T_c \tag{9-24}$$

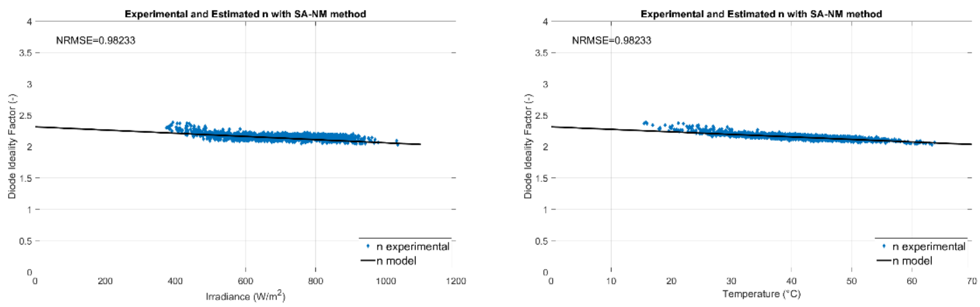

Figure 9-40: Results of the non-linear regression for the diode ideality factor estimated with SA-NM method for First Solar module.

Once again, the correlations can closely approximate the behaviour of the diode ideality factor. In fact, with both method the NRMSE is below one, being slightly better for LM.

4. Series Resistance

The series resistance presents a high dispersion. Nonetheless, a clear tendency was still observable with respect to irradiance and temperature. For this reason , the non-linear regression has been applied to optimize the coefficients 'a' ($R_{s,STC}$) and 'b' (λ_{R_s}) of equation (6-8). In particular, it seems that the series resistance decreases with irradiance while it has a more disperse behaviour with respect to temperature. The equations modelling the two correlations for the two methods are (9.25) and (9.26), for LM and SA-NM respectively. Furthermore, in the graphs below, the results of the non-linear regression are presented with respect to irradiance.

$$R_s = \mathbf{6.205} \cdot \frac{T_c}{T_{c,STC}} \cdot \left[1 - \mathbf{0.259} \cdot log\left(\frac{G}{G_{STC}}\right)\right] \tag{9-25}$$

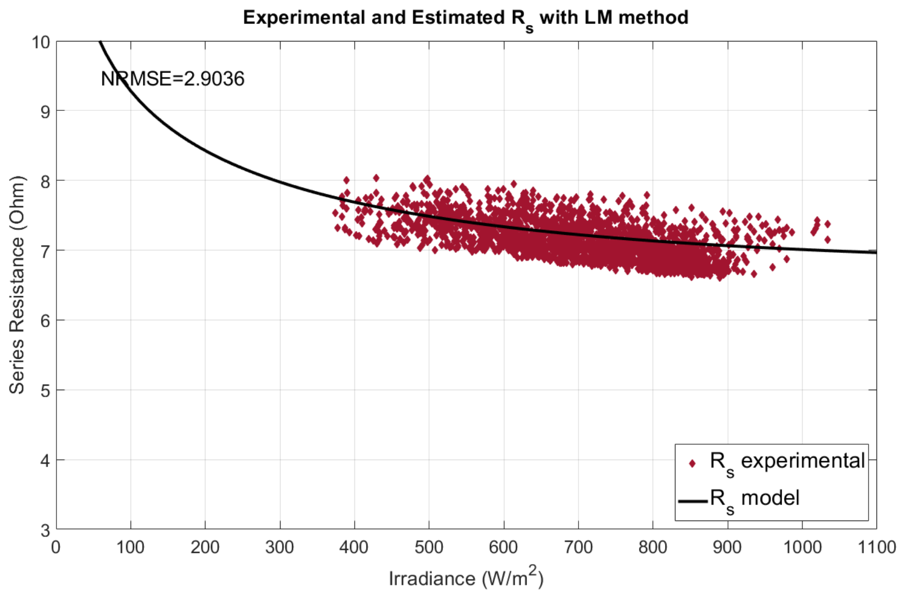

Figure 9-41: Results of the non-linear regression for the series resistance estimated with LM method for First Solar module.

$$R_s = \mathbf{6.239} \cdot \frac{T_c}{T_{c,STC}} \cdot \left[1 - \mathbf{0.325} \cdot log\left(\frac{G}{G_{STC}}\right)\right] \tag{9-26}$$

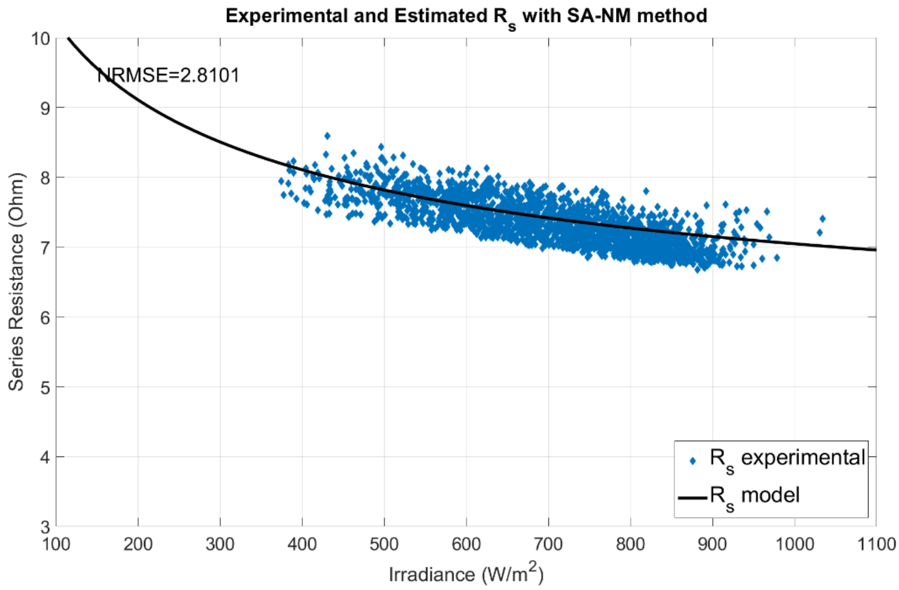

Figure 9-42: Results of the non-linear regression for the series resistance estimated with SA-NM method for First Solar module.

Looking at the correlations obtained with both methods, it seems that the series resistance has similar tendencies with both irradiance and temperature. In fact, the parameter λ_{R_s} is positive since the series resistance decreases with irradiance and temperature. Moreover, as expected, the values of the series resistance are between 7 and 9, which is significantly higher compared to the other modules. However, these are the typical values for these kinds of technologies since they are often associated with higher losses through the frontal contact.

Lastly, regarding the NRMSE on the correlation, its value is 2.9 % for LM and 2.8 % for SA-NM, which means that the correlations achieved with SA-NM are able to accurately predict the behaviour of the parameters.

5. Shunt Resistance

The shunt resistance presents a very clear behaviour with irradiance whilst is a bit disperse with respect to temperature. This confirms the expected behaviour provided by the correlation, which is only function of irradiance and not of the temperature of the module. Moreover, regarding the non-linear regression on the correlation, the parameter that has been optimized to properly fit the experimental points was $R_{sh,STC}$. The graphical and mathematical representation of the correlations implemented with the two methods is presented below.

$$R_{sh} = \mathbf{1194.2} \cdot \frac{G_{STC}}{G} \tag{9-27}$$

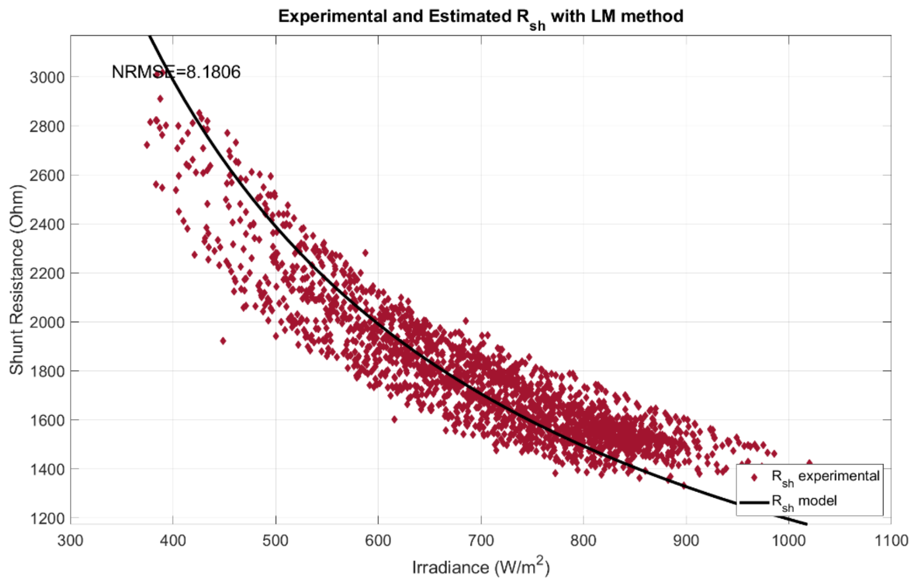

Figure 9-43: Results of the non-linear regression for the shunt resistance estimated with LM method for First Solar module.

$$R_{sh} = \mathbf{1165.4} \cdot \frac{G_{STC}}{G} \tag{9-28}$$

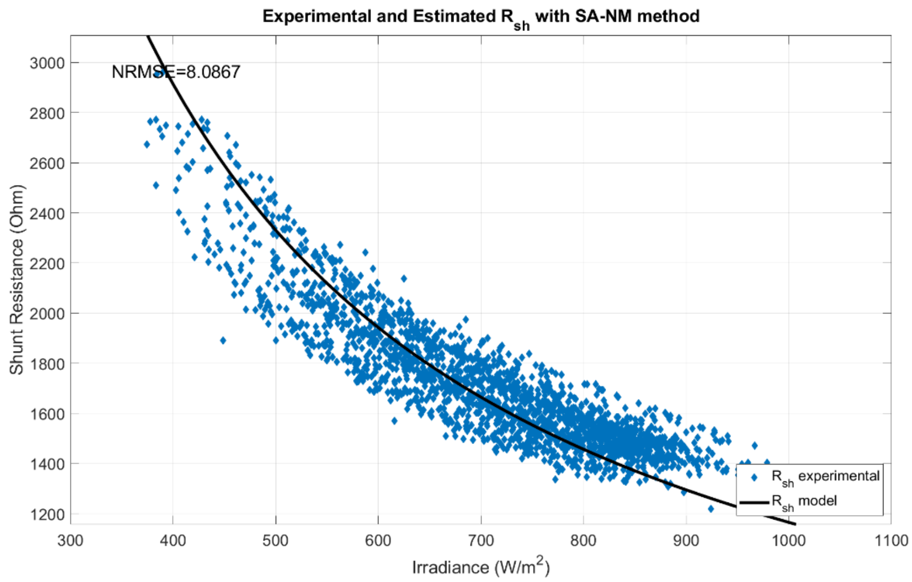

Figure 9-44: Results of the non-linear regression for the shunt resistance estimated with SA-NM method for First Solar module.

Due to the lower dispersion of the points compared to the other modules, the NRMS of both correlations is relatively low. In particular, that associated with SA-NM is 8.09 whilst that associated with LM is 8.18.

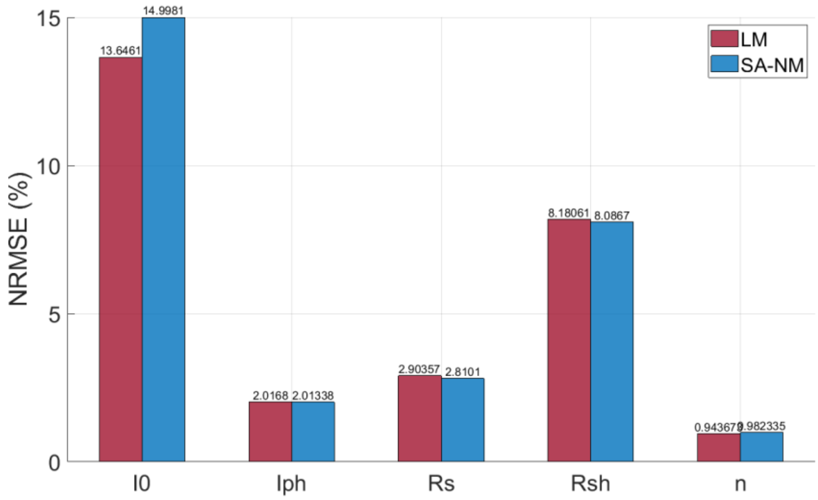

Figure 9-45: NRMSE of each parameter's correlation for First Solar module

In figure (9-45) the normal root mean square error associated with each correlations has been summarized. As mentioned before, the LM method is able to provide correlation with higher accuracy for the saturation current and diode ideality factor. Instead, for the other parameters SA-NM performed better. In spite of this, it's important to note that both methods work well and are characterized by great accuracy. To study further the 'goodness' of each method, the analysis on energy and power estimation has been performed.

Figure (9-46) presents the same curves shown in figure (9-34) are shown, comparing the measured curves with those estimated through the use of the correlations and of the transcendental equation. Once again the results are not as accurate as they were in figure (9-34) since the parameters associated to each curve are no longer those optimized precisely to approximate that shape. Nonetheless, the curve estimated through the correlation are still accurate.

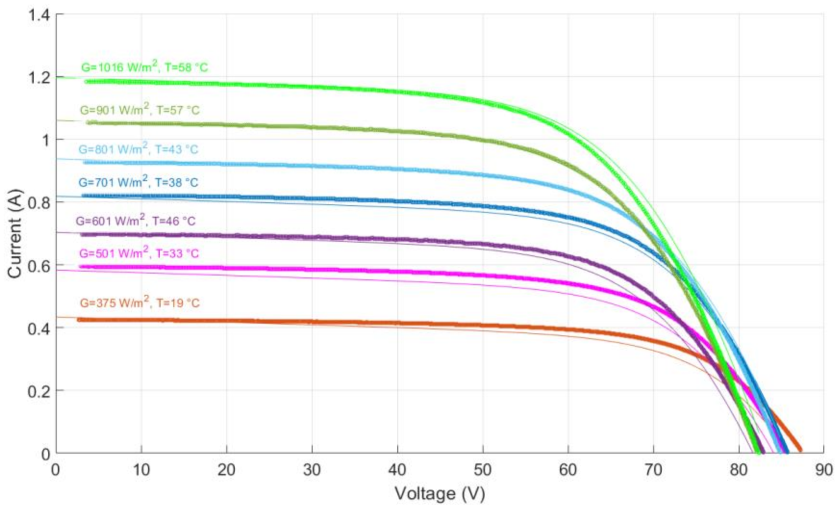

Figure 9-46: Measured (circles) and modelled *I-V* curves at different values of irradiance and temperature with LM correlations for First Solar module

II. Power and Energy estimation

The estimation of power and energy has been implemented in order to compare the three different method mentioned in chapter 8: LM, SA-NM and Osterwald. Firstly, it's possible to observe the typical power evolution for a typical sunny day considering both the experimental and the estimated values.

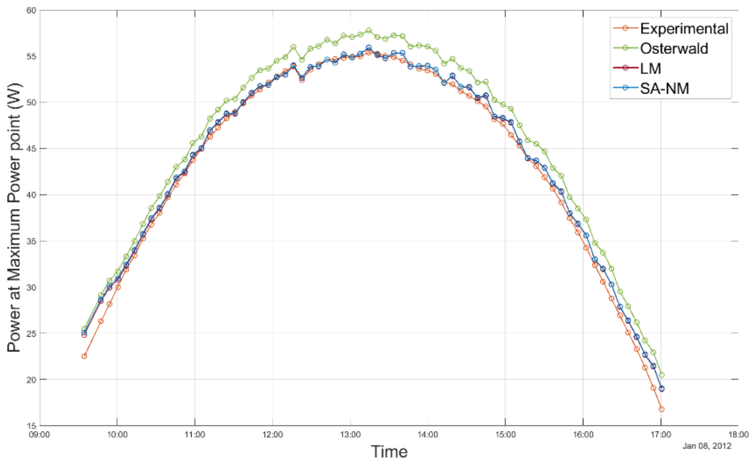

Figure 9-47: Power at Maximum Power Point for a given day for First Solar module

As shown in figure (9-47), LM and SA-NM models overlap each other perfectly. Moreover, they are very close to each other and are able to follow with great accuracy the real evolution of the experimental measured. Osterwald method on the other end is often overestimating the power, especially after the morning when the irradiance and temperature measure start to increase.

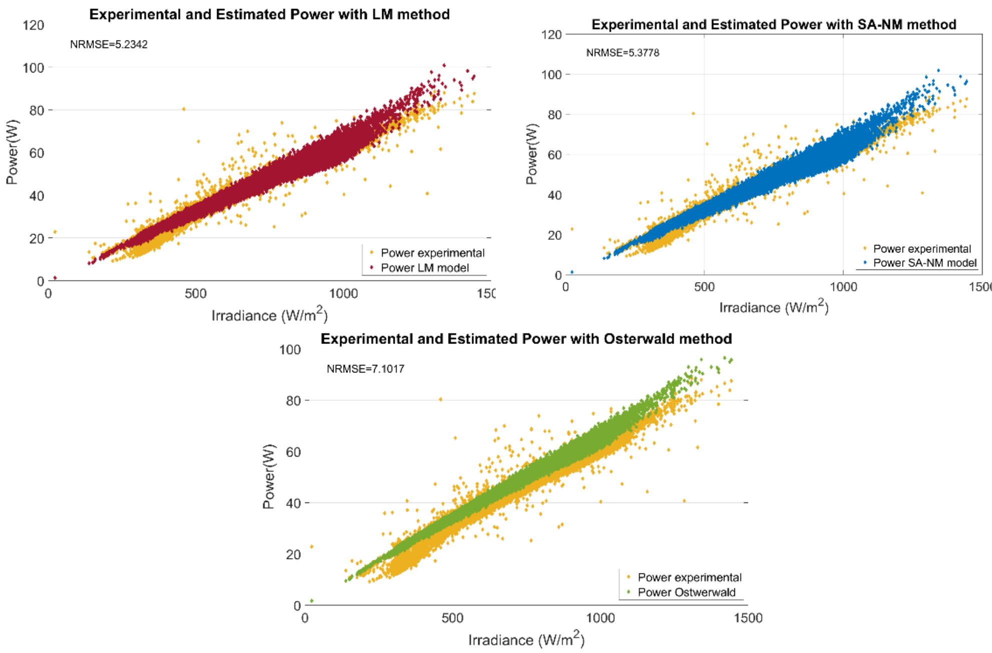

Figure 9-48: Comparison of power at MPP between experimental points and those estimated with the various method for First Solar module

A second analysis can be done considering the whole data-set available. For each method applied is possible to compare the experimental points with those estimated. Figure (9-48) shows the distribution of the experimental ad estimated points as a function of irradiance for all three methods. LM and SA-NM perform similarly, as they seem to approximate well the experimental data for irradiances higher that 500 W/m^2. For irradiances lower that 500 W/m^2 both methods overestimate the measures. Osterwald method on the other hand, overestimate the power at any value of irradiance.

Lastly, to better compare the three methods, it's possible to compute the error on the estimation of energy and the NRMSE on the estimation of maximum power. The results are shown in figure (9-49). Considering only the results related to all the data, it's obvious that the two methods developed with the innovative technique presented in this thesis are very good. In fact, when compared to Osterwald method, they are able to predict with more accuracy power and energy. Moreover, when looking at the distinction between, it can be observed that Osterwald method is always the worst for any type of day. In addition, considering the NRMSE on power estimation it seems that all three methods perform best for sunny-days and worst for cloudy-days. On the other hand, considering the error on energy estimation, which is affected by some error compensation between positive and negative values, it seems that Osterwald performs best for cloudy days and worst for sunny days. LM and SA-NM have lower errors for cloudy days as well. However, this could be simply related to the fact that for cloudy days, which are usually characterized by lower irradiances, the methods sometimes underestimate the experimental values causing error compensation. Instead for sunny and cloudy day, all three methods usually perform some overestimation.

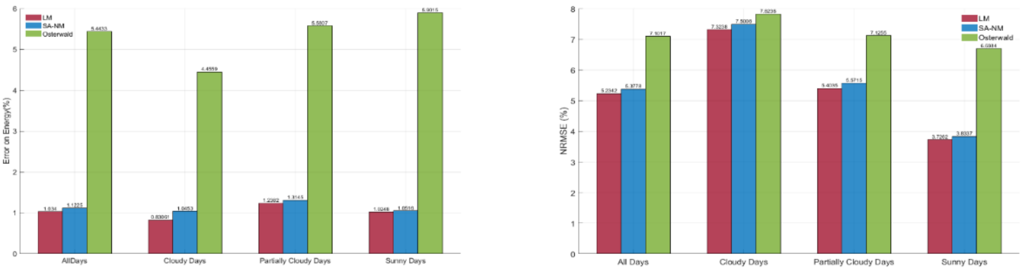

Figure 9-49: Error on estimated energy and NMRSE on maximum power for First Solar module.

Chapter 10

Conclusions

In this study, an innovative technique to efficiently predict the performance of photovoltaic (PV) modules in any weather condition is presented. In particular, this procedure extracts the parameters of an equivalent circuit starting from experimental datasets of current-voltage (I-V) curves of PV generators without mismatch phenomena. The extracted parameters are then used to obtain suitable equations that can predict the behaviour of each parameter with respect to irradiance and temperature. Then, the equations are validated by comparing the predicted PV energy with the measured energy generated during the experimental campaign. This is achieved through the integration over time of the maximum power point.

In this work, two different numerical methods are used for parameters extraction. The first one employs the Levenberg-Marquardt (LM) algorithm, while the second method uses a combination of Simulated-Annealing and Nelder-Mead (SA-NM) algorithms. Moreover, an additional theoretical model has been used to estimate the performance of PV generators in terms of power and energy. This model is the Osterwald model (OM), which is the simplest and most common model known in literature as it provides the maximum power point for whichever value of irradiance and temperature. The three models (LM, SA-NM and OM) have been compared both in terms of estimated maximum power and predicted PV energy in order to assess their accuracy in comparison with the measured values.

In order to estimate the validity of the proposed models, the key aspect of this study was the experimental analysis which was carried out by exploiting long-term experimental campaigns conducted at the University of Jaén (Spain). In particular, this analysis has been performed on three PV modules from different technologies: a high efficiency Heterojunction with Intrinsic Thin layer (HIT) module and two thin films, a Copper Indium Gallium Selenide (GIGS) and a Cadmium Telluride (CdTe) modules. The corresponding experimental campaigns were carried out in 2011 (HIT) and 2012 (CIGS, CdTe).

Regarding the HIT module, results show that both methods (LM and SA-NM) accurately extract the parameters of the single diode model. In fact, the normal root mean square errors (*NRMSEs*) associated with the extraction procedure is always below 1%. In addition, considering the equations obtained for each parameter, the NRMSE are relatively low for all parameters. Moreover, regarding the maximum power point estimation, SA-NM and LM behave similarly and they are more accurate than Osterwald method. In particular, the NRMSE on maximum power is 8.52% for LM and 8.57% for SA-NM, whilst is 10.10% for Osterwald. Regarding the error on predicted PV energy, it is around 6.50% and 6.55% for LM and SA-NM, respectively, and around 8.52% for Osterwald method.

Regarding thin films modules, the final results show that for both modules the two developed models are characterized by greater accuracy compared to the Osterwald method. In particular, considering the CIGS module and focusing on the maximum power point estimation, the NRMSE on maximum power is 4.4% for LM and 4.45% for SA-NM, whilst is 7.1% for Osterwald. Regarding the error on predicted PV energy, LM and SA-NM behaves similarly as they are able to predict with greater accuracy the experimental data compared to the Osterwald method. In fact, the error is around 0.54% for LM and 0.68% for SA-NM, respectively, and around 5.1% for Osterwald. Moving on to the CdTe module, it presents similar results. Regarding the maximum power point estimation, LM and SA-NM are once again characterized by lower errors compared to the Osterwald model. In fact, the NRMSE on maximum power is around 5.23% for LM, 5.38% for SA-NM and 7.9% for Osterwald. Moreover, considering the error on predicted PV energy, it is around 1.03% for LM, 1.12% for SA-NM and 5.44% for Osterwald. Lastly, it can be noted that, for both modules, all three methods work better for sunny days that are characterized by overall clear sky condition.

References

[1] B. Anco S, Photovoltaics for Commercial and Utilities Power Generation, Lilburn (GA,USA): Fairmont Press, Inc., 2012.

[2] F. Spertino, *Lezioni di "Solar Photovoltaic System',* Torino: Politecnico di Torino, 2019/2020.

[3] G. Tiwari and S. Dubey, Fundamental of Photovoltaic Modules and their Applications, New Delhi: RSC Publishing, 2010.

[4] A. Goetzberger and V. Hoffmann, Photovoltaic Solar Energy Generation, Freiburg: Springer, 2005.

[5] [Online]. Available: https://www.mdpi.com/2079-9292/9/2/315/htm.

[6] A. Jain and K. Avinashi , Exact analytical solution of the parameters of real solar cells using Lambert W-function, New Delhi (India): Elsevier, 2003.

[7] M. B. Rhouma, A. Gastli, L. B. Brahim, F. Touati and M. Benammar, "A single method for extracting the parameters of the PV cell single-diode model," *Renwable Energy,* vol. 113, 2017.

[8] F. F. Muhammad, M. Y. Yahya, S. S. Hameed, F. Aziz, K. Sulaiman, M. A. Rasheed and Z. Ahmad, "Employment of single-diode model to elucidate the variations in photovoltaic parameters under different electrical and thermal conditions," *PLoS ONE,* 2017.

[9] [Online]. Available: https://www.alternative-energy-tutorials.com/energy-articles/solar-cell-*i*-*v*-characteristic.html.

[10] D. G. Lorente, S. Pedrazzi, G. Zini, A. D. Rosa and P. Tartarini, "Mismatch losses in PV power plants," *Solar Energy,* vol. 100, pp. 42-49, 2014.

[11] B. Nasreddine, C. S. M. Ait and A. Panajotis, "PV array power output maximization under partial shading using new shifted PV array arrangements," *Applied Energy,* vol. 287, pp. 326-337, 2017.

[12] [Online]. Available: https://incompliancemag.com/article/esd-failure-analysis-of-pv-module-diodes-and-tlp-test-methods/.

[13] [Online]. Available: https://www.cleanenergyreviews.info/blog/solar-panel-components-construction.

[14] U. Gangopadhyay, S. Das and S. Jana, "State of the Art of Photovoltaic Technology," in *International Conference on Solar Energy Photovoltaics*, Bhubaneswar, India, 2013.

[15] [Online]. Available: https://solarmagazine.com/solar-panels/.

[16] [Online]. Available: https://www.solarelectricsupply.com/sanyo-186-watt-solar-panel-hit-186ba19-324.

[17] A. K. Tossa, Y. Soro, Y. Azoumah and D. Yamegueu, "A new approach to estimate the performance and energy productivity of photovoltaic modules in real operating conditions," *Solar Energy,* 2014.

[18] F. Spertino, J.Ahmad, A.Ciocia, P. D. Leo, A. Murtaza and M. Chiaberge, "Capacitor charging method for *I-V* curve tracer and MPPT in photovoltaic system," *Solar Energy,* vol. 119, pp. 461-473, 2015.

[19] S. Gulkowski, J. V. Munoz Diez, J. Aguilera Tejero and G. Nofuentes, "Energy," *Energy,* vol. 172, pp. 380-390, 2019.

[20] JCGM, *Guide to the expression of uncertinty in measurement,* Geneve, Switzerland, 1995.

[21] Slawomir Koziel and Y. Xin-She , Computational Optimization, Methods and Algorithms, vol. Studies in Computational Intelligence, Berlin: Springer-Verlag Berlin Heidelberg, 2011.

[22] S. Gulkowski, J. V. Munoz Diez, J. Aguilera Tejero and G. Nofuentes Garrido, “Computational modeling and experimental analysis of heterojunction with intrinsic thin-layer photovoltaic module under different environmental conditions,” *Energy,* vol. 172, pp. 380-390, 2019.

[23] J. J. More, “Levenberg-Marquardt algorithm: implementation and theory,” in *Conference on numerical analysis,* , Dundee, UK, 1977.

[24] D. Dash, S. Mallik, R. Roshan, S. Mahata, P. Das and S. Mahato, “An empiral approach towards photovoltaic parameter extraction and optimization,” *Solar energy,* vol. 153, 21 June 2017.

[25] Utkarsh Jadli, Padmanabh Thakur and Rishablh Dev Shukla, “A New Parameter Estimation Method of Solar Photovoltaic,” *IEEE Journal,* vol. 8, no. 1, 2018.

[26] D. Delahaye, S. Chaimatanan and M. Mongeau, “Simulated annealing: from basics to applications,” in *Handbook of Metaheuristics*, Springer, 2019.

[27] R. B. Messaoud, “Extraction of uncertain parameters of single-diode model of a photovoltai panel using simulated annealing optimization,” *Energy Reports,* vol. 6, pp. 350-357, 2020.

[28] C. Kelley, Iterative methods for Optimization, Raleigh, North Carolina: SIAM, 1999.

[29] A. Scaiola, *Innovative technique to estimate the performance of photovoltaic generator using the parameters of the single diode model equivalent circuit,* Politecnico di Torino: Tesi di Laurea Magistrale, 2019.

[30] M. A. Magnetti, *Ad hoc tool for massive data analysis of photovoltaic generators: experimental validation and energy assessment of a high efficiency module,* Politecnico di Torino: Tesi di Laurea Magistrale, 2020.

[31] E. Meca, *Data Modeling and Analysis of a Solar Cell. Evaluation of the rise time from the 5-Parameter Model,* 2017.

[32] R. Miceli, A. Orioli and A. d. Gangi, “A procedure to calculate the *I-V* characteristics of thin-gilm photovoltaic modules using an explicit rational form,” *Applied Energy,* vol. 155, pp. 613-628, 2015.

[33] A. Molina-Garcia, M. Bueso, M. Kessler, J. Guerrero-Perez, J. Fuentes and E. Gomez-Lazaro, “CdTe thin-film solar module modeling using a non-linear regression approach,” in *17th Power system computation Conference*, Stockholm (Sweden), 2011.

[34] N. Anani and H. Ibrahim, “Performance Evaluation of Analytical Methods for Parameters Extraction of Photovoltaic Generators,” *Energies,* vol. 13, 2020.

[35] N. Anani and H. Ibrahim, “Adjusting the Single-Diode Model Parameters of a Photovoltaic Module with Irradiance and Temperature,” *Energies,* vol. 13, 2020.